Fall 2016

Research on hybrid manufacturing using industrial robot

Zhiyuan Wang

Department: Mechanical and Aerospace Engineering

RESEARCH ON HYBRID MANUFACTURING USING INDUSTRIAL ROBOT

by

ZHIYUAN WANG

A DISSERTATION

Presented to the Faculty of the Graduate School of the

MISSOURI UNIVERSITY OF SCIENCE AND TECHNOLOGY

In Partial Fulfillment of the Requirements for the Degree

DOCTOR OF PHILOSOPHY

in

MECHANICAL ENGINEERING

2016

Approved

Dr. Frank Liou, Advisor

Dr. Ashok Midha

Dr. Heng Pan

Dr. Lian Duan

Dr. Joseph W Newkirk

PUBLICATION DISSERTATION OPTION

This dissertation consists of the following five articles that have been published or submitted for publication as follows:

Pages 6-65 are intended for submission to Robotics and Computer-Integrated Manufacturing.

Pages 66-96 are intended for submission to International Journal of Robotics and Automation Technology.

Pages 97-113 have been published in International Journal of Computer Applications in Technology.

Pages 114-132 have been published in Precision Engineering.

Pages 133-156 have been published in 3D Printing and Additive Manufacturing.

All of them have been prepared in the format of Missouri S&T specs.

ABSTRACT

The applications of using industrial robots in hybrid manufacturing overcome many restrictions of the conventional manufacturing methods, such as small part building size, long building period, and limited material choices. However, some problems such as the uneven distribution of motion accuracy within robot working volume, the acceleration impact of robot under heavy external loads, few methods and facilities for increasing the efficiency of hybrid manufacturing process are still challenging. This dissertation aims to improve the applications of using industrial robot in hybrid manufacturing by addressing following three categories research issues. The first research issue proposed a novel concept view on robot accuracy and stiffness problem, for making the maximum usage of current manufacturing capability of robot system. Based on analyzing the robot forward/inverse kinematic, the angle error sensitivity of different joint and the stiffness matrix properties of robot, new evaluation formulations are established to help finding the best position and orientation to perform a specific trajectory within the robot's working volume. The second research issue focus on the engineering improvements of robotic hybrid manufacturing. By adopting stereo vision, laser scanning technology and curved surface compensation algorithm, it enhances the automation level and adaptiveness of hybrid manufacturing process. The third research issue extends the robotic hybrid manufacturing process to the broader application area. A mini extruder with a variable pitch and progressive diameter screw is developed for large scale robotic deposition. The proposed robotic deposition system could increase the building efficiency and quality for large-size parts. Moreover, the research results of this dissertation can benefit a wide range of industries, such as automation manufacturing, robot design and 3D printing.

ACKNOWLEDGMENTS

First and foremost, I would like to express my sincere gratitude to my advisor, Dr. Frank Liou, for his encouragement, insightful guidance, and support during my PhD study at Missouri University of Science and Technology. He patiently guided me through every stage of my research while granted me a great deal of independence. His encouragement endowed me with tremendous confidence in exploring unknown scientific territory and challenging myself to be my best. His diligence and rigorous altitude to research and work will have a significant influence on my future life. It has been a privilege and a great honor to have worked with him.

I would also like to extend my appreciation to all my dissertation committee members, Dr. Ashok Midha, Dr. Heng Pan, Dr. Lian Duan and Dr. Joseph W Newkirk. Without their guidance and valuable comments, it is impossible for me to complete my dissertation.

The dissertation was supported by the Laser Aided Manufacturing Processes (LAMP) Laboratory, and the Intelligent System Center of Missouri S&T, which are gratefully acknowledged.

I would like to express my deep thanks to my lab-mates and friends, Mr. Todd Sparks, Ms. Lisa, Mr. Renwei Liu, Mr. Sreekar Karnati, Mr. Yunlu Zhang, Ms. Xueyang Chen, Mr. Zhiqiang Fan, Mr. Max Mulholland, Mr. Jingwei Zhang, Mr. Xinchang Zhang and Mr. Lei Yan for their support during my study in Rolla.

Last but not the least, I wish to extend my special and sincere thanks to my parents and all the family members, for their love and unwavering support.

TABLE OF CONTENTS

Page

LIST OF ILLUSTRATIONS

Page

PAPER III

PAPER IV

PAPER V

LIST OF TABLES

Page

INTRODUCTION

1.1. BACKGROUND

With the development of automation technology, the scope of applications using industrial robots is getting wider and wider. The potential applications of using industrial robots in hybrid manufacturing, which usually involve both robot deposition process and robot machining process, have been gaining worldwide attention from researchers. In the robot hybrid manufacturing process, the industrial robot arm functions as the motion mechanism for the tools of machining or deposition [1], as shown in Figure 1.1.

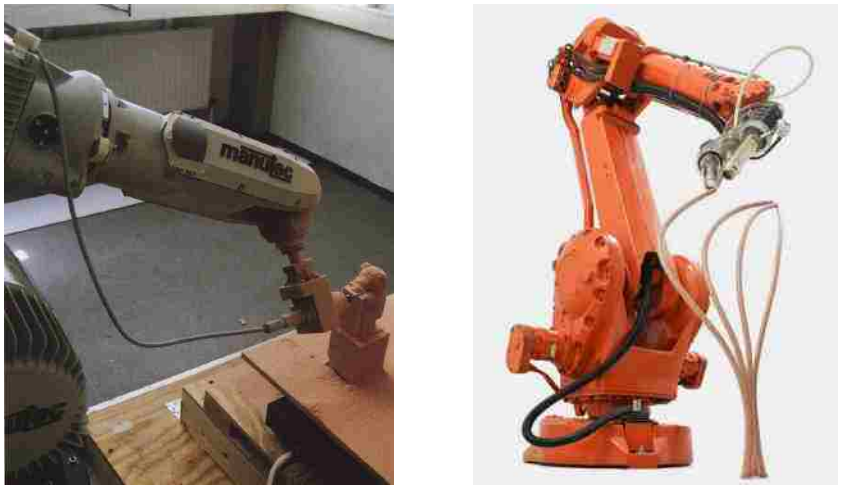

(a) Robot Machining (b) Robot Deposition

Figure 1.1 Robot hybrid manufacturing process

Many restrictions of the conventional manufacturing methods, such as small part building size, long building period, and limited material choices, can be overcame in the hybrid manufacturing process with the using industrial robot. However, some problems still limit its further development, such as the uneven distribution of motion accuracy within robot working volume [2], the acceleration impact of robot under heavy external loads [3], few methods and facilities for increasing the efficiency of hybrid manufacturing

process. In order to solve these problems, this dissertation will investigate the following key research tasks to improve the applications of the industrial robot in hybrid manufacturing process. The outcomes will benefit many areas, such as robotic engineering, additive manufacturing engineering, and high value component repair technology.

1.2. RESEARCH OBJECTIVES

The main objective of this research is to investigate the key technologies for improving the applications of using industrial robot in hybrid manufacturing and expanding it to a wider area. Five research tasks are carefully studied to achieve this overall objective.

Specifically, the research task 1 answers the following question: Where is the best place and orientation to perform a hybrid manufacturing working path within the robot's working envelop. The main challenge for answering this question is how to evaluate the trajectory accuracy at different position and orientation while considering the affection of robot kinematic parameters error. By analyzing the robot forward/inverse kinematic, the angle error sensitivity of different joint in the serial manipulator system will be revealed. The influence of different position and orientation on the movement accuracy of end effector will also be discussed [4-6]. Based on these analysis, a visualized evaluation map can be obtained to describe the accuracy difference of a robotic laser deposition working path at different positions and orientations.

Research task 2 addresses the question of how to improve the operation accuracy when heavy external load applied on robot's end effector. In robotic hybrid manufacturing process, the weight of deposition extruder or the cutting force from machining process, affects the operation accuracy significantly [7-8]. By analyzing the robot kinematic and stiffness matrix properties of robot, a new evaluation formulation will be established for

mapping the trajectory's stiffness within the robot's working volume. The method is important for improving the operation performance of robot system under heavy external laod with its current stiffness capability.

Research Task 3 studies using robot to implement hybrid manufacturing process on a freeform surface. Take the robotic writing task as example, an adaptive compensation algorithm is developed for the robot to deposit ink on a curved surface [9-10]. This method provides more flexibility for using the robot arm to print characters or graph on a curved surface. Meanwhile, the robot system also affords a larger working envelope for ink deposition process. Research Task 4 applies the stereo vision and laser scanning technology into hybrid manufacturing process [11-12]. These methods could realize automatic part alignment and working path generation, and enhance the automation and accuracy of hybrid manufacturing process.

Research Task 5 proposed fused pellets modeling (FPM) system for robotic hybrid manufacturing process. A mini extruder with variable pitch and progressive diameter screw is developed for large scale robotic deposition. In order to get a better control of the extrusion filament shape, some initial studies based on analyzing polymer extrusion theory and non-Newtonian fluid properties will be carried out [13-16]. The robotic FPM system could increase the building efficiency and deposition quality for large-size parts by controlling the filament shape.

The outcomes of above research tasks are expected to advance the knowledge of using robot in hybrid manufacturing process. The technical developments may benefit not only the area of hybrid manufacturing, but also other areas such as robotic engineering, additive manufacturing, and part repair engineering.

1.3. ORGANIZATION OF DISSERTATION

In this dissertation, there are five major developments been presented and been organized in the way as shown in Figure 1.2. Paper I and II focus on theory foundation study for robotic hybrid manufacturing, which highlights the study of movement accuracy and the stiffness property of robot, respectively. Paper III and Paper IV emphasize the engineering improvement of robotic hybrid manufacturing, aims to enhance the automation level and adaptiveness of this process. Paper V develops the fused pellets modeling system for large scale robotic deposition, this study could extend robotic hybrid manufacturing to a wider application area.

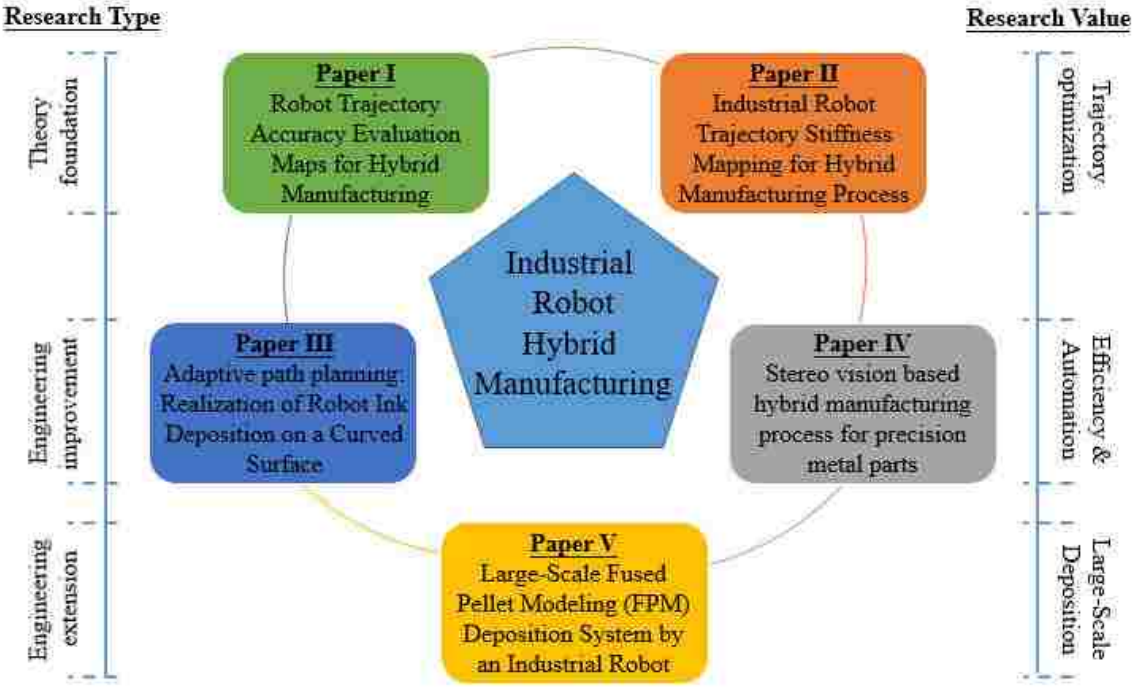

Figure 1.2 Framework of this dissertation

All of the five articles share a same core research topic: hybrid manufacturing using industrial robot, while each of them has a different focus. Paper I presents a new method of finding the best position and orientation to perform a specific hybrid manufacturing working path based on the current accuracy capacity of robot system. This method is

helpful for making the maximum usage of the robot's current accuracy ability rather than blindly pursuit the higher accuracy of robot system. For the situation of heavy external load applied on robot system, a new evaluation formulation is established for mapping the hybrid manufacturing trajectory's stiffness within the robot's working volume in Paper II. One advantage of using robot in hybrid manufacturing is its great flexibility, an adaptive compensation algorithm based on B-spline surface theory is developed for the robot realizing deposit ink on a curved surface in Paper III. In order to improve the efficiency of hybrid manufacturing process, by adopting stereo vision and laser scanning technology, an automatic alignment and path planning method is given in Paper IV. Paper V developed a fused pellets modeling (FPM) system for larger scale robotic deposition, it also studied the methods for optimizing the extrusion process to eliminate the void density during large scale FPM processes.

PAPER

I. INDUSTRIAL ROBOT TRAJECTORY ACCURACY EVALUATION MAPS FOR HYBRID MANUFACTURING PROCESS BASED ON JOINT ANGLE ERROR ANALYSIS

Zhiyuan Wang, Renwei Liu, Todd Sparks, Yunlu Zhang and Frank Liou

Department of Mechanical and Aerospace Engineering

Missouri University of Science and Technology, Rolla, Missouri 65409, U.S.A.

ABSTRACT

Industrial robots have been widely used in various fields. The joint angle error is a main factor that affects the accuracy performance of the robot. It is important to notice that these kinematic parameters error cannot be eliminated from the robot system completely. Even after calibration, these errors still exist and will be fluctuated during the robot system running. This paper proposed a new method of finding the best position and orientation to perform a specific working path based on the current accuracy capacity of robot system. By analyzing the robot forward/inverse kinematic and the angle error sensitivity of different joint in the serial manipulator system, a new evaluation formulation is established for mapping the trajectory accuracy within the robot's working volume. The influence of different position and orientation on the movement accuracy of end effector is discussed. Finally, a visualized evaluation map can be obtained to describe the accuracy difference of a robotic laser deposition working path at different positions and orientations. This method is helpful for making the maximum usage of the robot's current accuracy ability rather than blindly pursuit the higher accuracy of robot system.

Keywords: Industrial Robot, Trajectory Accuracy, Joint Angle Error, Hybrid Manufacturing

1. INTRODUCTION

Usually, the serial robots are mainly used in industry for tasks that require good repeatability [1-2]. In this case, the movement accuracy of a robot is not important, as long as the robot end-effector poses are manually taught, repeatability is all that matters. However, in offline programming tasks, like the robotic hybrid manufacturing process, movement accuracy becomes important, since the working path and positions are defined in a virtual space with respect to an absolute or relative coordinate system.

In order to improve the precision of robot, some studies have focused on the modeling and identification of the geometric parameter errors and have ignored the non-geometric errors [3-4]. These studies assumed that the effect of the non-geometric errors on the robot position errors is small [5-8]. The identified kinematic parameters are inaccurate, because these non-geometric errors still affect the robot accuracy, non-geometric error parameters cannot be ignored.

Other researchers developed the robot kinematic model including geometric and joint compliance errors. Judd and Knasinski [9] examined experimentally many error sources of a physical robot such as geometric errors, gear errors, servo error, structural deformation errors, thermal change errors, gear wear errors and base misalignment. However, these error sources are specific to individual physical robots, so the method is not general. Dulen and Schröer [10] applied the elastic beam theory to investigate the robot link effects as represented by the changes of six differential elements. Hudgens et al. [11] used a method for the identification of general robot compliance characteristics under applied torques and forces. But both studies did not include sufficient non-geometric errors for accurate robot calibration.

Some researchers focused on algorithm study, one of the most be used is the least squares algorithm for parameter identification [12]. There are many other studies using various algorithms for parameter identification such as nonlinear optimization procedure [13-14], iterative linearization, extended Kalman filter. The effectiveness of the identification algorithms was compared in the calibration study for SCARA robot by Omodei et al. [15]. Omodei et al. concluded that EKF is the best among the above algorithms due to the advantages such as fast convergence, reliability and estimation of identification result uncertainty. Park and Kim [16] conclude the same remark that EKF converges faster than Least Squares Estimation. Some algorithms also used for parameter identification for examples maximum likelihood [17], Levenberg–Marquardt [18] although their convergence speeds are fairly slow.

Besides, to increase robot accuracy, its kinematic properties are identified based on robot signature. Stone et al. [19-20] developed an identification method to estimate S model parameters based on joint features such as rotation plane, rotation center and rotation radius. Afterward, D-H parameters can be extracted from the parameters of S model. Abderrahim and Whittaker [21] identify directly D–H parameters by adopting the method of Stone et al. without utilizing the S model. These studies, however, only found out robot geometric parameters. Another calibration method applied genetic programming for calibrating manipulators [22]. The advantage of the method is that it makes a correcting model automatically by genetic programming (or symbolic regression) and therefore avoiding the involvement of human in building robot calibration models. However, this method does not supply knowledge of error sources in robot structure and has slow convergence speed due to the nature of the method.

In addition to the model-based calibration methods mentioned above, alternative approaches such as the so-called model-free calibration have been developed for robot calibration. These approaches are based on an approximation of robot kinematic relationships, such as the relationship between the robot joint readings and its position errors or between the robot positions and its position errors. In order to approximate these relationships, some researchers have used radial basis function networks (RBFN) [23], fuzzy logic algorithms [24], and artificial neural networks (ANN) [25-26]. Some other researchers have utilized polynomials such as Fourier polynomials, ordinary polynomials, and the polynomials of Jacobi, Laguerre and Hermeite, and Bessel. Other works have used Fourier and ordinary polynomials to predict the robot position errors at its configurations or end-effector positions [27-28]. However, these techniques are limited due to their low accuracy and complicated polynomials. Among those approximation techniques, the ANN-based functional approximation is the most effective due to its ability to generalize high adaptation, flexibility, and learning ability. In some studies [29-30], a functional relationship between the robot joint angle and its corresponding joint errors are formulated based on an ANN. However, the ANN training data that are obtained by the robot's nominal inverse kinematics are inaccurate. Generally, the methods of approximation for robot kinematics are limited with regard to understanding the sensitivity of the robot error sources, even the errors that can be modeled or measured easily.

As the above stated studies, most of study in this area are focus on improve the accuracy of robot system, but it is important to notice that these kinematic parameters error cannot be eliminated from the robot system completely. Even after calibration, these errors still exist and will be fluctuated during the robot system running. Thus it is more

meaningful to make the maximum usage of the robot's current accuracy ability rather than blindly pursuit the higher accuracy of robot system. This paper proposed a new method of finding the best position and orientation to perform a specific working path based on the current accuracy capacity of robot system. This paper is composed as following structure: Firstly, the knowledge of rigid body representation and homogeneous transformation matrices is introduced. Then by analyzing the robot forward/inverse kinematic and the angle error sensitivity of different joint in the serial manipulator system, a new evaluation formulation is established for mapping the trajectory accuracy within the robot's working volume. The influence of different position and orientation on the movement accuracy of end effector is discussed. Finally, a visualized evaluation map can be obtained to describe the accuracy difference of a robotic laser deposition working path at different positions and orientations.

2. RIGID BODY REPRESENTATION AND HOMOGENEOUS TRANSFORMATION MATRIX

A point P in space can be represented by its three coordinates relative to Cartesian reference frame:

$$\mathrm{P} = p_x \boldsymbol{\imath} + p_y \boldsymbol{J} + p_z \widehat{\boldsymbol{k}} \tag{1}$$

Where p_x, p_y, and p_z are the three coordinates of the points represented in the reference frame. $\boldsymbol{\imath}$, $\boldsymbol{J}$, and $\widehat{\boldsymbol{k}}$ are the unit vectors along each axis in the reference frame.

A vector can be represented by three coordinates of its tail and of its head. If the vector starts at O_A and ends at the point P (Figure 2.1), then:

$${}^{A}\boldsymbol{p} = p_x \boldsymbol{\imath} + p_y \boldsymbol{J} + p_z \widehat{\boldsymbol{k}} \tag{2}$$

Where p_x, p_y, and p_z are the three components of the vector in the reference frame. In fact, point P is in reality represented by a vector connected to it at point P and expressed by the three components of the vector. The vector can also be written in a matrix form in the reference frame, as shown in Equation (3).

$${}^{A}\boldsymbol{p} = \begin{bmatrix} p_x \\ p_y \\ p_z \end{bmatrix} \tag{3}$$

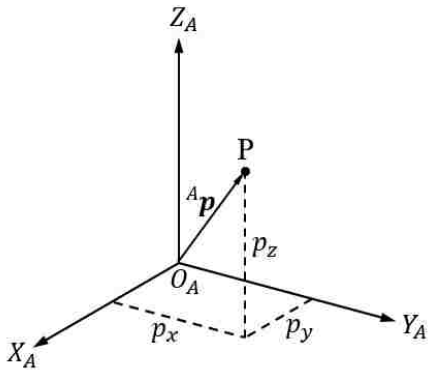

Figure 2.1 Representation of a point and a vector in space

An object can be represented in space by attaching a frame to it and representing the frame in space. Since the object is permanently attached to this frame, its position and orientation relative to this frame is always known. As a result, as long as the frame can be described in space, the object's location and orientation relative to the fixed frame will be known, as shown in Figure 2.2.

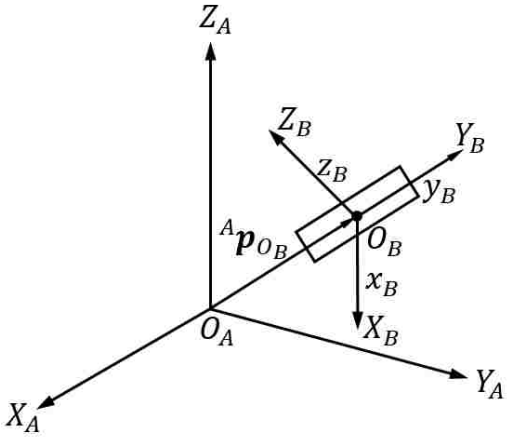

Figure 2.2 Representation of an object in space

Where x_B, y_B, and z_B are the unit vector in the reference frame B, the three unit vectors are mutually perpendicular and their length must be equal to unity. These constraints translate into the following constraint equations:

$$ {}^A x_B \;\; {}^A x_B = {}^A y_B \;\; {}^A y_B = {}^A z_B \;\; {}^A z_B = 1 \tag{4} $$

$$ {}^A x_B \;\; {}^A y_B = {}^A y_B \;\; {}^A z_B = {}^A z_B \;\; {}^A x_B = 0 \tag{5} $$

Create a 3×3 matrix ${}^A_B\boldsymbol{R}$, use the direction cosine value of x_B, y_B, and z_B relative to the unit vector in the reference frame A as the elements.

$$ {}^A_B\boldsymbol{R} = [{}^A x_B \quad {}^A y_B \quad {}^A z_B] = \begin{bmatrix} r_{11} & r_{12} & r_{13} \\ r_{21} & r_{22} & r_{23} \\ r_{31} & r_{32} & r_{33} \end{bmatrix} \tag{6} $$

${}^{A}_{B}\boldsymbol{R}$ represents the rotation of object relative to reference frame A. It is easy to notice that ${}^{A}_{B}\boldsymbol{R}$ is an orthogonal matrix, and satisfying the following equation:

$$ {}^{A}_{B}\boldsymbol{R}^{-1} = {}^{A}_{B}\boldsymbol{R}^{T};\ |{}^{A}_{B}\boldsymbol{R}| = 1 \tag{7} $$

The rotation matrixes about x-axis, y-axis and z-axis are as following:

$$ \boldsymbol{R}(x,\theta) = \begin{bmatrix} 1 & 0 & 0 \\ 0 & c\theta & s\theta \\ 0 & s\theta & c\theta \end{bmatrix} \tag{8} $$

$$ \boldsymbol{R}(y,\theta) = \begin{bmatrix} c\theta & 0 & s\theta \\ 0 & 1 & 0 \\ s\theta & 0 & c\theta \end{bmatrix} \tag{9} $$

$$ \boldsymbol{R}(z,\theta) = \begin{bmatrix} c\theta & s\theta & 0 \\ s\theta & c\theta & 0 \\ 0 & 0 & 1 \end{bmatrix} \tag{10} $$

Therefore, the object's location and orientation relative to the fixed frame can be described by a 4×4 homogeneous matrix:

$$ {}^{A}_{B}T = \begin{bmatrix} {}^{A}_{B}R & {}^{A}\boldsymbol{p}_{O_B} \\ 0 & 1 \end{bmatrix} \tag{11} $$

3. D-H REPRESENTATION OF 6-DOF INDUSTRIAL ROBOT

In 1955, Denavit and Hartenberg published a paper in the ASME Journal of Applied Mechanics that was later used to represent and model robots and to derive their equations of motion. The Denavit – Hartenberg (D-H) model of the representation is a very simple way of modeling robot links and joints that can be used for any robot configuration, regardless of its sequence and complexity.

It has the added benefit that many techniques have been developed for use with its results, such as the calculation of Jacobians, force analysis, etc. This method has become the standard way of representing robots and modeling their motions.

For the 6-DOF industrial robot, a reference frame will be assigned to each joint and define a general procedure to transform form one joint to the next. Combine all the transformations from the base to the first joint, from the first joint to the second joint, etc., until get to the last joint, the robot's total transformation matrix will be obtained.

Figure 3.1 shows two reference frames, each has assigned on a rotate joint. Assign joint number i to the first shown joint, $i + 1$ to the second shown joint.

All joints, without exception, are represented by a z-axis. For the revolute, the z-axis is in the direction of rotation as followed by the right-hand rule for rotations and the rotation value θ about the z-axis will be the joint variable.

As shown in Figure 3.1, in general, the joints may not necessarily be parallel or intersecting. As a result, in general, the z-axes are skew lines.

There is always one line mutually perpendicular to any two skew lines, called the the common normal, which has the shortest distance between the two skew lines. The x-axis of the local reference frame always be assigned in the direction of the common normal.

Thus, if a_i represents the common normal between z_i and z_{i+1}, the direction of x_{i+1} will be along a_i.

In figure 3.1, θ represents a rotation about the z-axis, d represents the distance on z-axis between two successive common normal, a represents the length of each common normal (also called joint offset), and α represents the angle between two successive z-axes (also called joint twist).

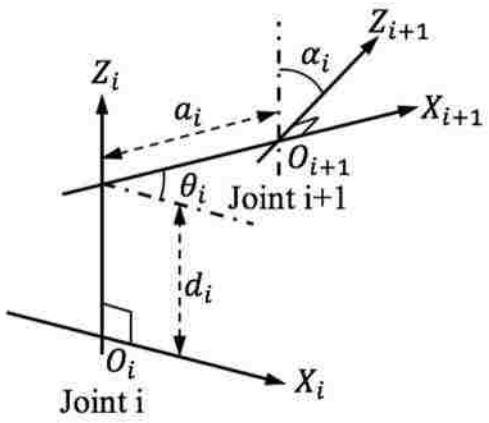

Figure 3.1 A D-H representation of robot joint-link frame combination

The next step is to follow the necessary motions to transform from one reference frame to the next. Assuming that starting from the local reference frame x_i z_i, the next local reference frame x_{i+1} z_{i+1} will be get by following four standard motions:

(I) Rotate about the z_i-axis and angle of θ_i, this will make x_i and x_{i+1} parallel to each other. This is true because a_i and $a_{i+\theta}$ are both perpendicular to z_i and rotating an angle of θ_i will make them parallel (and thus coplanar). (II) Translate along the z_i-axis a distance of d_i to make x_i and x_{i+1} collinear. Since x_i and x_{i+1} were already parallel and normal to z_i, moving along z_i will lay them over each other. (III) Translate along the x_i-axis a distance of a_i to bring the origins of x_i and x_{i+1} together. At this point, the two origins of the two reference frames will be at the same location. (IV) Rotate z_i-axis about

x_{i+1}-axis an angle of α_i to align z_i-axis with z_{i+1}-axis. At this point, frame i and $i+1$ will be exactly the same, and transformed from one frame to the next will be obtained.

Doing the exactly the same sequence of four movements between the $i+1$ and $i+2$ frames will transform one to the next, and by repeating this as necessary, successive frames can be transformed. Starting with the reference frame, firstly transformed to the base of the robot, then to the first joint, second joint…, until the end effector. What is nice is that the foregoing sequence of movements remains the same between any two frames.

Use matrix A representing the four movements is found by post-multiplying these four matrices representing the four movements. Since all transformations are relative to the current frame, all matrices are post-multiplied. The result is as follows:

$$^{i}T_{i+1} = A_i = Rot(z_i, \theta_i) \times Trans(0,0,d_i) \times Trans(a_i,0,0) \times Rot(x_i, \alpha_i)$$

$$= \begin{bmatrix} C\theta_i & S\theta_i & 0 & 0 \\ S\theta_i & C\theta_i & 0 & 0 \\ 0 & 0 & 1 & 0 \\ 0 & 0 & 0 & 1 \end{bmatrix} \times \begin{bmatrix} 1 & 0 & 0 & 0 \\ 0 & 1 & 0 & 0 \\ 0 & 0 & 1 & d_i \\ 0 & 0 & 0 & 1 \end{bmatrix} \times \begin{bmatrix} 1 & 0 & 0 & a_i \\ 0 & 1 & 0 & 0 \\ 0 & 0 & 1 & 0 \\ 0 & 0 & 0 & 1 \end{bmatrix} \times \begin{bmatrix} 1 & 0 & 0 & 0 \\ 0 & C\alpha_i & S\alpha_i & 0 \\ 0 & S\alpha_i & C\alpha_i & 0 \\ 0 & 0 & 0 & 1 \end{bmatrix} \quad (12)$$

$$A_i = \begin{bmatrix} C\theta_i & S\theta_i C\alpha_i & S\theta_i S\alpha_i & a_i C\theta_i \\ S\theta_i & C\theta_i C\alpha_i & C\theta_i S\alpha_i & a_i S\theta_i \\ 0 & S\alpha_i & C\alpha_i & d_i \\ 0 & 0 & 0 & 1 \end{bmatrix} \quad (13)$$

In the equations, $S\theta_i$ represents $sin(\theta_i)$, $C\theta_i$ represents $cos(\theta_i)$.

Use $\boldsymbol{A}_1$ represents the location and orientation of the first joint relative to the base frame of the robot, $\boldsymbol{A}_2$ represents the location and orientation of the second joint relative to the first joint frame.

Thus the location and orientation of the second joint relative to the base frame can be represented by the post-multiplying previous two matrices:

$$T_2 = A_1 A_2 \quad (14)$$

Calling the result of post-multiplying $\boldsymbol{A}_i$ matrices as $\boldsymbol{T}$, if the pre-superscript is 0, it can be omitted to write.

At the base of the robot, start with the first joint and transform to the second joint, then to the third…, to the hand of the robot, and eventually to the end effector. For a n degree of freedom series robot, there will be number n of $\boldsymbol{A}$ matrices, the total transformation between the base of the robot and the end effector is:

$$T_n = A_1 A_2 A_3 \quad A_n \tag{15}$$

To facilitate the calculation of the $\boldsymbol{A}$ matrices, a table of joint and link parameters will be formed, whereby the values representing each link and joint are determined from the schematic drawing of the robot, and are substituted into each $\boldsymbol{A}$ matrix.

The Nachi Robot (SC300F-02) is used as an illustrate example throughout this paper. It has a 4.1 m^2 (cross-section area) operating area and a 300° rotation range for the base motor (Figure 3.2), which could provide a much bigger working envelope than any current hybrid manufacturing system. The 6-axis movement mechanism makes the deposition/machining process more flexible in building a model with complex features.

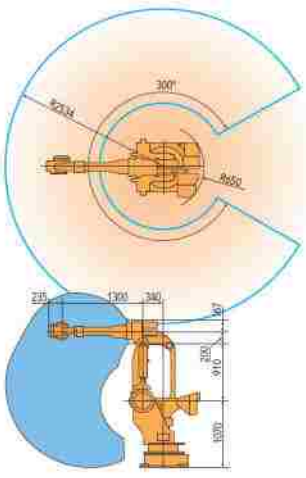

Figure 3.2 Working envelop and links schematic of Nachi Robot (SC300F-02)

Based on the previous of knowledge of how to set the reference frame axis on each joint, and figuring out the positive rotation direction of each joint by operating the robot manually, the kinematic chain of Nachi Robot (SC300F-02) is shown in Figure 3.3.

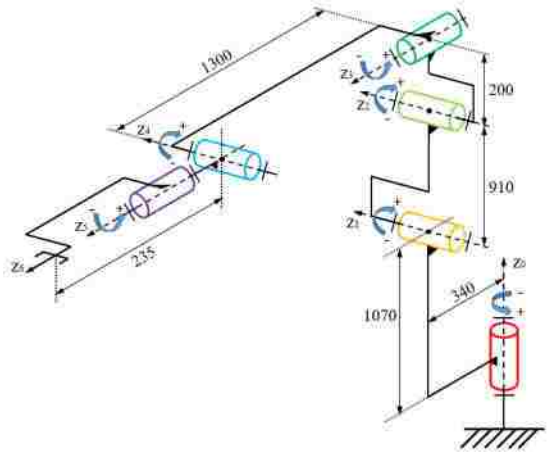

Figure 3.3 Kinematic chain schematic of Nachi Robot (SC300F-02)

But one thing needs to be noticed is that at current posture, the joints value displayed on the robot's touchpad is $[0^\circ \quad 90^\circ \quad 0^\circ \quad 0^\circ \quad 0^\circ \quad 0^\circ]$. In order to build a D-H model could represent the real robot perfectly, all of the joint value should be set to 0°, thus the robot's posture will be look like as the Figure 3.4:

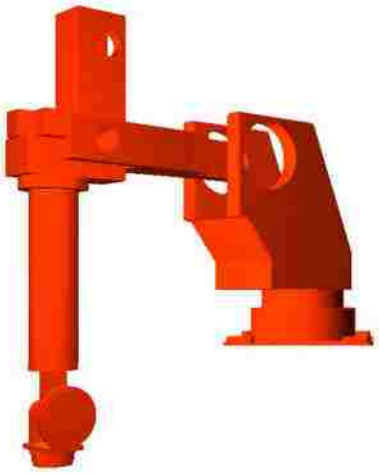

Figure 3.4 Robot's posture when joints value as $[0^\circ \quad 0^\circ \quad 0^\circ \quad 0^\circ \quad 0^\circ \quad 0^\circ]$

Start at joint 1, z_0 represents the first joint, which is the base revolute joint, x_0 is chosen to be the same direction as the reference frame x-axis of the robot controller, this is done for convenience to verify the correctness of the D-H model. x_0 is a fixed field axis, it represents the base of the robot. Next, z_1 is assigned at joint 2. x_1 will be normal to z_0 and z_1, because these two axes are intersecting. x_2 will be in the direction of the common normal between z_1 and z_2. x_3 is in the direction of the common normal between z_2 and z_3. In order to ensure the solvability of the invers kinematic of robot, z_4, z_5 and z_6 are assigned at the same origin point. Thus, the reference frames representation of Nachi robot as shown in Figure 3.5. Normally, the end effector is not included in the equations of motions, but it can be represented by an additional line in the D-H parameters table. In the case, the tip point of end effector physically represents the center point of the fixing plate of the joint 6, it is also as the same as the coordinate value that indicated on the robot's touch pad.

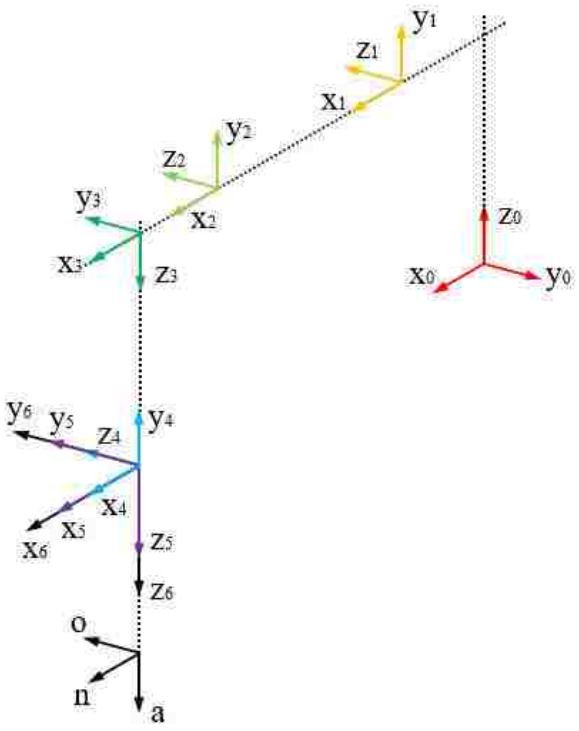

Figure 3.5 Reference frames representation of Nachi robot

According to these assigned coordinate frames, the parameters of D-H model can be filled out in Table 3.1. Notice that the rotations are measured with the right-hand rule. The curled fingers of your right hand, rotating in the direction of rotation, determine the direction of the axis of rotation along the thumb.

Table 3.1 D-H model parameters of Nachi Robot (SC300F-02)

i	θ_i	d_i	a_i	α_i
1	θ_1	1070	340	90
2	θ_2	0	910	0
3	θ_3	0	200	90
4	θ_4	1300	0	-90
5	θ_5	0	0	90
6	θ_6	0	0	0
tool	0	235	0	0

4. ROBOT KINEMATIC

Robot kinematic equations can establish the mapping of parameters between joints angle domain and coordinate domain of the end effector (Figure 4.1). The forward kinematic problem is concerned how to calculate the position and orientation of the end effector from a group of known joints value. On the contrary, the inverse kinematic problem is to determine the value of each joint in order to place the arm at a desired position and orientation.

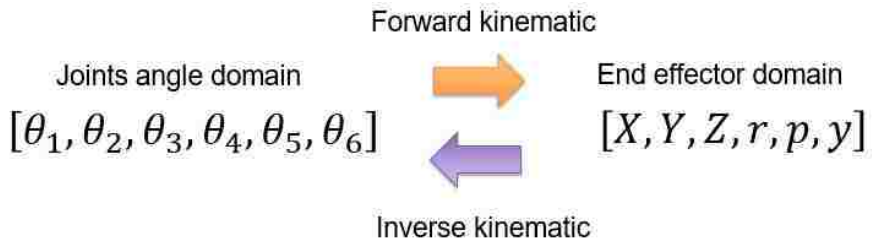

Figure 4.1 Mapping relationship between joints angle domain and end effector domain

4.1. FORWARD KINEMATIC OF ROBOT

According to Equation 14, T_n represents the transformation matrix of end effector frame relative to the base frame of a n degree of freedom series robot. The position and orientation of an arbitrary point ${}^{n}p = [p_x \quad p_y \quad p_z]$ on the end effector can be described in the robot base coordinate frame as following:

$$ {}^{0}p = T_n {}^{n}p = A_1 A_2 A_3 \quad A_n {}^{n}p \tag{16} $$

For a robot which structure has been determined, according to D-H model table, link length a_i, link offset d_i, and link rotation angle α_i are all known parameters, θ_i are the variables changing with the movement of the robot. Thus, the equations of forward kinematic can be written as:

$$ T_n = A_1(\theta_1) A_2(\theta_2) A_3(\theta_3) \quad A_n(\theta_n) \tag{17} $$

For the Nachi robot, there are 6 joints, the transformation between each two successive joints can be written by simply substituting the parameters from the Table 1:

$$A_1 = \begin{bmatrix} C_1 & 0 & S_1 & a_1C_1 \\ S_1 & 0 & C_1 & a_1S_1 \\ 0 & 1 & 0 & d_1 \\ 0 & 0 & 0 & 1 \end{bmatrix} \tag{18}$$

$$A_2 = \begin{bmatrix} C_2 & S_2 & 0 & a_2C_2 \\ S_2 & C_2 & 0 & a_2S_2 \\ 0 & 0 & 1 & 0 \\ 0 & 0 & 0 & 1 \end{bmatrix} \tag{19}$$

$$A_3 = \begin{bmatrix} C_3 & 0 & S_3 & a_3C_3 \\ S_3 & 0 & C_3 & a_3S_3 \\ 0 & 1 & 0 & 0 \\ 0 & 0 & 0 & 1 \end{bmatrix} \tag{20}$$

$$A_4 = \begin{bmatrix} C_4 & 0 & S_4 & 0 \\ S_4 & 0 & C_4 & 0 \\ 0 & 1 & 0 & d_4 \\ 0 & 0 & 0 & 1 \end{bmatrix} \tag{21}$$

$$A_5 = \begin{bmatrix} C_5 & 0 & S_5 & 0 \\ S_5 & 0 & C_5 & 0 \\ 0 & 1 & 0 & 0 \\ 0 & 0 & 0 & 1 \end{bmatrix} \tag{22}$$

$$A_6 = \begin{bmatrix} C_6 & S_6 & 0 & 0 \\ S_6 & C_6 & 0 & 0 \\ 0 & 0 & 1 & 0 \\ 0 & 0 & 0 & 1 \end{bmatrix} \tag{23}$$

In the equations, S_i represents $sin(\theta_i)$, C_i represents $cos(\theta_i)$.

According to equation 11, the $\boldsymbol{T}_6$ is a 4×4 homogeneous matrix, the forward kinematic solution of Nachi Robot it can be written as following:

$$T_6 = \begin{bmatrix} n_x & o_x & a_x & p_x \\ n_y & o_y & a_y & p_y \\ n_z & o_z & a_z & p_z \\ 0 & 0 & 0 & 1 \end{bmatrix} = A_1A_2A_3A_4A_5A_6 \quad (24)$$

The elements in the matrix are as following:

$n_x = C_1(C_2(C_3(C_4C_5C_6 \quad S_4S_6) \quad C_6S_3S_5) \quad S_2(S_3(C_4C_5C_6 \quad S_4S_6) + C_3C_6S_5)) +$

$S_1(C_4S_6 + C_5C_6S_4)$

$n_y = S_1(C_2(C_3(C_4C_5C_6 \quad S_4S_6) \quad C_6S_3S_5) \quad S_2(S_3(C_4C_5C_6 \quad S_4S_6) + C_3C_6S_5))$

$C_1(C_4S_6 + C_5C_6S_4)$

$n_z = C_2(S_3(C_4C_5C_6 \quad S_4S_6) + C_3C_6S_5) + S_2(C_3(C_4C_5C_6 \quad S_4S_6) \quad C_6S_3S_5)$

$o_x = C_1(C_2(C_3(\quad C_4C_5S_6 \quad C_6S_4) + S_3S_5S_6) \quad S_2(S_3(\quad C_4C_5S_6 \quad C_6S_4) \quad C_3S_5S_6)) +$

$S_1(C_4C_6 \quad C_5S_4S_6)$

$o_y = S_1\big(C_2(C_3(\quad C_4C_5S_6 \quad C_6S_4) + S_3S_5S_6) \quad S_2(S_3(\quad C_4C_5S_6 \quad C_6S_4) \quad C_3S_5S_6)\big)$

$C_1(C_4C_6 \quad C_5S_4S_6)$

$o_z = C_2(S_3(\quad C_4C_5S_6 \quad C_6S_4) \quad C_3S_5S_6) + S_2(C_3(\quad C_4C_5S_6 \quad C_6S_4) + S_3S_5S_6)$

$a_x = C_1(C_2(C_3C_4C_5 + C_5S_3) \quad S_2(C_4S_3S_5 \quad C_3C_5)) + S_1S_4S_5$

$a_y = S_1\big(C_2(C_3C_4S_5 + C_5S_3) \quad S_2(C_4S_3S_5 \quad C_3C_5)\big) \quad C_1S_4S_5$

$a_z = C_2(C_4S_3S_5 \quad C_3C_5) + S_2(C_3C_4S_5 + C_5S_3)$

$p_x = C_1(C_2(d_4S_3 + a_3C_3) \quad S_2(a_3S_3 \quad d_4C_3) + a_2C_2) + a_1C_1$

$p_y = S_1(C_2(d_4S_3 + a_3C_3) \quad S_2(a_3S_3 \quad d_4C_3) + a_2C_2) + a_1C_1$

$p_z = S_2(d_4S_3 + a_3C_3) + C_2(a_3S_3 \quad d_4C_3) + a_2S_2 + d_1$

4.2. INVERSE KINEMATIC OF ROBOT

The previous section showed how to determine the end-effector position and orientation in terms of the joint variables. This section is concerned with the inverse problem of finding the joint variables in terms of the end-effector position and orientation.

This is the problem of inverse kinematics, and it is, in general, more difficult than the forward kinematics problem. The following derivation steps will show how to obtain the solution of inverse kinematics of robot:

Step 1: solve θ_1

$\because\ T_6 = A_1A_2A_3A_4A_5A_6$

$\therefore A_1^{-1}T_6 = A_2A_3A_4A_5A_6$

Make $\boldsymbol{L} = A_1^{-1}T_6$, $\boldsymbol{R} = A_2A_3A_4A_5A_6$

$\because$ For the two equal matrixes, the corresponding elements in matrix are equal as well.

$\therefore \boldsymbol{L}(3,4) = \boldsymbol{R}(3,4)$

$\because \begin{cases} \boldsymbol{L}(3,4) = p_x \sin(\theta_1) \quad p_y \cos(\theta_1) \\ \boldsymbol{R}(3,4) = 0 \end{cases}$

$\therefore p_x \sin(\theta_1) \quad p_y \cos(\theta_1) = 0$

$\Rightarrow \dfrac{\sin(\theta_1)}{\cos(\theta_1)} = \dfrac{p_y}{p_x} = \tan(\theta_1)$

Therefore, the solution of θ_1 is:

$$\theta_1 = atan2(p_y, p_x) \tag{25}$$

Step 2: solve $\boldsymbol{\theta_3}$

$\because\ T_6 = A_1A_2A_3A_4A_5A_6$

$\therefore A_1^{-1}T_6 = A_2A_3A_4A_5A_6$

Make $\boldsymbol{L} = A_1^{-1}T_6$, $\boldsymbol{R} = A_2A_3A_4A_5A_6$

$\because$ For the two equal matrixes, the corresponding elements in each matrix are equal as well.

$$\therefore \begin{cases} \boldsymbol{L}(1,4) = \boldsymbol{R}(1,4) \\ \boldsymbol{L}(2,4) = \boldsymbol{R}(2,4) \end{cases}$$

$$\because \begin{array}{c} \boldsymbol{L}(1,4) = p_y \sin(\theta_1) + p_x \cos(\theta_1) \quad a_1 \\ \boldsymbol{R}(1,4) = d_4 \sin(\theta_2 + \theta_3) + a_3 \cos(\theta_2 + \theta_3) + a_2 \cos(\theta_2) \\ \boldsymbol{L}(2,4) = p_z \quad d_1 \\ \boldsymbol{R}(2,4) = a_3 \sin(\theta_2 + \theta_3) \quad d_4 \cos(\theta_2 + \theta_3) + a_2 \sin(\theta_2) \end{array}$$

Notice that all variables in $\boldsymbol{L}(1,4)$ and $\boldsymbol{L}(2,4)$ are known, make $k_1 = \boldsymbol{L}(1,4)$ and $k_2 = \boldsymbol{L}(2,4)$

$$\Rightarrow \begin{cases} k_1 = d_4 \sin(\theta_2 + \theta_3) + a_3 \cos(\theta_2 + \theta_3) + a_2 \cos(\theta_2) \\ k_1 = a_3 \sin(\theta_2 + \theta_3) \quad d_4 \cos(\theta_2 + \theta_3) + a_2 \sin(\theta_2) \end{cases}$$

$$\Rightarrow \begin{cases} k_1^2 = (d_4 \sin(\theta_2 + \theta_3) + a_3 \cos(\theta_2 + \theta_3) + a_2 \cos(\theta_2))^2 \\ k_2^2 = (a_3 \sin(\theta_2 + \theta_3) \quad d_4 \cos(\theta_2 + \theta_3) + a_2 \sin(\theta_2))^2 \end{cases}$$

$$\Rightarrow k_1^2 + k_2^2 = 2a_2 d_4 \sin(\theta_3) + 2a_2 a_3 \cos(\theta_3) + d_4^2 + a_3^2 + a_2^2$$

$$\Rightarrow d_4 \sin(\theta_3) + a_3 \cos(\theta_3) = \frac{(k_1^2 + k_2^2) \quad (d_4^2 + a_3^2 + a_2^2)}{2a_2}$$

Make $k = \frac{(k_1^2 + k_2^2) - (d_4^2 + a_3^2 + a_2^2)}{2a_2}$, and based on the knowledge of trigonometric functions, the equation $sin^2(x) + cos^2(x) = 1$ is always true.

$$\Rightarrow \begin{cases} d_4 \sin(\theta_3) + a_3 \cos(\theta_3) = k \\ sin^2(\theta_3) + cos^2(\theta_3) = 1 \end{cases}$$

These are binary quadratic equations, in which $\sin(\theta_3)$ and $\cos(\theta_3)$ are regarded as the unknown variables. Solve these equations, the two sets of solution are as following:

Solution 1 of θ_3:

$$\left[\sin(\theta_{3-1}) = \frac{a_3\sqrt{k^2 + d_4^2 + a_3^2} \quad d_4 k}{d_4^2 + a_3^2}, \quad \cos(\theta_{3-1}) = \frac{d_4\sqrt{k^2 + d_4^2 + a_3^2} + a_3 k}{d_4^2 + a_3^2}\right]$$

$$\Rightarrow \tan(\theta_{3-1}) = \frac{a_3\sqrt{k^2 + d_4^2 + a_3^2} + d_4 k}{d_4\sqrt{k^2 + d_4^2 + a_3^2} + a_3 k}$$

$$\Rightarrow \tan(\theta_{3-1}) = \frac{(\ \ a_3\sqrt{\ k^2 + d_4^2 + a_3^2} + d_4 k)(\frac{1}{d_4\sqrt{\ k^2 + d_4^2 + a_3^2}})}{(d_4\sqrt{\ k^2 + d_4^2 + a_3^2} + a_3 k)(\frac{1}{d_4\sqrt{\ k^2 + d_4^2 + a_3^2}})}$$

$$\Rightarrow \tan(\theta_{3-1}) = \frac{\left(\frac{a_3}{d_4}\right) + (\frac{k}{\sqrt{\ k^2 + d_4^2 + a_3^2}})}{1 \quad \left(\frac{a_3}{d_4}\right)(\frac{k}{\sqrt{\ k^2 + d_4^2 + a_3^2}})}$$

Based on the knowledge of trigonometric functions, there is:

$$\tan(\alpha + \beta) = \frac{\tan(\alpha) + \tan(\beta)}{1 \quad \tan(\alpha)\tan(\beta)}$$

Make $\alpha = atan2(\ \ a_3, d_4),\ \beta = atan2(k, \sqrt{\ k^2 + d_4^2 + a_3^2})$

$$\Rightarrow \tan(\alpha + \beta) = \frac{\tan(atan2(\ \ a_3, d_4)) + \tan(atan2(k, \sqrt{\ k^2 + d_4^2 + a_3^2}))}{1 \quad \tan(atan2(\ \ a_3, d_4))\tan(atan2(k, \sqrt{\ k^2 + d_4^2 + a_3^2}))}$$

$$= \tan(\theta_{3-1})$$

$$\Rightarrow \theta_{3-1} = \alpha + \beta = atan2(\ \ a_3, d_4) + \ atan2(k, \sqrt{\ k^2 + d_4^2 + a_3^2})$$

Solution 2 of θ_3:

$$\left[\sin(\theta_{3-2}) = \frac{a_3\sqrt{\ k^2 + d_4^2 + a_3^2} + d_4 k}{d_4^2 + a_3^2},\quad \cos(\theta_{3-2}) = \quad \frac{d_4\sqrt{\ k^2 + d_4^2 + a_3^2} \quad a_3 k}{d_4^2 + a_3^2}\right]$$

$$\Rightarrow \tan(\theta_{3-2}) = \frac{a_3\sqrt{\ k^2 + d_4^2 + a_3^2} + d_4 k}{d_4\sqrt{\ k^2 + d_4^2 + a_3^2} + a_3 k}$$

$$\Rightarrow \tan(\theta_{3-2}) = \frac{(a_3\sqrt{\ k^2 + d_4^2 + a_3^2} + d_4 k)(\ \ \frac{1}{d_4\sqrt{\ k^2 + d_4^2 + a_3^2}})}{(\ \ d_4\sqrt{\ k^2 + d_4^2 + a_3^2} + a_3 k)(\ \ \frac{1}{d_4\sqrt{\ k^2 + d_4^2 + a_3^2}})}$$

$$\Rightarrow \tan(\theta_{3-2}) = \frac{\left(\frac{a_3}{d_4}\right) + \left(\frac{k}{\sqrt{k^2 + d_4^2 + a_3^2}}\right)}{1 \quad \left(\frac{a_3}{d_4}\right)\left(\frac{k}{\sqrt{k^2 + d_4^2 + a_3^2}}\right)}$$

Based on the knowledge of trigonometric functions, there is:

$$\tan(\alpha + \beta) = \frac{\tan(\alpha) + \tan(\beta)}{1 \quad \tan(\alpha)\tan(\beta)}$$

Make $\alpha = atan2(\ \ a_3, d_4),\ \beta = atan2(k,\ \ \sqrt{\ k^2 + d_4^2 + a_3^2})$

$$\Rightarrow \tan(\alpha + \beta) = \frac{\tan(atan2(\ \ a_3, d_4)) + \tan(atan2(k,\ \ \sqrt{\ k^2 + d_4^2 + a_3^2}))}{1 \quad \tan(atan2(\ \ a_3, d_4))\tan(atan2(k,\ \ \sqrt{\ k^2 + d_4^2 + a_3^2}))}$$

$$= \tan(\theta_{3-2})$$

$$\Rightarrow \theta_{3-2} = \alpha + \beta = atan2(\ \ a_3, d_4) + \ atan2(k,\ \ \sqrt{\ k^2 + d_4^2 + a_3^2})$$

Therefore, take two results together, the solution of θ_3 is:

$$\theta_3 = atan2(\ \ a_3, d_4) + \ atan2\left(k, \pm\sqrt{\ k^2 + d_4^2 + a_3^2}\right) \tag{26}$$

When $(\ \ k^2 + d_4^2 + a_3^2) \geq 0$

Step 3: solve θ_2

$\because\ T_6 = A_1A_2A_3A_4A_5A_6$

$\therefore\ (A_1A_2A_3)^{-1}T_6 = A_4A_5A_6$

Make $\boldsymbol{L} = (A_1A_2A_3)^{-1}T_6$, $\boldsymbol{R} = A_4A_5A_6$

$\because$ For the two equal matrixes, the corresponding elements in each matrix are equal as well.

$$\therefore \begin{cases} \boldsymbol{L}(1,4) = \boldsymbol{R}(1,4) \\ \boldsymbol{L}(3,4) = \boldsymbol{R}(3,4) \end{cases}$$

$$\because \begin{matrix} \boldsymbol{L}(1,4) = \sin(\theta_2+\theta_3)\,(p_z \quad d_1) + \cos(\theta_2+\theta_3)\,(p_y\sin(\theta_1) + p_x\cos(\theta_1) \quad a_1) \quad \cos(\theta_3)\,a_2 \quad a_3 \\ \boldsymbol{R}(1,4) = 0 \\ \boldsymbol{L}(3,4) = \sin(\theta_2+\theta_3)\,(p_y\sin(\theta_1) + p_x\cos(\theta_1) \quad a_1) + \cos(\theta_2+\theta_3)\,(d_1 \quad p_z) \quad \sin(\theta_3)\,a_2 \\ \boldsymbol{R}(3,4) = d_4 \end{matrix}$$

$$\Rightarrow \begin{matrix} \sin(\theta_2+\theta_3) = \dfrac{(p_y\sin(\theta_1) + p_x\cos(\theta_1) \quad a_1 + p_z \quad d_1)a_2\cos(\theta_3) + (p_y\sin(\theta_1) + p_x\cos(\theta_1) \quad a_1)d_4 + (p_z \quad d_1)a_3}{(p_y\sin(\theta_1) + p_x\cos(\theta_1) \quad a_1)^2 + (d_1 \quad p_z)^2} \\ \cos(\theta_2+\theta_3) = \dfrac{(p_y\sin(\theta_1) + p_x\cos(\theta_1) \quad a_1 + d_1 \quad p_z)a_2\cos(\theta_3) + (p_y\sin(\theta_1) + p_x\cos(\theta_1) \quad a_1)a_3 + (d_1 \quad p_z)d_4}{(p_y\sin(\theta_1) + p_x\cos(\theta_1) \quad a_1)^2 + (d_1 \quad p_z)^2} \end{matrix}$$

Notice that all the variables in equation (xx) are known, thus make:

$$k_1 = \frac{(p_y\sin(\theta_1) + p_x\cos(\theta_1) \quad a_1 + p_z \quad d_1)a_2\cos(\theta_3) + (p_y\sin(\theta_1) + p_x\cos(\theta_1) \quad a_1)d_4 + (p_z \quad d_1)a_3}{(p_y\sin(\theta_1) + p_x\cos(\theta_1) \quad a_1)^2 + (d_1 \quad p_z)^2}$$

$$k_2 = \frac{(p_y\sin(\theta_1) + p_x\cos(\theta_1) \quad a_1 + d_1 \quad p_z)a_2\cos(\theta_3) + (p_y\sin(\theta_1) + p_x\cos(\theta_1) \quad a_1)a_3 + (d_1 \quad p_z)d_4}{(p_y\sin(\theta_1) + p_x\cos(\theta_1) \quad a_1)^2 + (d_1 \quad p_z)^2}$$

$$\Rightarrow \begin{cases} \sin(\theta_2+\theta_3) = k_1 \\ \cos(\theta_2+\theta_3) = k_2 \end{cases}$$

$$\Rightarrow \frac{\sin(\theta_2+\theta_3)}{\cos(\theta_2+\theta_3)} = \frac{k_1}{k_2} = \tan(\theta_2+\theta_3)$$

Therefore, the solution of θ_2 is:

$$\theta_2 = atan2(k_1, k_2) \quad \theta_3 \tag{27}$$

Step 4: solve θ_4

$\because\ T_6 = A_1A_2A_3A_4A_5A_6$

$\therefore\ (A_1A_2A_3)^{-1}T_6 = A_4A_5A_6$

Make $\boldsymbol{L} = (A_1A_2A_3)^{-1}T_6$, $\boldsymbol{R} = A_4A_5A_6$

$\because$ For the two equal matrixes, the corresponding elements in each matrix are equal as well.

$$\therefore \begin{cases} \boldsymbol{L}(1,3) = \boldsymbol{R}(1,3) \\ \boldsymbol{L}(2,3) = \boldsymbol{R}(2,3) \end{cases}$$

$$\because \begin{matrix} \boldsymbol{L}(1,3) = a_z\sin(\theta_2+\theta_3) + a_y\sin(\theta_1)\cos(\theta_2+\theta_3) + a_x\cos(\theta_1)\cos(\theta_2+\theta_3) \\ \boldsymbol{R}(1,3) = \cos(\theta_4)\sin(\theta_5) \\ \boldsymbol{L}(2,3) = a_x\sin(\theta_1) \quad a_y\cos(\theta_1) \\ \boldsymbol{R}(2,3) = \sin(\theta_4)\sin(\theta_5) \end{matrix}$$

Notice that all variables in $\boldsymbol{L}(1,3)$ and $\boldsymbol{L}(2,3)$ are known, make $k_1 = \boldsymbol{L}(2,3)$ and $k_2 = \boldsymbol{L}(1,3)$

$$\Rightarrow \begin{cases} k_1 = a_x \sin(\theta_1) \quad a_y \cos(\theta_1) \\ k_2 = a_z \sin(\theta_2 + \theta_3) + a_y \sin(\theta_1)\cos(\theta_2 + \theta_3) + a_x \cos(\theta_1)\cos(\theta_2 + \theta_3) \end{cases}$$

$$\Rightarrow \begin{cases} k_1 = \sin(\theta_4)\sin(\theta_5) \\ k_2 = \cos(\theta_4)\sin(\theta_5) \end{cases}$$

When $\sin(\theta_5) \neq 0$

$$\Rightarrow \frac{\sin(\theta_4)}{\cos(\theta_4)} = \frac{k_1}{k_2} = \tan(\theta_4)$$

Therefore, the solution of θ_4 is:

$$\theta_4 = atan2(k_1, k_2) \tag{28}$$

Step 5: solve θ_5

$\because\ T_6 = A_1A_2A_3A_4A_5A_6$

$\therefore\ (A_1A_2A_3A_4)^{-1}T_6 = A_5A_6$

Make $\boldsymbol{L} = (A_1A_2A_3A_4)^{-1}T_6$, $\boldsymbol{R} = A_5A_6$

$\because$ For the two equal matrixes, the corresponding elements in each matrix are equal as well.

$$\therefore \begin{cases} \boldsymbol{L}(1,3) = \boldsymbol{R}(1,3) \\ \boldsymbol{L}(2,3) = \boldsymbol{R}(2,3) \end{cases}$$

$\boldsymbol{R}(1,3) = \sin(\theta_5)$

$\boldsymbol{R}(2,3) = \quad \cos(\theta_5)$

$\boldsymbol{L}(1,3) = (a_x \sin(\theta_1) \quad a_y \cos(\theta_1))\sin(\theta_4) + (((\quad a_y \sin(\theta_1)$

$a_x \cos(\theta_1))\sin(\theta_4) + a_z \cos(\theta_2))\sin(\theta_3) + (a_z \cos(\theta_2) + (a_y \sin(\theta_1) +$

$a_x \cos(\theta_1))\cos(\theta_2))\cos(\theta_3))\cos(\theta_4)$

$$\boldsymbol{L}(2,3) = ((\ \ a_y \sin(\theta_1)\ \ \ a_x \cos(\theta_1)) \cos(\theta_2)\ \ \ a_z \sin(\theta_2))\ \ \sin(\theta_3) +$$

$$((\ \ a_y \sin(\theta_1)\ \ \ a_x \cos(\theta_1)) \sin(\theta_2) + a_z \cos(\theta_2)) \cos(\theta_3)$$

Notice that all variables in $\boldsymbol{L}(1,3)$ and $\boldsymbol{L}(2,3)$ are known, make $k_1 = \boldsymbol{L}(1,3)$ and $k_2 = \boldsymbol{L}(2,3)$

$$\Rightarrow \begin{cases} k_1 = \sin(\theta_5) \\ k_2 = \ \ \cos(\theta_5) \end{cases}$$

$$\Rightarrow \frac{\sin(\theta_5)}{\cos(\theta_5)} = \frac{k_1}{k_2} = \tan(\theta_5)$$

Therefore, the solution of θ_5 is:

$$\theta_5 = atan2(k_1,\ \ k_2) \tag{29}$$

Step 6: solve θ_6

$\because\ T_6 = A_1 A_2 A_3 A_4 A_5 A_6$

$\therefore\ (A_1 A_2 A_3 A_4 A_5)^{-1} T_6 = A_6$

Make $\boldsymbol{L} = (A_1 A_2 A_3 A_4 A_5)^{-1} T_6$, $\boldsymbol{R} = A_6$

$\because$ For the two equal matrixes, the corresponding elements in each matrix are equal as well.

$$\therefore \begin{cases} \boldsymbol{L}(1,2) = \boldsymbol{R}(1,2) \\ \boldsymbol{L}(2,2) = \boldsymbol{R}(2,2) \end{cases}$$

$$\boldsymbol{L}(1,2) = (((\ \ o_y \sin(\theta_1)\ \ \ o_x \cos(\theta_1)) \cos(\theta_2)\ \ \ o_z \sin(\theta_2)) \sin(\theta_3) +$$

$$((\ \ o_y \sin(\theta_1)\ \ \ o_x \cos(\theta_1)) \sin(\theta_2) + o_z \cos(\theta_2)) \cos(\theta_3)) \sin(\theta_5) + ((o_x \sin(\theta_1)$$

$$o_y \cos(\theta_1)) \sin(\theta_4) + (((\ \ o_y \sin(\theta_1)\ \ \ o_x \cos(\theta_1)) \sin(\theta_2) + o_z \cos(\theta_2)) \sin(\theta_3) +$$

$$(o_z \sin(\theta_2) + (o_y \sin(\theta_1) + o_x \cos(\theta_1)) \cos(\theta_2)) \cos(\theta_3)) \cos(\theta_4)) \cos(\theta_5)$$

$$\boldsymbol{R}(1,2) = \ \ \sin(\theta_6)$$

$$\boldsymbol{L}(2,2) = (((o_y \sin(\theta_1) + o_x \cos(\theta_1)) \sin(\theta_2) \quad o_z \cos(\theta_2)) \sin(\theta_3) +$$

$$((\ \ o_y \sin(\theta_1) \quad o_x \cos(\theta_1)) \cos(\theta_2) \quad o_z \sin(\theta_2)) \cos(\theta_3)) \sin(\theta_4) +$$

$$(o_x \sin(\theta_1) \quad o_y \cos(\theta_1)) \cos(\theta_4)$$

$$\boldsymbol{R}(2,2) = \cos(\theta_6)$$

Notice that all variables in $\boldsymbol{L}(1,2)$ and $\boldsymbol{L}(2,2)$ are known, make $k_1 = \boldsymbol{L}(1,2)$ and $k_2 = \boldsymbol{L}(2,2)$

$$\Rightarrow \begin{cases} k_1 = \quad \sin(\theta_6) \\ k_2 = \cos(\theta_6) \end{cases}$$

$$\Rightarrow \frac{\sin(\theta_6)}{\cos(\theta_6)} = \frac{k_1}{k_2} = \tan(\theta_6)$$

Therefore, the solution of θ_6 is:

$$\theta_6 = atan2(\ \ k_1, k_2) \tag{30}$$

Thus, six equations have been found that collectively yield the values needed to place and orientate the robot at any desired location. In addition, all the valid results of inverse kinematic should be within the joint rotation range respectively, as shown in Table 4.1. It is important to notice that this solution is only possible to obtain in this method because the last three joints of the robot are intersecting at a common point. Otherwise, it will not possible to solve for this kind of solution, and as a result, one will have to solve the matrices directly or by calculating the inverse of the matrix and solving for the unknowns. Most industrial robots have the intersecting wrist joint and a similar approach may be taken for the other robots.

From the above calculation process, it is easy to notice that the forward kinematic problem has only one solution, but the inverse kinematic problem usually has multiple groups of solution, as shown in Figure 4.2. A common principle called “Minimum energy

consuming principle" has been widely used to choose a group solution of inverse kinematic. The controller will choose a group of angles which has the minimum joint angles changing compare to the current position of the robot, because the less joint angle rotating result the less power consuming.

Table 4.1 Joint rotation range of Nachi Robot (SC300F-02)

Joint #	Rotation range
J1	$\pi \sim \pi$
J2	$0 \sim 1.67\pi$
J3	$0.67\pi \sim 0.33\pi$
J4	$\pi \sim \pi$
J5	$1.33\pi \sim 1.33\pi$
J6	$\pi \sim \pi$

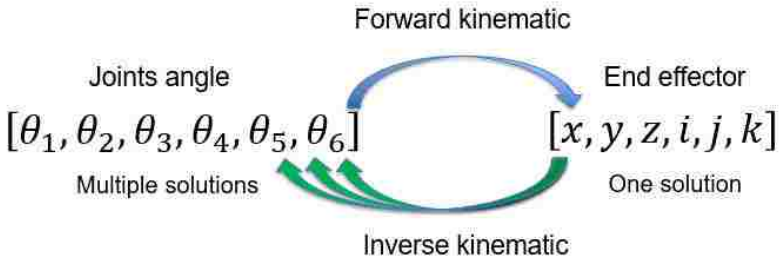

Figure 4.2 Solution difference between joints angle domain and end effector domain

5. JOINT ANGLE ERROR ON EFFECTOR'S POSITION ACCURACY

From the D-H model of Nachi robot, the center point of the robot's fixing plate relative to the robot base reference frame (Figure 5.1) can be described as following equation:

$$\boldsymbol{P} = \begin{bmatrix} x \\ y \\ z \\ 1 \end{bmatrix} = \boldsymbol{A_1 A_2 A_3 A_4 A_5 A_6 \ \ Tool} \tag{31}$$

$$\boldsymbol{A_i} = \begin{bmatrix} C\theta_i & S\theta_i C\alpha_i & S\theta_i S\alpha_i & a_i C\theta_i \\ S\theta_i & C\theta_i C\alpha_i & C\theta_i S\alpha_i & a_i S\theta_i \\ 0 & S\alpha_i & C\alpha_i & d_i \\ 0 & 0 & 0 & 1 \end{bmatrix} \tag{32}$$

$$\boldsymbol{Tool} = \begin{bmatrix} 0 \\ 0 \\ l \\ 1 \end{bmatrix} \tag{33}$$

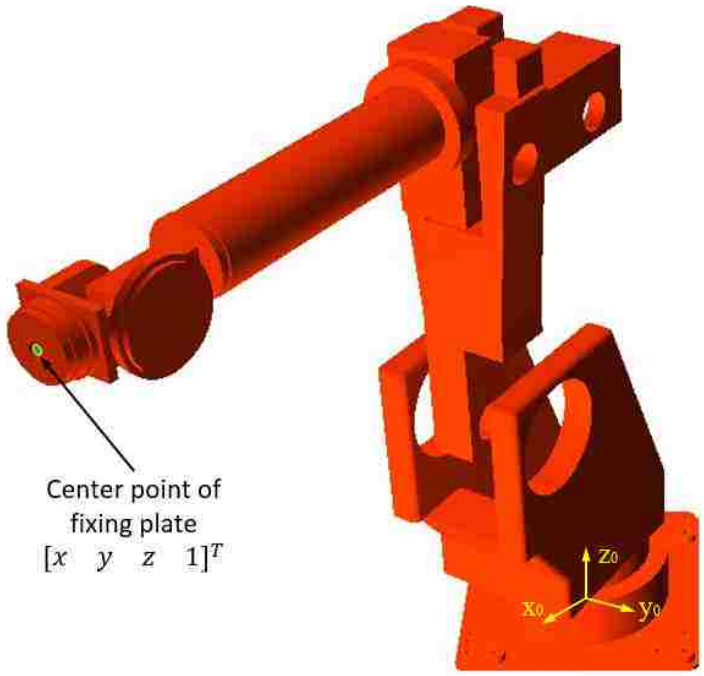

Figure 5.1 Center point of the robot's fixing plate relative to the robot base frame

In actual use, the kinematic parameters of the robot are normally different from the designed due to variety reasons, these difference come from the manufacturing, assembling, installation, sensors and even the temperature changing, finally these factors will lead to the position error of the end effector. Because the serial system structure of industrial robot, the error on each joint could be coupling and accumulating with each other. For the error on each joints, the ability to influence the final position error of the end effector is very different as well. Thus, a robot positon error model can be created to analyze the sensitivity of each joint with error as following:

$$\boldsymbol{A_{ir}} = \begin{bmatrix} C(\theta_i + \delta\theta_i) & S(\theta_i + \delta\theta_i)C(\alpha_i + \delta\alpha_i) & S(\theta_i + \delta\theta_i)S(\alpha_i + \delta\alpha_i) & (a_i + \delta a_i)C(\theta_i + \delta\theta_i) \\ S(\theta_i + \delta\theta_i) & C(\theta_i + \delta\theta_i)C(\alpha_i + \delta\alpha_i) & C(\theta_i + \delta\theta_i)S(\alpha_i + \delta\alpha_i) & (a_i + \delta a_i)S(\theta_i + \delta\theta_i) \\ 0 & S(\alpha_i + \delta\alpha_i) & C(\alpha_i + \delta\alpha_i) & d_i + \delta d_i \\ 0 & 0 & 0 & 1 \end{bmatrix} \quad (34)$$

$$\boldsymbol{Tool_r} = \begin{bmatrix} 0 \\ 0 \\ l + \delta l \\ 1 \end{bmatrix} \quad (35)$$

$$\boldsymbol{P_r} = \begin{bmatrix} x + \delta x \\ y + \delta y \\ z + \delta z \\ 1 \end{bmatrix} = \boldsymbol{A_{1r}A_{2r}A_{3r}A_{4r}A_{5r}A_{6r}} \quad \boldsymbol{Tool_r} \quad (36)$$

$$\boldsymbol{P} = |\boldsymbol{P_r P}| = \sqrt{(\delta x)^2 + (\delta y)^2 + (\delta z)^2} \quad (37)$$

$\boldsymbol{A_{ir}}$ and $\boldsymbol{Tool_r}$ are the transformation matrixes with kinematic parameters' error, $\boldsymbol{P_r}$ is the center point of the robot's fixing plate when considering the kinematic parameters' error of D-H model, $\boldsymbol{P}$ is the position difference between the theory coordinate value and coordinate value with parameters' error.

Based on the equations of robot positon error model, a D-H model parameter error analysis simulation system can be programmed with Python, the flow chart of this simulation analysis system as shown in Figure 5.2.

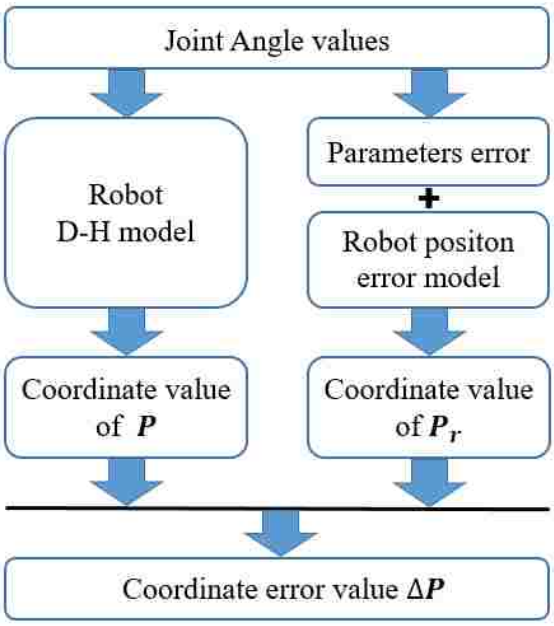

Figure 5.2 Flow chart of D-H model parameter error analysis simulation system

For the error on each joints, the influence on final position error of the end effector is varied at different position and orientation. In order to study the difference of these influence, the control variable method and unified error input method has been adopted. Set the joint value as [90° 70° 20° 0° 50° 90°], this is a typical position and orientation of robot for deposition or machining process, as shown in Figure 5.3.

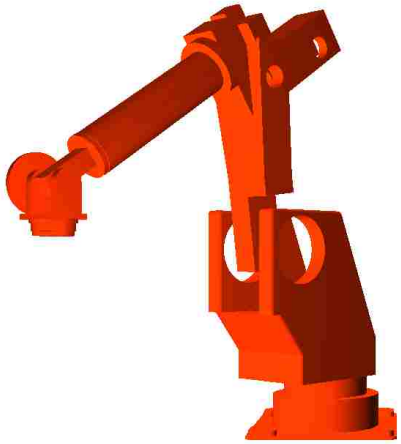

Figure 5.3 Typical position and orientation of robotic deposition or machining process

Use this as the robot's basic position and orientation, only rotate one joint at one time within its rotation range and keep other joints fixed, assume there is a joint angle error which value is 0.01°, calculate the coordinate error at every 1° angle changing, apply this error on each joint respectively, thus a figure with six error curves according to each joint can be obtained. Repeat this process for other joints, similar figures of error curves can be obtained, as shown in Figure 5.4.

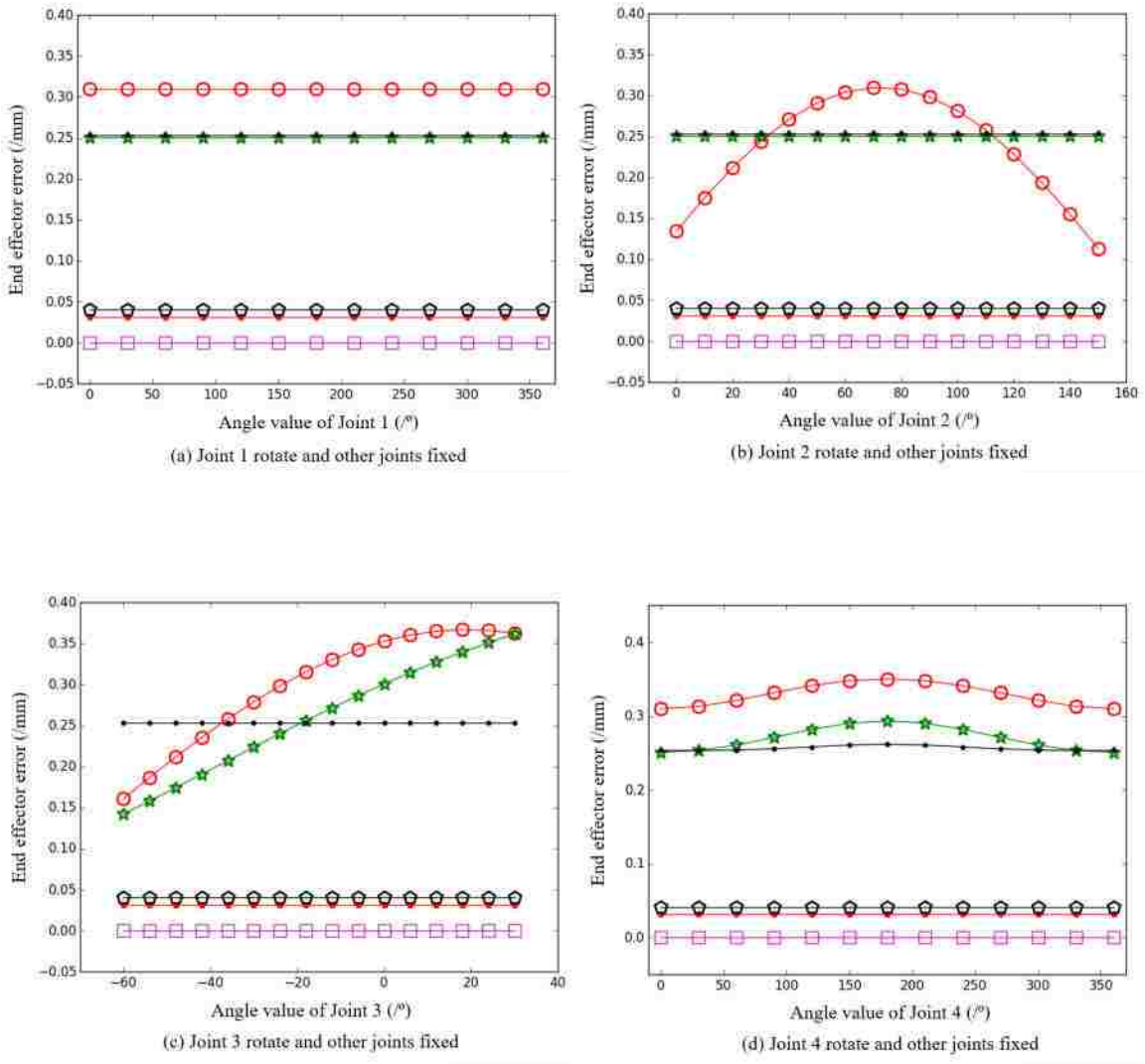

Figure 5.4 End effector error distribution when joints rotate with unified angle error

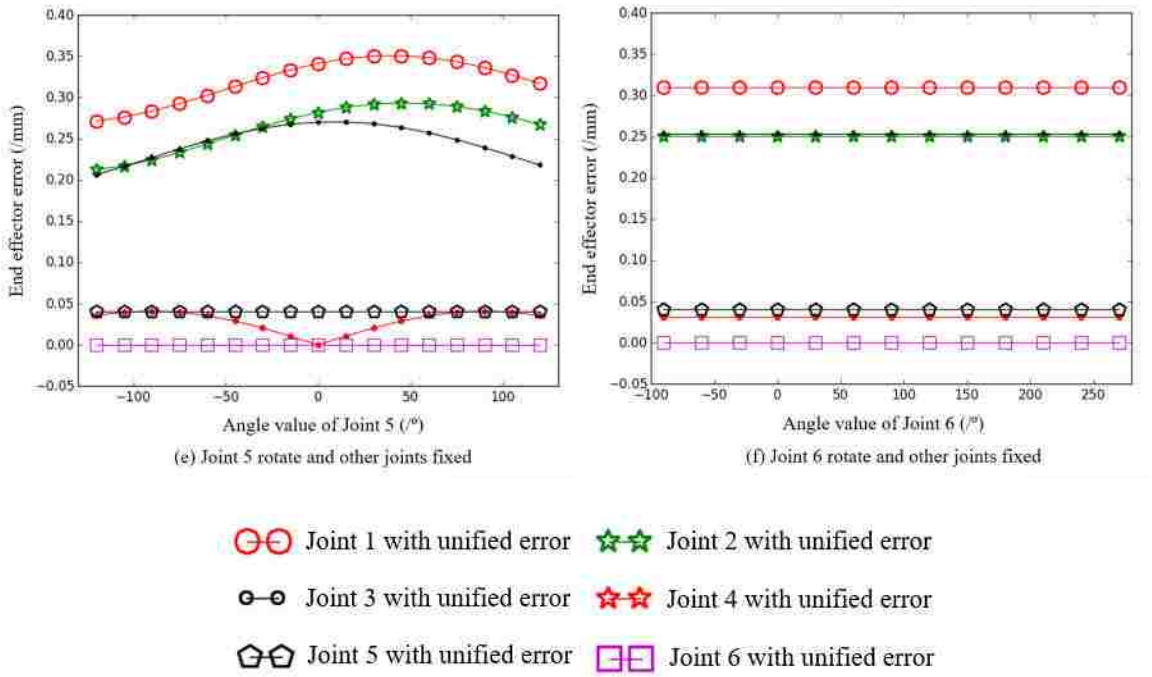

Figure 5.4 End effector error distribution when joints rotate with unified angle error (cont.)

When joint 1 rotates from 0° to 360°, meanwhile other joints are fixed. Apply the 0.01° joint angle error on each joints respectively, the resulting end effector error distribution as shown in Figure 5.4 (a). The figure shows that when only joint 1 rotates, the end effector error caused by angle error on different joints are constant, these values don't change with the changing of position and orientation of joint 1. For the influence on final position error of different joint error, the effect of weights sorted descend as 1, 3, 2, 5, 4, 6.

When joint 2 rotates from 0° to 150°, meanwhile other joints are fixed. Apply the 0.01° joint angle error on each joints respectively, the resulting end effector error distribution as shown in Figure 5.4 (b). The figure shows that when only joint 2 rotates, the end effector error caused by angle error on joint 1 is varied and reach its maximum at the middle value of the joint 2 rotation angle, the end effector error caused by angle error on

other joints are constant, these values don't change with the changing of position and orientation of joint 2. For the influence on final position error of different joint error, the effect of weights sorted descend as 3, 2, 1, 5, 4, 6.

When joint 3 rotates from 60° to 30°, meanwhile other joints are fixed. Apply the 0.01° joint angle error on each joints respectively, the resulting end effector error distribution as shown in Figure 5.4 (c). The figure shows that when only joint 3 rotates, the end effector error caused by angle error on joint 1, 2 are varied, the end effector error caused by angle error on other joints are constant, these values don't change with the changing of position and orientation of joint 3. For the influence on final position error of different joint error, the effect of weights sorted descend as 1, 2, 3, 5, 4, 6.

When joint 4 rotates from 0° to 360°, meanwhile other joints are fixed. Apply the 0.01° joint angle error on each joints respectively, the resulting end effector error distribution as shown in Figure 5.4 (d). The figure shows that when only joint 4 rotates, the end effector error caused by angle error on joint 1, 2, 3 are varied, the end effector error caused by angle error on other joints are constant, these values don't change with the changing of position and orientation of joint 4. For the influence on final position error of different joint error, the effect of weights sorted descend as 1, 2, 3, 5, 4, 6.

When joint 5 rotates from 120° to 120°, meanwhile other joints are fixed. Apply the 0.01° joint angle error on each joints respectively, the resulting end effector error distribution as shown in Figure 5.4 (e). The figure shows that when only joint 5 rotates, the end effector error caused by angle error on joint 1, 2, 3, 4 are varied, the end effector error caused by angle error on other joints are constant, these values don't change with the

changing of position and orientation of joint 5. For the influence on final position error of different joint error, the effect of weights sorted descend as 1, 2, 3, 5, 4, 6.

When joint 6 rotates from 0° to 360°, meanwhile other joints are fixed. Apply the 0.01° joint angle error on each joints respectively, the resulting end effector error distribution as shown in Figure 5.4(f). The figure shows that when only joint 6 rotates, the end effector error caused by angle error on different joints are constant, these values don't change with the changing of position and orientation of joint 6. For the influence on final position error of different joint error, the effect of weights sorted descend as 1, 3, 2, 5, 4, 6.

Sum up all these position error together and calculate the average position error caused by each joint respectively, the results as shown in Table 5.1. As can be seen from the data in Table 5.1, even a tiny joint error can lead to a significant end effector position error. The sensitivity of joint error influence on end effector position error is different, for the serial manipulator type industrial robot, the joint errors exist on arm joints have more obvious effect on position error of end effector than the joint errors exist on wrist joints. For the total influence on final position error of different joint errors, the effect of weights sorted descend as 6, 5, 4, 2, 3, 1.

Table 5.1 Average position error (/mm) caused by each joint and joint error sensitivity rank

	Joint 1	Joint 2	Joint 3	Joint 4	Joint 5	Joint 6
Average position error	0.301	0.257	0.252	0.030	0.0410	0.0000
Sensitivity rank	6	5	4	2	3	1

In order to increase the accuracy of industrial robot, precise manufactured parts and high resolution sensors can be used to reduce the joint angle error, but adopt these expensive parts for the whole robot system will make the cost surge. The analysis of joint error sensitivity can be helpful for making a decision of balancing the cost and accuracy. Take this Nachi robot as an example, utilize high performance parts and sensors on joint 1 will improve the system accuracy mostly.

6. INDUSTRIAL ROBOT TRAJECTORY ACCURACY MAPPING

Normally, the users pay attention to movement accuracy when robot perform certain trajectory, and simply believe that the more accurate of the robot system, the better result will be obtained. It is important to notice that the kinematic parameters error cannot be eliminate from the robot system completely, even after calibration, these errors still exist and will be varied during running, so the conventional error compensation method is not a "once and for all" solution. For a certain working path, it can be performed at multiple positions and orientations within robot working envelop, based on the robot kinematic and joint sensitivity analysis, a visualized evaluation map can be obtained to describe the accuracy difference of trajectory at different positions and orientations. This method can help the user to find the best position and orientation to perform a working path, it can also make the maximum usage of current accuracy ability of a specific robot rather than blindly pursuit higher accuracy.

Any working path performed by robot is composed of angle changing in joints domain, the angle changing is related with the trajectory itself, as well as with its location and orientation. When an error is present, each joint has different sensitivity on affecting the position error of end effector. Thus, a trajectory accuracy evaluation function for Nachi Robot (SC300F-02) can be created as following:

$$E = \sum_{i=1}^{6} w_i \Delta\theta_i = \begin{bmatrix} w_1 & w_2 & w_3 & w_4 & w_5 & w_6 \end{bmatrix} \begin{matrix} \Delta\theta_1 \\ \Delta\theta_2 \\ \Delta\theta_3 \\ \Delta\theta_4 \\ \Delta\theta_5 \\ \Delta\theta_6 \end{matrix} \tag{37}$$

w_i is the effect weight of different joints influence on position of end effector, $\Delta\theta_i$ is the joint angle changing for a specific working path at certain position and orientation.

For a simple working path, let the end effector move a 50mm straight line along y-axis from negative to positive in robot system coordinate, there are multiple positions available to conduct this task within robot working envelop, as shown in Figure 6.1.

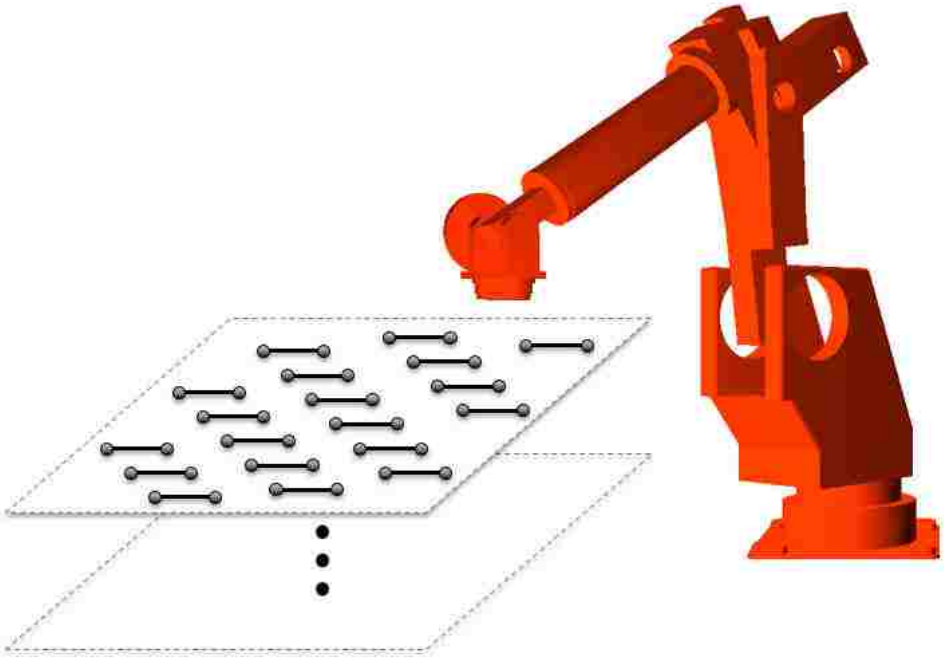

Figure 6.1 Multiple positions choice for robot conduct a specific trajectory

Apply the trajectory accuracy evaluation method for this task, separate working area into small testing patches ($50\text{mm} \times 50\text{mm}$) within the x range is from -700 to 700, y range is from -1200 to -2000, z takes 800, 1200, 1600, and 2000, respectively, in robot system coordinate. The robot trajectory accuracy evaluation mapping results for a 50 mm straight line in these laminated 2D working areas are as shown in Figure 6.2.

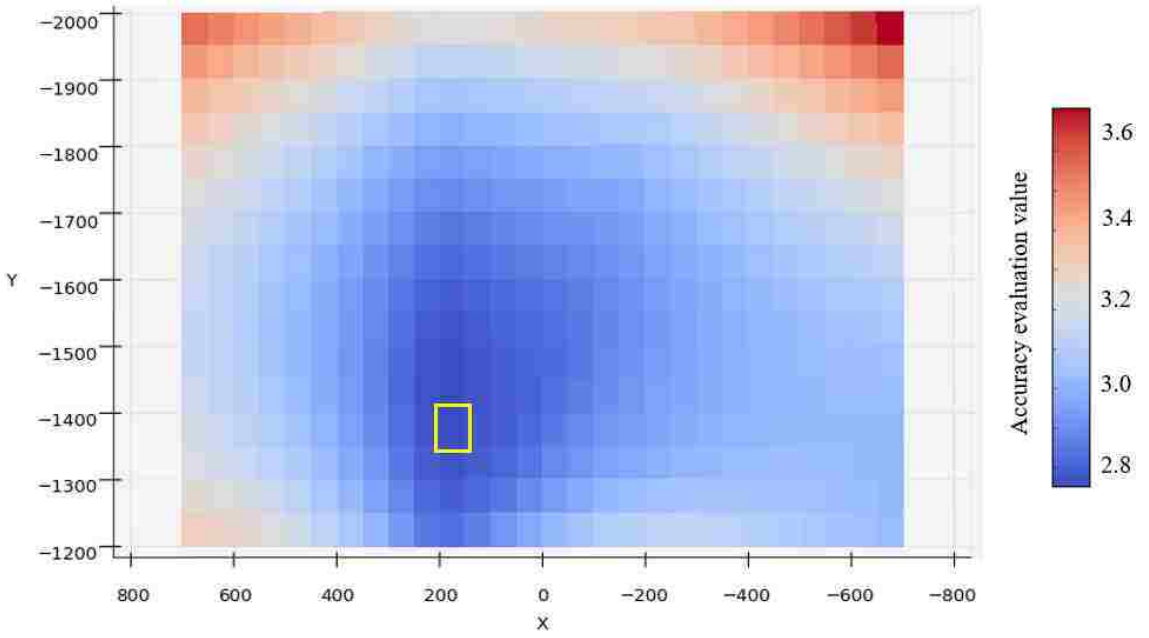

(a) X(-700,700), Y(-1200, -2000), Z=800

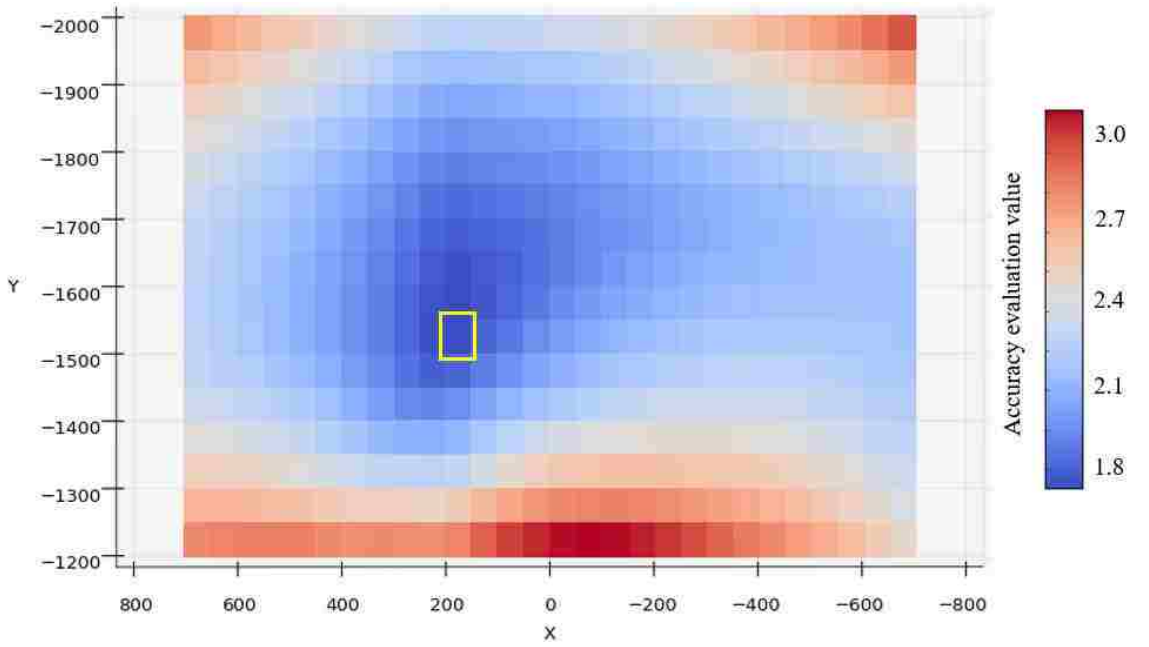

(b) X(-700,700), Y(-1200, -2000), Z=1200

Figure 6.2 Trajectory accuracy evaluation mapping result for straight line in 2D working area

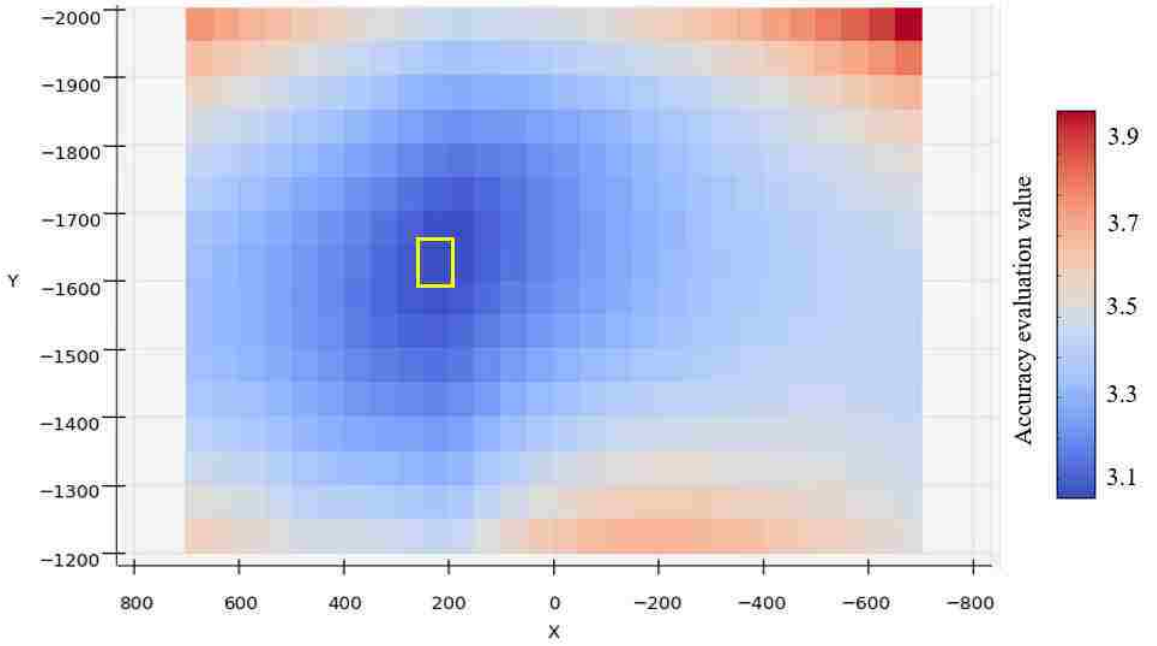

(c) X(-700,700), Y(-1200, -2000), Z=1600

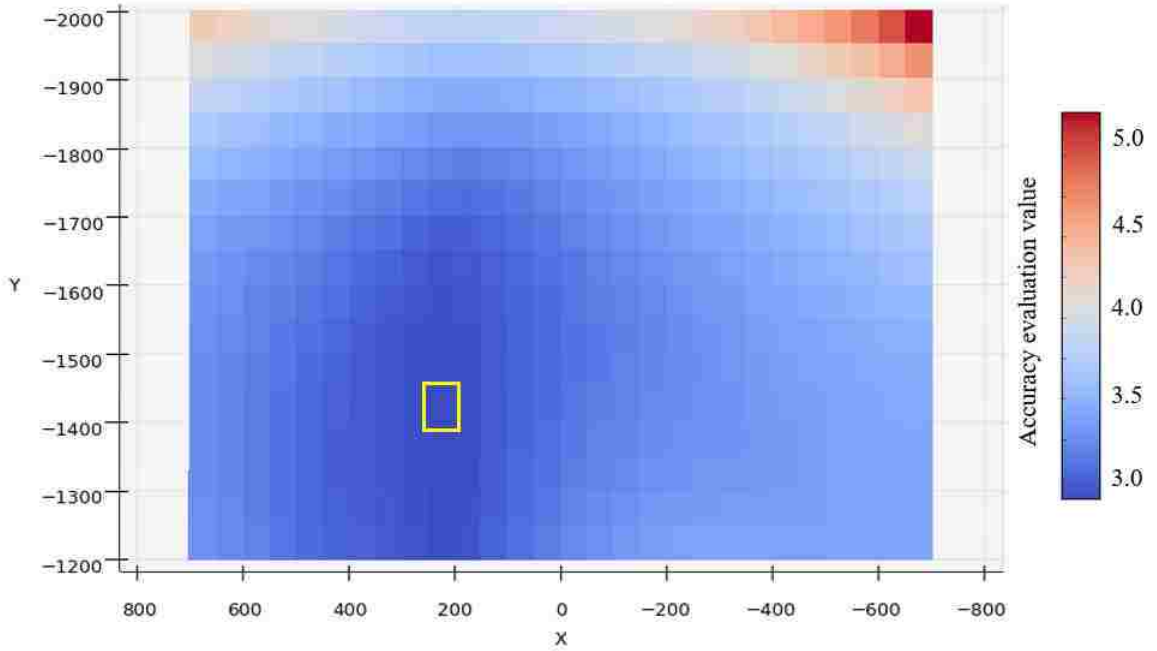

(d) X(-700,700), Y(-1200, -2000), Z=2000

Figure 6.2 Trajectory accuracy evaluation mapping result for straight line in 2D working area (cont.)

As can be seen from Figure 6.2, for same height, which means z value is constant, each patch has different accuracy evaluation value for a specific trajectory, the less

evaluation value of patch is, the better accuracy can be obtained at this position. The patch surrounded by rectangle shape indicate the best position to perform this task. The best position is varied along with changing of z value.

In order to verify the correctness of accuracy evaluation, the drawing experiments have carried out.

Employ the parameter settings the in Figure 6.2 (a) as an example, set up the position of working table and white paper with grid in the robot working envelop, as shown in Figure 6.3.

Figure 6.3 Experiments set up for accuracy evaluation of robot drawing straight line

According to the accuracy evaluation results shown in Figure 6.2 (a), let the robot draw 50mm straight line in the patch with best accuracy and in the patch with worst accuracy respectively.

Repeat this process for 10 times and record the measurement data as shown in Figure 6.4.

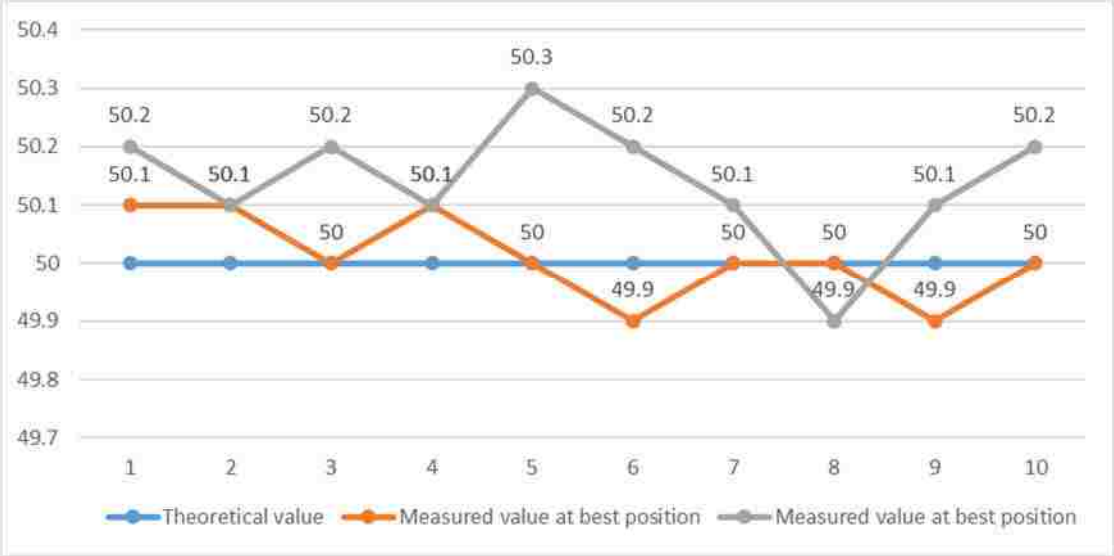

Figure 6.4 Experiments value (mm) for accuracy evaluation of robot drawing

As can be seen from Figure 6.4, the average measurement value at the best accuracy position and the worst accuracy position are 50.01mm and 50.14mm, the standard deviation of two sets of data are 0.074 and 0.107, respectively. The difference between two standard deviations is 31%.

The accuracy evaluation of the best accuracy position and the worst accuracy position with the parameter settings in Figure 6.2 (a) are 2.65 and 3.74, the difference between two accuracy evaluation values is 29%, which is close to the difference of standard deviations of experiments value. Thus the experiments result shows that the accuracy evaluation value could reflect the trajectory accuracy difference within robot working envelope at different positions. It is easy to notice that in Figure 6.1, all the directions of the straight lines are along the y axis of robot system coordinate, it is also the common direction when the users assign a working path for robot. Obviously, this straight line can be drawn in multiple directions from a same start point, and the different direction will cause different joint angle changing, as shown in Figure 6.5.

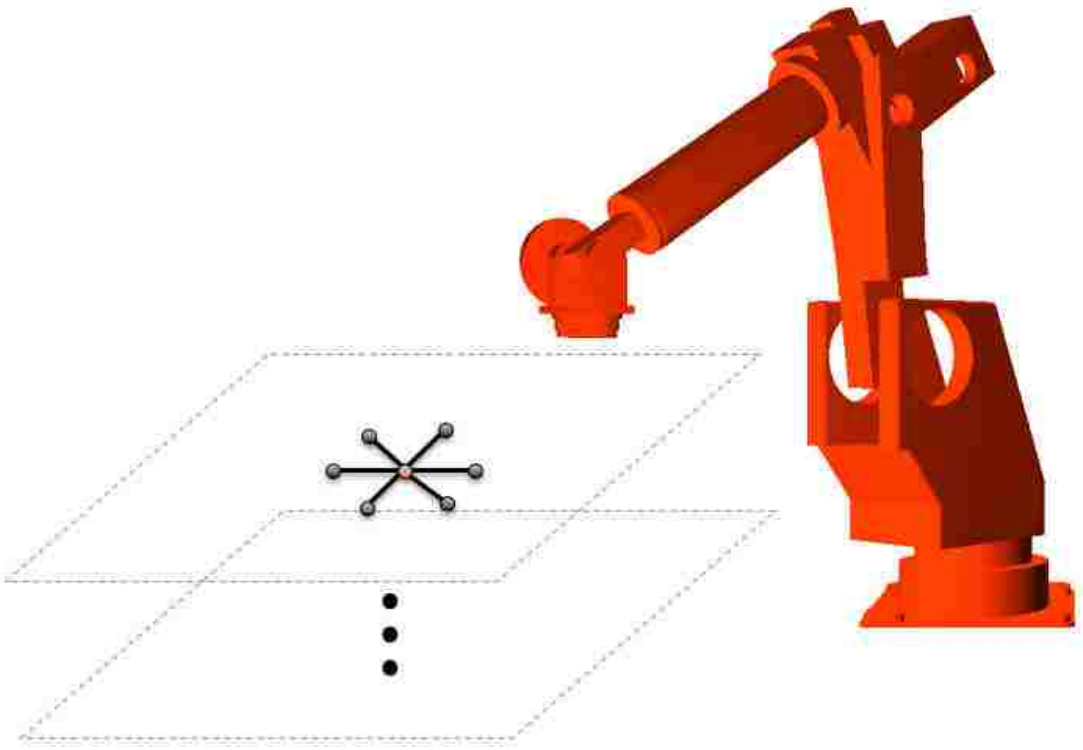

Figure 6.5 Multiple direction possibilities for robot conduct a specific trajectory

Apply the trajectory accuracy evaluation method for this situation, set the angle changing 30° every position from 0° to 360°, the start point is (200, -1500, 1200) in robot system coordinate, the length of line is 50 mm.

The robot trajectory accuracy evaluation results for these lines toward different directions as shown in Figure 6.6.

The 50 mm straight line start from the same point toward different directions have different accuracy evaluation value, the color range from red to green indicates the accuracy evaluation value as descending, the less evaluation value of line is, the better accuracy can be obtained at this orientation.

The lowest accuracy evaluation value is plotted as the thicker green arrow, it represents the best orientation to perform this task.

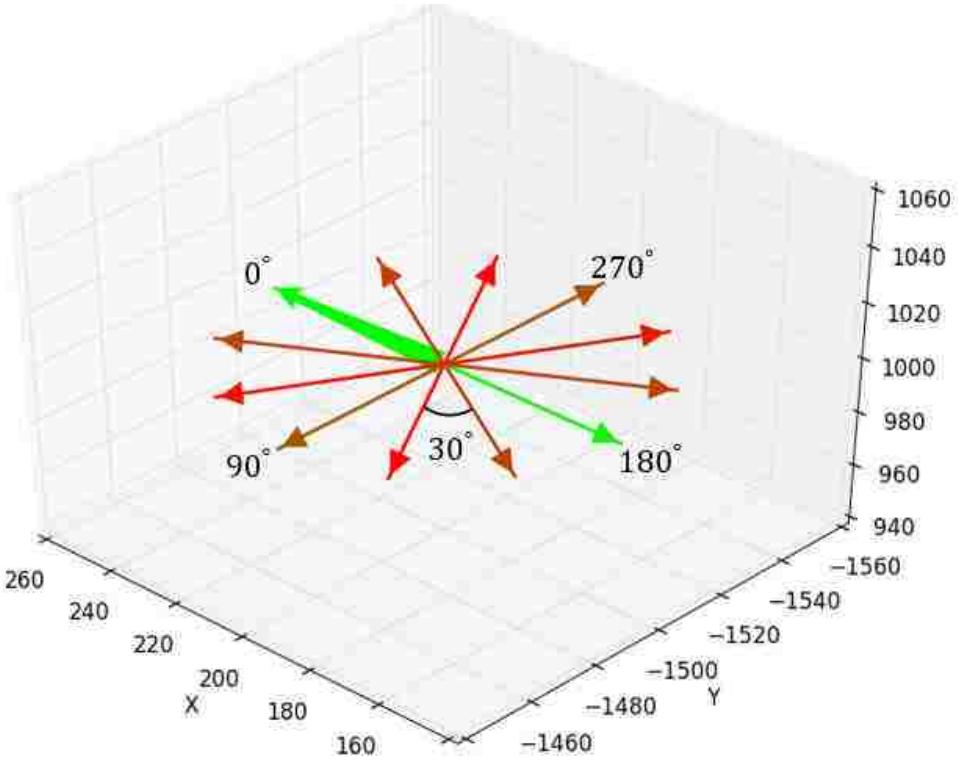

Figure 6.6 Trajectory accuracy evaluation mapping result for straight line towards different directions

In order to observe the affection of orientation on trajectory accuracy in the working envelop of robot, separate working area into small testing patches ($120\text{mm} \times 120\text{mm}$) within the x range is from -600 to 600, y range is from -1200 to -1800, z takes 800, 1200, 1600, and 2000, respectively, in robot system coordinate.

Then apply the same analysis process to these multiple centers, the robot trajectory accuracy evaluation mapping results for 50 mm straight line starts from the same point towards different directions in laminated 2D working areas are as shown in Figure 6.7.

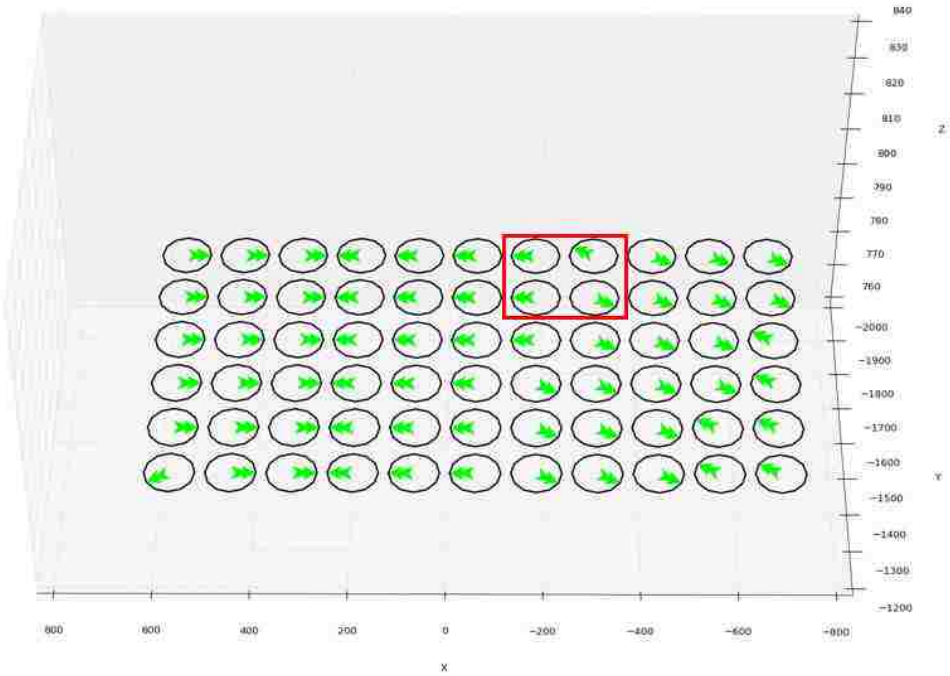

(a) X(-600,600), Y(-1200, -1800), Z=800

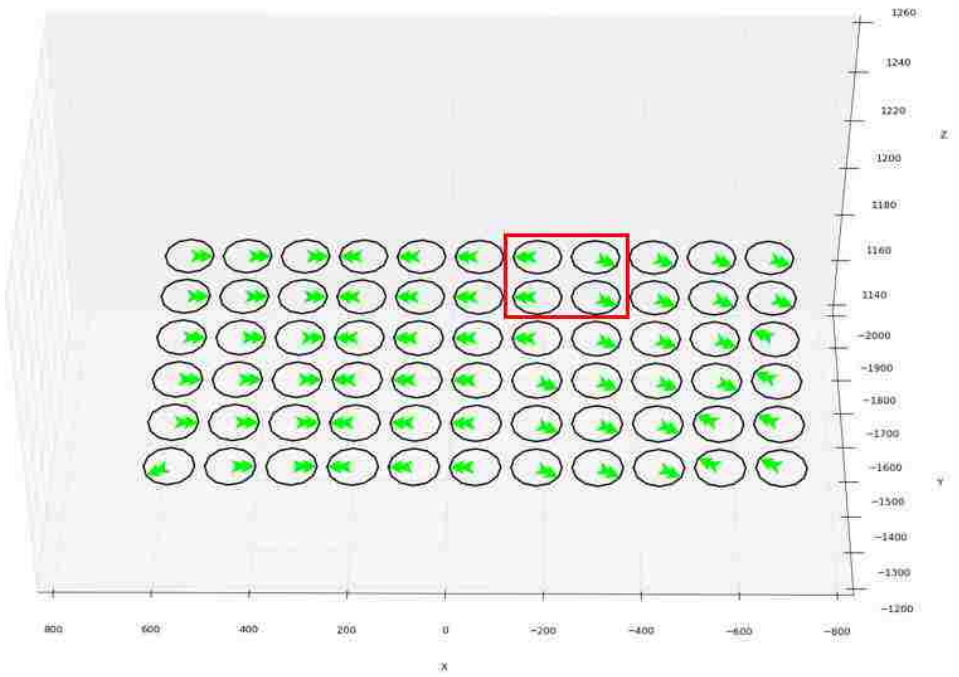

(b) X(-600,600), Y(-1200, -1800), Z=1200

Figure 6.7 Trajectory accuracy evaluation mapping result for straight line orientation analysis

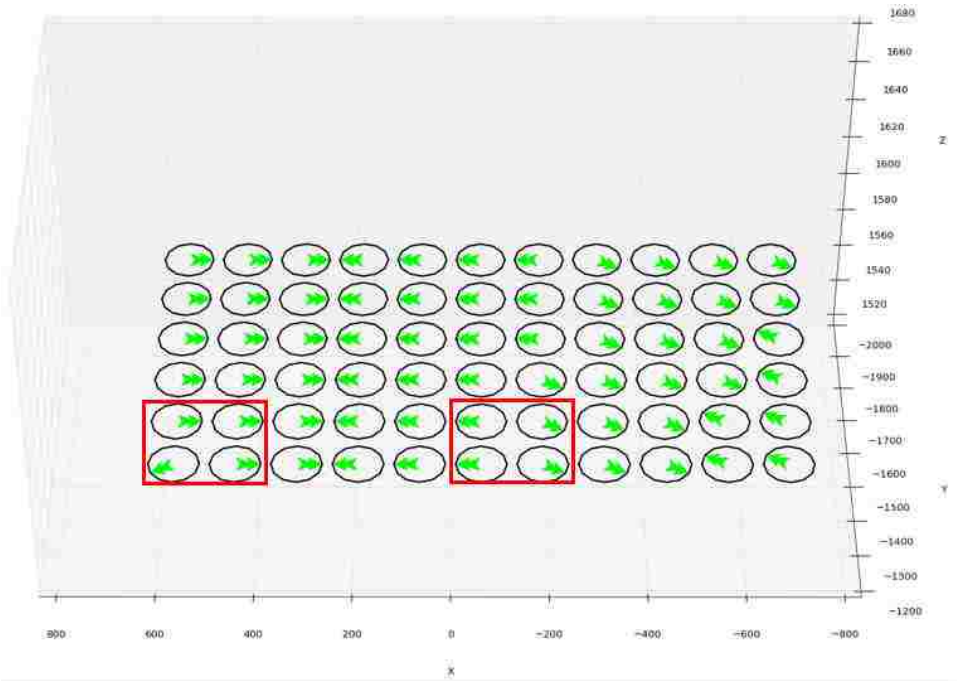

(c) X(-600,600), Y(-1200, -1800), Z=1600

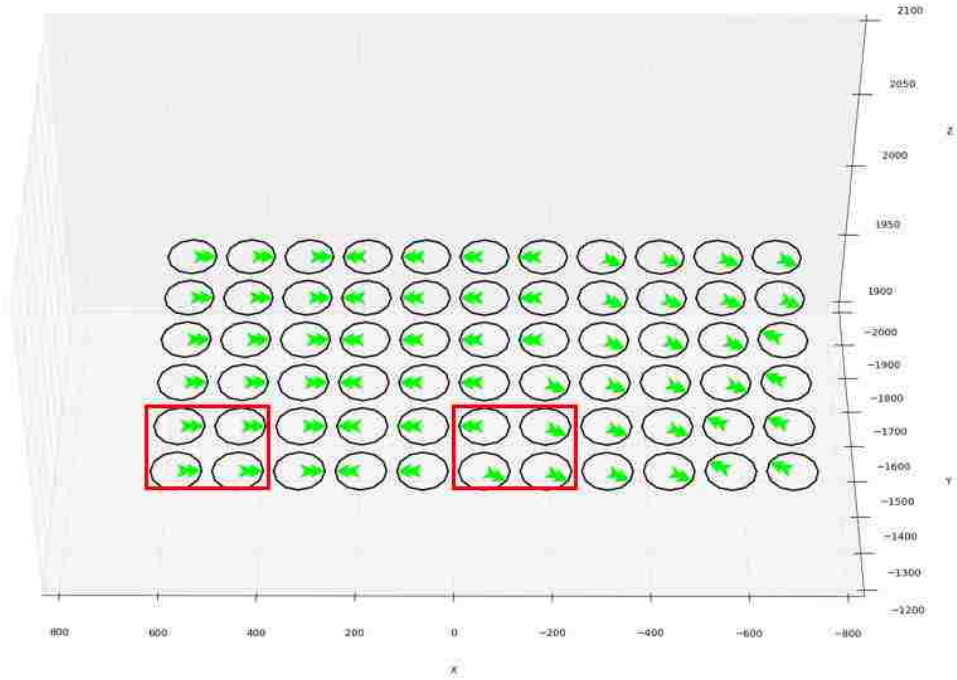

(d) X(-600,600), Y(-1200, -1800), Z=2000

Figure 6.7 Trajectory accuracy evaluation mapping result for straight line orientation analysis (cont.)

As can be seen from Figure 6.7, at the same height, which means z value is constant, the best orientation for move a straight line are varied in different regions. For same x, y coordinates, the best orientation could be changed according to the changing of z value, as the red rectangle bounded area shown in these figures. Thus, the best position and orientation in 3D working envelop to perform a certain working path can be found by taking enough accuracy evaluation calculation.

7. SIMULATION: TRAJECTORY ACCURACY MAPPING OF A ROBOTIC HYBRID MANUFACTURING WORKING PATH

The zigzag path is a typical trajectory for robotic hybrid manufacturing as shown in Figure 7.1. One layer of this kind path could work for machining or milling process, multiple layers of that could be used as a deposition working path.

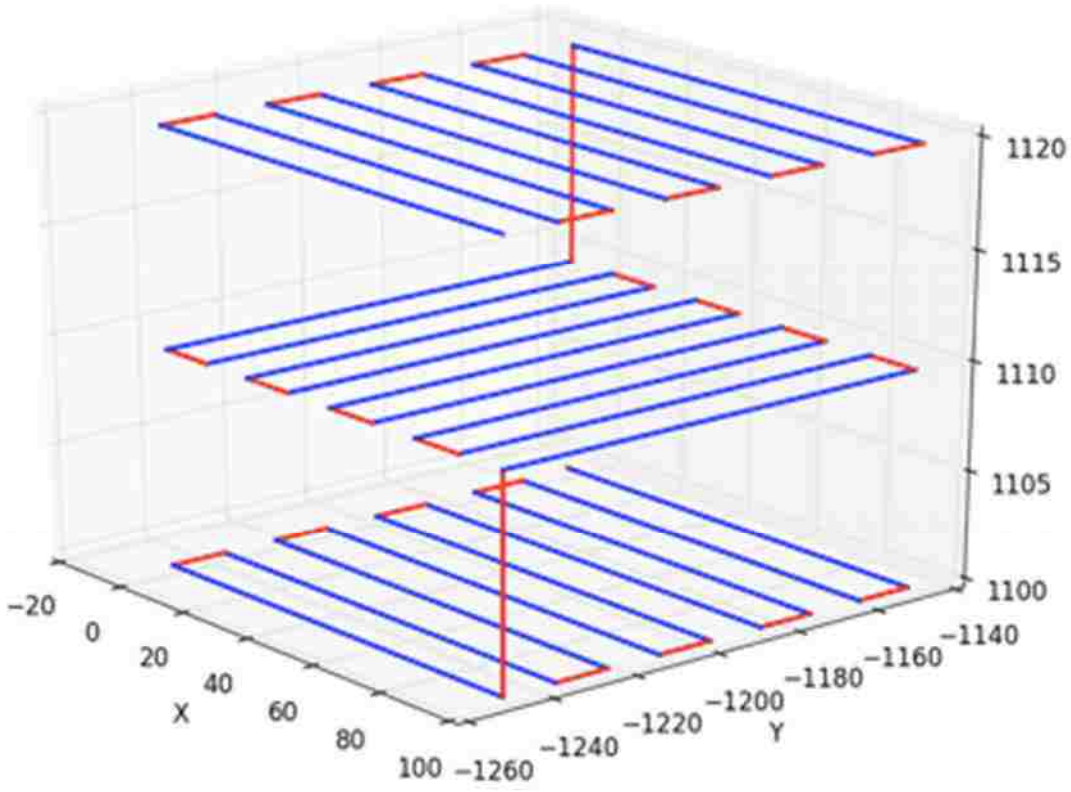

Figure 7.1 Zigzag path for hybrid manufacturing

The simulation will take this zigzag path as an example, use the above discussed trajectory accuracy mapping method to find the best position and orientation to conduct this task within Nachi Robot's (SC300F-02) working envelop (Figure 7.2).

Also analyze the actual dimension error and possibility of reaching a deposition tolerance requirements according to a group of known joints error.

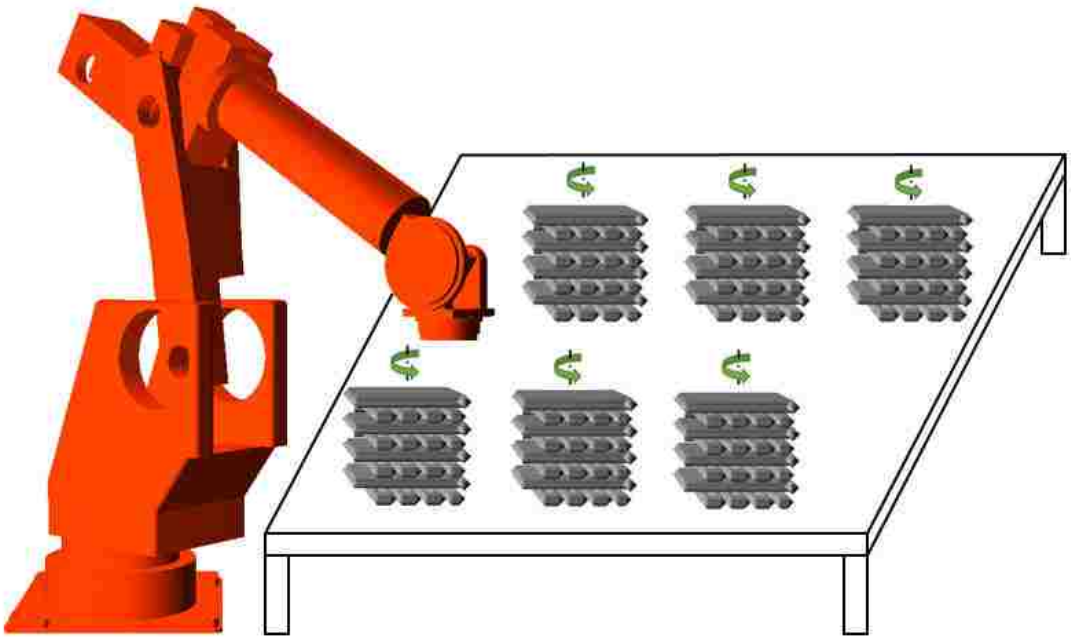

Figure 7.2 Multiple position and orientation possibilities for a zigzag path

In order to study how zigzag trajectory's position and orientation affect its accuracy in the working envelop of robot. The trajectory's accuracy evaluation value should be calculated at different position while with different orientation with robot working envelop.

Firstly, separate working volume into small testing cube area ($50\text{mm} \times 50\text{mm} \times 50\text{mm}$) within the in robot system coordinate.

Specifically, x range is from -500 to 500, y range is from -1200 to -1800, z range is from 800 to 1400.

Thus there are 45 testing cube areas within robot working envelop, as shown in Figure 7.3.

The dimension of deposition zigzag path is $10\text{mm} \times 10\text{mm} \times 1\text{mm}$, layer thickness is 0.1 mm, track width is 2 mm and overlap is 0.3.

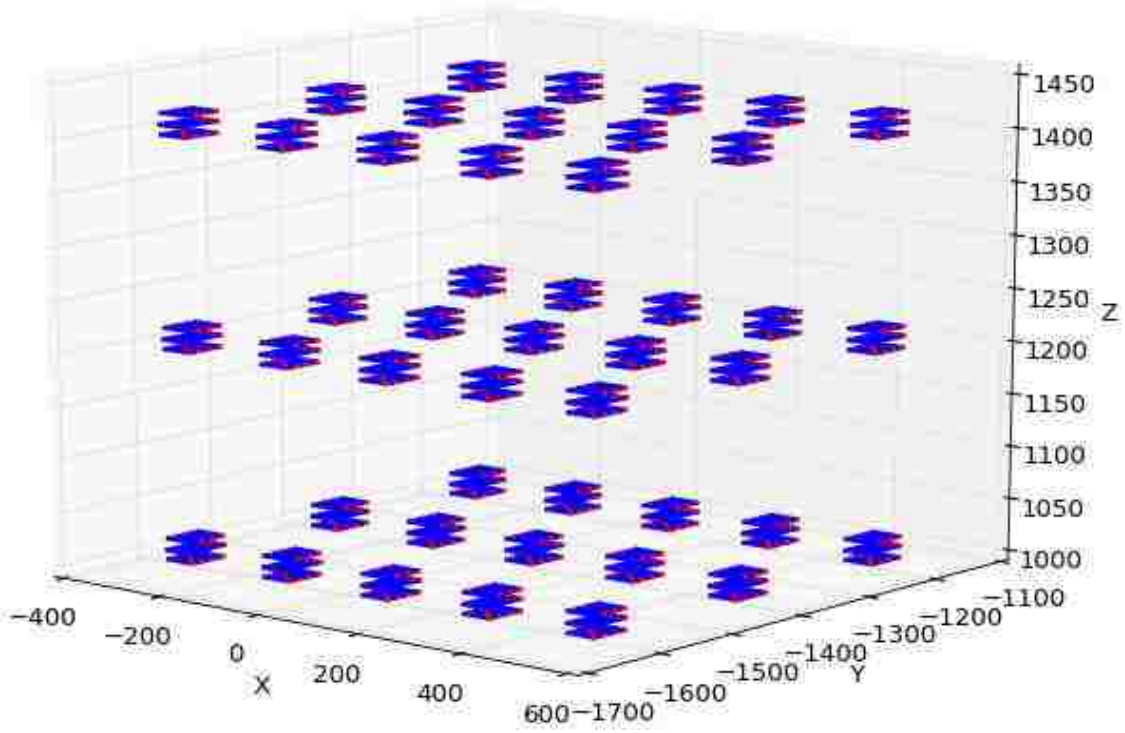

Figure 7.3 Trajectory testing cube within robot working envelop

Secondly, set the orientation angle for these trajectories:

Start from x axis positive direction, rotate about z axis counterclockwise, take the angle value as 0°, 30°, 60°, 90°, 120°, 150°, 180°, 210°, 240°, 270°, 300°, 330°, respectively.

Then apply the trajectory accuracy mapping process to every line segments of the zigzag trajectories.

Sum these up as robot trajectory accuracy evaluation value of this trajectory, the results are respectively shown in Table 7.1.

Plot the testing cube area with the normalized evaluation values in angle group, the trajectory accuracy mapping results for this task as shown in Figure 7.4.

Table 7.1 Zigzag trajectories accuracy evaluation value

Poistion	Rotation angle (°)											
No.	0	30	60	90	120	150	180	210	240	270	300	330
1	513.73	544.44	600.52	514.68	543.87	598.28	513.70	544.50	600.83	514.97	544.02	598.26
2	449.73	486.91	537.52	450.33	486.04	535.57	449.73	486.90	537.82	450.53	486.15	535.58
3	418.42	458.35	504.35	418.92	457.10	502.23	418.42	458.30	504.41	419.04	457.21	502.23
4	482.79	591.78	598.75	483.24	590.82	596.77	482.75	591.80	599.02	483.51	590.90	596.81
5	415.23	520.59	534.87	415.44	519.39	533.27	415.23	520.59	535.16	415.59	519.50	533.27
6	382.97	484.43	499.07	383.08	482.87	497.38	382.97	484.40	499.19	383.19	482.98	497.37
7	494.84	610.41	571.85	494.79	608.92	570.37	494.81	610.63	572.11	494.96	608.99	570.40
8	425.68	538.09	514.81	425.50	536.55	513.60	425.68	538.09	515.07	425.61	536.66	513.60
9	386.03	500.67	483.25	385.73	498.75	481.91	386.03	500.61	483.36	385.84	498.86	481.91
10	532.61	599.25	522.45	532.12	597.21	521.56	532.58	599.51	522.70	532.21	597.30	521.58
11	461.10	539.73	479.53	460.51	537.84	478.68	461.10	539.98	479.68	460.62	537.95	478.68
12	421.69	506.31	458.00	420.98	503.98	457.02	421.69	506.20	458.11	421.09	504.08	457.02
13	542.77	571.76	466.45	541.87	570.01	466.02	542.75	572.02	466.58	541.97	570.03	466.04
14	482.07	527.45	434.70	481.07	525.64	434.22	482.07	527.68	434.82	481.19	525.64	434.22
15	447.82	503.16	427.43	446.67	500.73	426.81	447.81	503.05	427.54	446.78	500.73	426.81
16	517.89	547.34	608.58	518.73	546.65	606.57	518.11	547.56	609.16	519.30	547.09	606.55
17	448.80	480.57	534.86	449.32	479.67	533.27	448.99	480.77	535.31	449.67	479.97	533.07
18	418.38	452.09	498.91	418.78	450.75	496.95	418.50	452.09	498.99	419.04	451.01	496.78
19	485.20	598.96	609.26	485.57	597.84	607.53	485.41	599.17	609.82	486.13	598.18	607.32
20	409.20	516.04	532.82	409.35	514.81	531.54	409.39	516.23	533.27	409.67	515.11	531.34
21	383.19	477.86	493.14	383.22	476.22	491.73	383.33	477.88	493.42	383.49	476.49	491.56
22	497.96	617.57	580.39	497.84	616.03	579.16	498.16	618.07	580.94	498.28	616.37	578.95
23	418.31	534.70	512.48	418.07	533.13	511.54	418.50	534.89	512.88	418.39	533.45	511.34
24	381.87	493.63	477.77	381.52	491.64	476.70	382.01	493.63	478.05	381.79	491.92	476.54
25	533.36	603.66	523.84	532.78	601.76	523.20	533.56	604.20	524.36	533.13	601.86	523.00
26	453.99	535.06	476.23	453.35	533.18	475.64	454.17	535.32	476.55	453.67	533.44	475.46
27	414.20	498.61	453.88	413.41	496.24	453.16	414.31	498.62	454.16	413.68	496.51	453.00
28	538.97	570.86	460.17	537.98	569.38	459.97	539.15	571.39	460.52	538.33	569.20	459.79
29	475.20	521.08	430.48	474.15	519.48	430.25	475.37	521.38	430.79	474.47	519.32	430.08
30	439.15	494.75	424.61	437.89	492.47	424.24	439.21	494.78	424.89	438.16	492.35	424.09
31	497.12	517.68	582.44	497.66	517.01	581.32	497.62	518.17	583.28	498.43	517.69	581.23
32	437.95	462.20	516.80	438.26	461.20	515.52	438.26	462.42	517.11	438.74	461.67	515.24
33	411.88	437.47	488.94	412.07	436.07	487.19	412.04	437.63	489.10	412.48	436.48	486.86
34	455.38	569.26	586.35	455.56	568.22	585.46	455.88	569.75	587.21	456.33	568.85	584.96
35	399.03	495.83	513.15	399.04	494.57	512.34	399.38	496.09	513.65	399.54	495.06	511.93
36	377.59	461.69	482.91	377.44	460.01	481.81	377.77	461.85	483.27	377.86	460.43	481.47
37	468.85	588.43	558.90	468.63	587.03	558.38	469.32	588.93	559.74	469.30	587.66	557.90
38	398.21	513.68	493.72	397.88	512.10	493.21	398.56	513.91	494.24	398.39	512.61	492.82
39	376.18	476.75	467.89	375.65	474.75	467.18	376.35	476.91	468.33	376.08	475.18	466.85
40	503.44	578.48	504.20	502.82	577.28	504.04	503.87	579.30	504.89	503.44	577.41	503.60
41	434.48	514.28	460.77	433.75	512.54	460.56	434.78	514.46	461.29	434.27	512.86	460.20
42	403.45	482.23	444.92	402.52	479.88	444.52	403.61	482.39	445.36	402.95	480.30	444.21
43	513.70	546.94	436.79	512.70	546.04	436.99	514.08	547.62	437.39	513.30	545.65	436.60
44	455.29	501.50	420.15	454.13	500.11	420.26	455.52	501.72	420.65	454.63	499.78	419.92
45	426.86	480.38	416.91	425.49	478.27	416.84	427.02	480.53	417.34	425.91	478.11	416.56

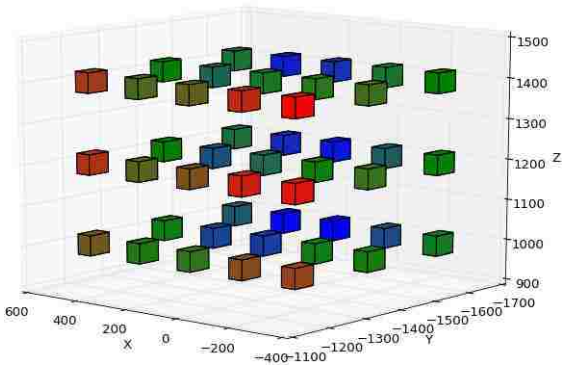

(a) Trajectory rotate angle equals 0°

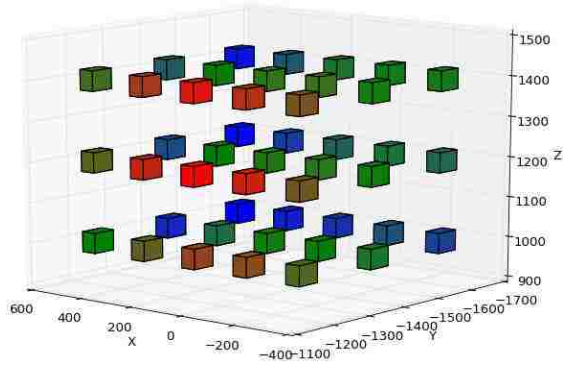

(b) Trajectory rotate angle equals 30°

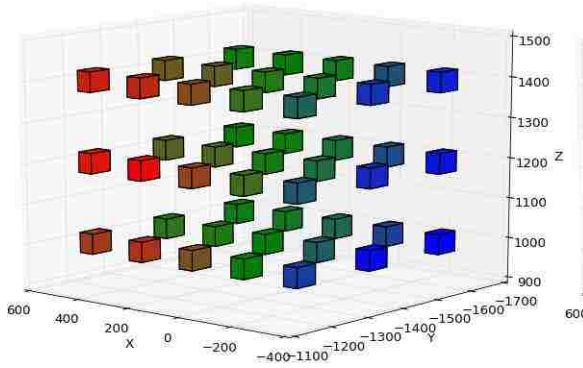

(c) Trajectory rotate angle equals 60°

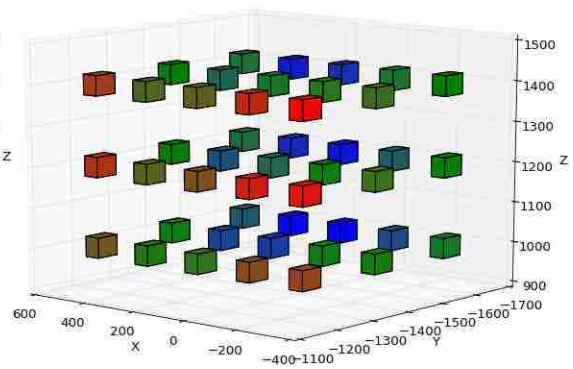

(d) Trajectory rotate angle equals 90°

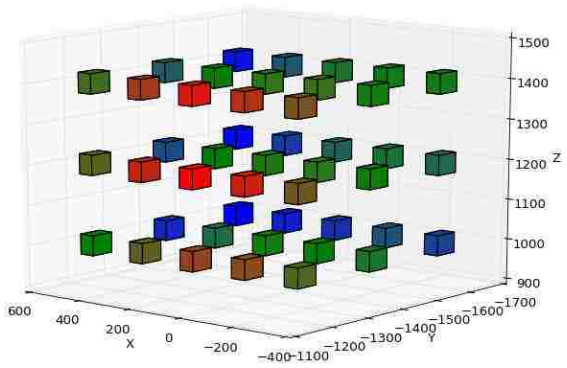

(e) Trajectory rotate angle equals 120°

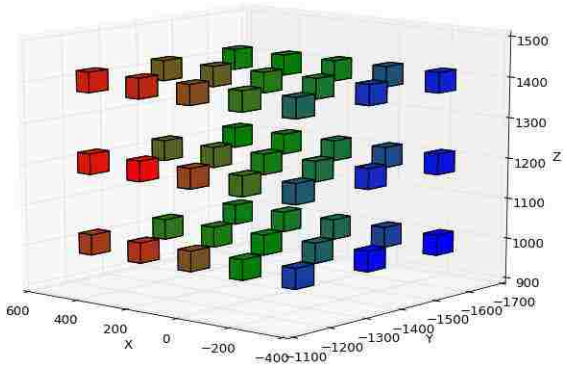

(f) Trajectory rotate angle equals 150°

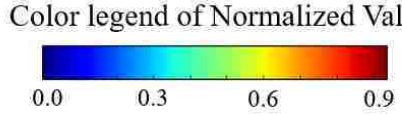

Figure 7.4 Trajectory accuracy mapping results

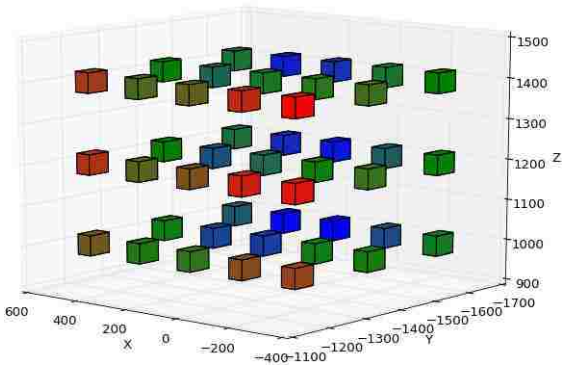

(g) Trajectory rotate angle equals 180°

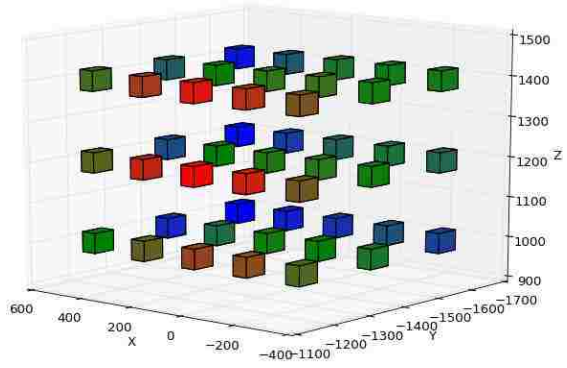

(h) Trajectory rotate angle equals 210°

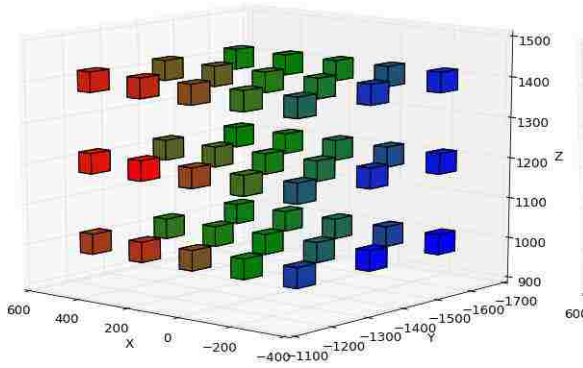

(i) Trajectory rotate angle equals 240°

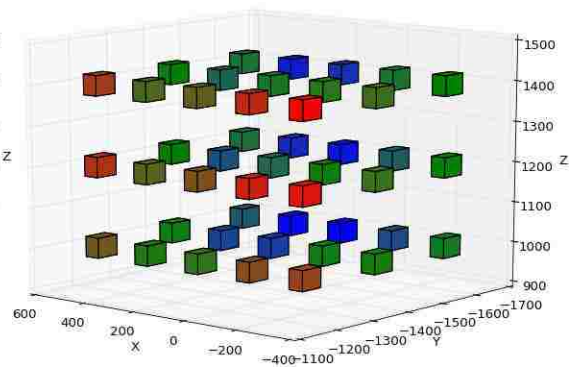

(j) Trajectory rotate angle equals 270°

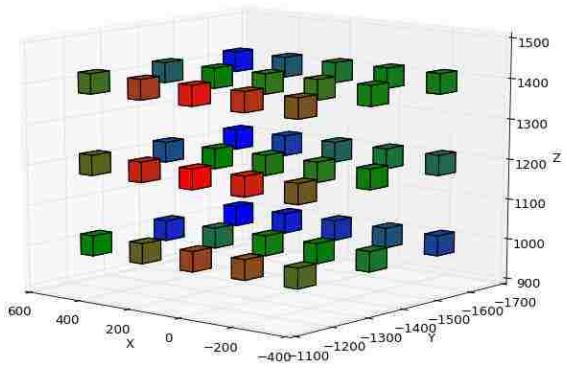

(k) Trajectory rotate angle equals 300°

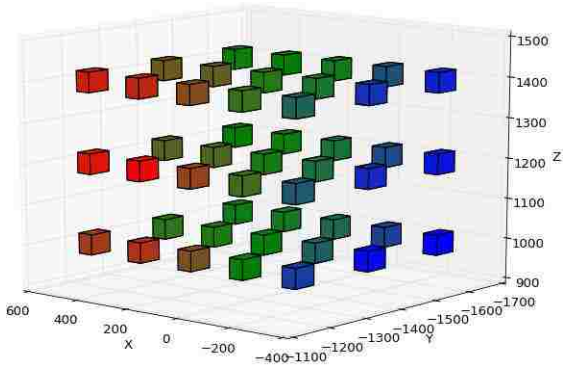

(l) Trajectory rotate angle equals 330°

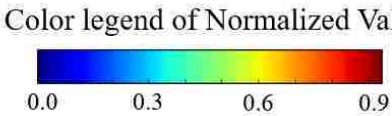

Figure 7.4 Trajectory accuracy mapping results (cont.)

As can be seen from Table 7.1 and Figure 7.4, the affection of position to the trajectory accuracy evaluation result is obvious. The accuracy evaluation result is also changing with the change of trajectory's orientation. Because the deposition angle between layers differs 90°, so the trajectory accuracy evaluation value in each axis directions is close, but it is still slightly different. The lower of the evaluation result is, the better accuracy can be obtained. Thus, the best position and orientation to perform this zigzag task is at center point of [100, -1600, 1000], and orientation angle is 90°.

For the laser metal deposition process, track width is an important parameter to ensure the deposition quality, it will affect the gap distance between the melting pools, thereby influence the dimension accuracy and density of the deposited parts (Figure 7.5).

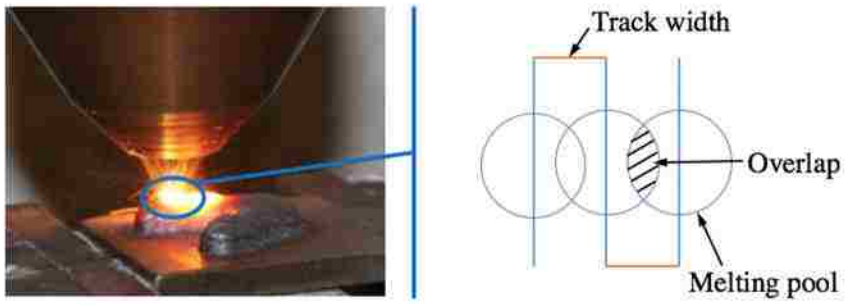

Figure 7.5 Schematic diagram of track width and melting in laser metal deposition

Usually, the diameter of laser spot is 2 mm, the overlap is chosen as 30%, thereby the theoretical track width should be 1.4 mm. But in actual, due the motion error of moving system, a 10% tolerance of the theoretical value is acceptable, as shown in Figure 7.6.

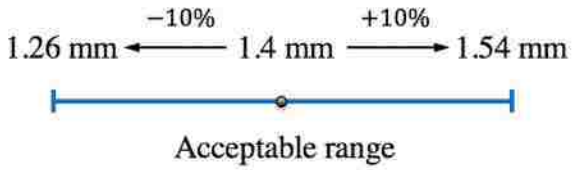

Figure 7.6 Deposition track width tolerance

With a group of known joint error value, the actual track width conduct by robot at the best position and orientation can be calculated through the robot kinematic. The joint error can be obtained by using many kinds of robot calibration method, like the laser tracker or machine vision. In order to discuss the affection of joint error on actual deposition track width, the joint error can be assumed with consideration of the robot's structure, wearing state, and its working environment. Three groups of joint error have been assumed as following: Joint error_1 [0.011, -0.26, 0.05, -0.01, -0.04, -0.01], Joint error_2 [0.023, 0.05, -0.29, 0.38, -0.03, 0.01], Joint error_3 [-0.013, 0.17, -0.09, 0.15, 0.04, 0.01].

There are total of 60 track width segments in the deposition working path, the actual track width according to these three groups of joint error has been plotted as shown in Figure 7.7:

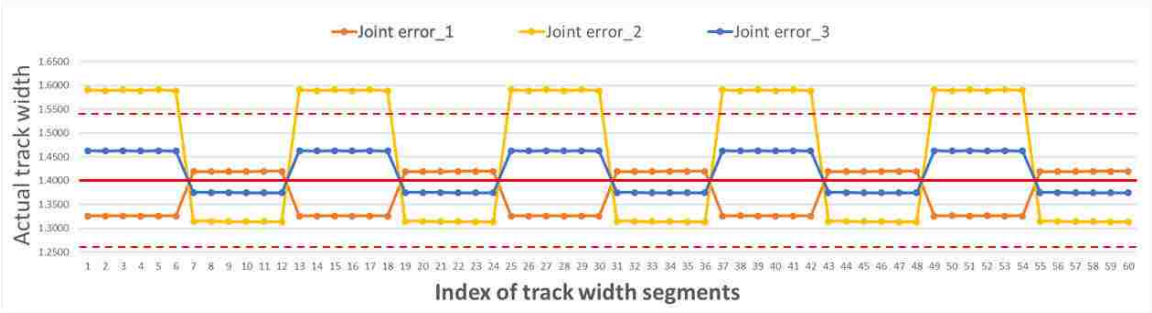

Figure 7.7 Actual track width according to different joint error

The red solid line is the theoretical value of track width, the two red dash lines are the lower and upper tolerance of this theoretical value. As can be seen from Figure 7.7, Joint error_2 exceed the upper tolerance, that means if robot's joints with this group of joint error value, it cannot satisfy the requirements of laser deposition task. In this case, the robot system is needed to be calibrated or applied with other compensation methods to improve its movement and position accuracy performance. For the other two groups of joint error, all of the track width value can fall into the acceptable tolerance range, but the

distribution of deviation from the theoretical value is different. Joint error_3 could result lager actual track width values than Joint error_1, it is preferred for the actual additive process, because this provides more manufacturing allowance for the next step machining process in hybrid manufacturing.

8. CONCLUSION

The subject of this paper was to develop a new methodology for finding the best position and orientation to perform a specific tasks based on the current robot system accuracy capability. Firstly, knowledge of rigid body representation and homogeneous transformation matrices was introduced. Then the D-H model of Nachi Robot (SC300F-02) was established and the detail solution of robot forward/inverse kinematic was given. Since joint angle error affects the end effector position accuracy greatly, a robot positon error model was created to analyze the sensitivity of each joint with angle error. It reveals that even the same joint angle error could have different weight of affection when it appears on different joint. Thus, a new evaluation formulation was established for mapping the trajectory accuracy within the robot's working volumetric. With a group of known joint error, influence of different position and orientation on the movement accuracy of end effector was discussed. Finally, the simulation process takes a laser deposition zigzag working path as example to validate effectiveness of the proposed methodology, it also can be used as a criterion for checking the current joint error of robot system whether or not can satisfy a specific manufacturing tolerance. In addition, this method not only benefits the application of using robot in hybrid manufacturing process, it also important for improving robot operation accuracy performance in other area and optimizing the cost design of the industrial robot.

ACKNOWLEDGEMENTS

This research was supported by Laser Aided Manufacturing Processes (LAMP) Laboratory at Missouri University of Science and Technology (Missouri S&T). Their support is greatly appreciated. The author would like to thank Lei Yan and Xueyang Chen from the Department of Mechanical & Aerospace Engineering at Missouri S&T for their valuable contribution to the project. The author would also like to thank all the people attached directly or indirectly to the project.

REFERENCES

[1] Summers, Mark. "Robot capability test and development of industrial robot positioning system for the aerospace industry." SAE transactions 114.1 (2005): 1108-1118.

[2] Mooring, Benjamin W., Morris R. Driels, and Zvi S. Roth. "Fundamentals of manipulator calibration." (1991).

[3] Veitschegger, William K., and Chi-Haur Wu. "Robot accuracy analysis based on kinematics." Robotics and Automation, IEEE Journal of 2.3 (1986): 171-179.

[4] Roth, Z. V. I. S., B. Mooring, and Bahram Ravani. "An overview of robot calibration." IEEE Journal on Robotics and Automation 5.3 (1987): 377-385.

[5] Hayati, Samad, Kam Tso, and Gerald Roston. "Robot geometry calibration." Robotics and Automation, 1988. Proceedings., 1988 IEEE International Conference on. IEEE, 1988.

[6] Zak, G., et al. "Application of the weighted least squares parameter estimation method to the robot calibration." Journal of Mechanical Design 116.3 (1994): 890-893.

[7] Schröer, Klaus, Stephen L. Albright, and Michael Grethlein. "Complete, minimal and model-continuous kinematic models for robot calibration." Robotics and Computer-Integrated Manufacturing 13.1 (1997): 73-85.

[8] Elatta, A. Y., et al. "An overview of robot calibration." Information Technology Journal 3.1 (2004): 74-78.

[9] Judd, Robert P., and Al B. Knasinski. "A technique to calibrate industrial robots with experimental verification." Robotics and Automation, IEEE Transactions on 6.1 (1990): 20-30.

[10] Duelen, G., and K. Schröer. "Robot calibration—method and results." Robotics and Computer-Integrated Manufacturing 8.4 (1991): 223-231.

[11] Hudgens, Jeff, Daniel Cox, and Delbert Tesar. "Classification structure and compliance modeling for serial manipulators." Robotics and Automation, 2000. Proceedings. ICRA'00. IEEE International Conference on. Vol. 4. IEEE, 2000.

[12] Hsia, Tien C. System identification: least-squares methods. Vol. 1. Lexington: Lexington books, 1977.

[13] Omodei, Alberto, Giovanni Legnani, and Riccardo Adamini. "Three methodologies for the calibration of industrial manipulators: Experimental results on a SCARA robot." Journal of Robotic Systems 17.6 (2000): 291-307.

[14] Press, William H., et al. "Numerical Recipes in C: The Art of Scientific Computing (New York." Cambridge University Press (1992): 636-9.

[15] Fassi, Irene, et al. "Calibration of serial manipulators: theory and applications." Industrial Robotics: Programming, Simulation and Applications (2007): 147-170.

[16] Park, In-Won, and Jong-Hwan Kim. "Estimating entire geometric parameter errors of manipulator arm using laser module and stationary camera." IECON 2011-37th Annual Conference on IEEE Industrial Electronics Society. IEEE, 2011.

[17] Renders, Jean-Michel, et al. "Kinematic calibration and geometrical parameter identification for robots." Robotics and Automation, IEEE Transactions on 7.6 (1991): 721-732.

[18] Gatla, Chandra Sekhar, et al. "An automated method to calibrate industrial robots using a virtual closed kinematic chain." Robotics, IEEE Transactions on 23.6 (2007): 1105-1116.

[19] Stone, Henry W., Arthur C. Sanderson, and Charles P. Neuman. "Arm signature identification." Robotics and Automation. Proceedings. 1986 IEEE International Conference on. Vol. 3. IEEE, 1986.

[20] Stone, Henry W., and Arthur C. Sanderson. "A prototype arm signature identification system." Robotics and Automation. Proceedings. 1987 IEEE International Conference on. Vol. 4. IEEE, 1987.

[21] Abderrahim, M., and A. R. Whittaker. "Kinematic model identification of industrial manipulators." Robotics and Computer-Integrated Manufacturing 16.1 (2000): 1-8.

[22] Dolinsky, Jens-Uwe, I. D. Jenkinson, and G. J. Colquhoun. "Application of genetic programming to the calibration of industrial robots." Computers in Industry 58.3 (2007): 255-264.

[23] Jang, Joon Hyun, Soo Hyun Kim, and Yoon Keun Kwak. "Calibration of geometric and non-geometric errors of an industrial robot." Robotica 19.03 (2001): 311-321.

[24] Bai, Ying. "On the comparison of model-based and modeless robotic calibration based on a fuzzy interpolation method." The International Journal of Advanced Manufacturing Technology 31.11-12 (2007): 1243-1250.

[25] Aoyagi, Seiji, et al. "Improvement of robot accuracy by calibrating kinematic model using a laser tracking system-compensation of non-geometric errors using neural networks and selection of optimal measuring points using genetic algorithm." Intelligent Robots and Systems (IROS), 2010 IEEE/RSJ International Conference on. IEEE, 2010.

[26] Wang, Dali, Ying Bai, and Jiying Zhao. "Robot manipulator calibration using neural network and a camera-based measurement system." Transactions of the Institute of Measurement and Control (2010).

[27] Alici, Gürsel, and Bijan Shirinzadeh. "A systematic technique to estimate positioning errors for robot accuracy improvement using laser interferometry based sensing." Mechanism and Machine Theory 40.8 (2005): 879-906.

[28] Alıcı, Gürsel, et al. "Prediction of geometric errors of robot manipulators with Particle Swarm Optimisation method." Robotics and Autonomous Systems 54.12 (2006): 956-966.

[29] Takanashi, Nobuaki. "6 DOF manipulators absolute positioning accuracy improvement using a neural-network." Intelligent Robots and Systems' 90.'Towards a New Frontier of Applications', Proceedings. IROS'90. IEEE International Workshop on. IEEE, 1990.

[30] Zhong, Xiaolin, John Lewis, and Francis L. N-Nagy. "Inverse robot calibration using artificial neural networks." Engineering Applications of Artificial Intelligence 9.1 (1996): 83-93.

II. INDUSTRIAL ROBOT TRAJECTORY STIFFNESS MAPPING FOR HYBRID MANUFACTURING

Zhiyuan Wang, Renwei Liu, Todd Sparks and Frank Liou

Department of Mechanical and Aerospace Engineering

Missouri University of Science and Technology, Rolla, Missouri 65409, U.S.A.

ABSTRACT

The application of using industrial robots in hybrid manufacturing is promising, but the heavy external load applied on robot system, including the weight of deposition extruder or the cutting force from machining process, affects the operation accuracy significantly. This paper proposed a new method for helping robot to find the best position and orientation to perform heavy duty tasks based on the current system stiffness. By analyzing the robot kinematic and stiffness matrix properties of robot, a new evaluation formulation has been established for mapping the trajectory's stiffness within the robot's working volumetric. The influence of different position and orientation for hybrid manufacturing working path in different scale has been discussed. Finally, a visualized evaluation map can be obtained to describe the stiffness difference of a robotic deposition working path at different positions and orientations. The method is important for improving the operation performance of robot system with current stiffness capability.

Keywords: Industrial Robot, Robot Stiffness, Jacobian Matrix, Hybrid Manufacturing

1. INTRODUCTION

Serial industrial robots are mainly used in industry for tasks that require good repeatability but not necessarily good global position and orientation accuracy of the robot end effector. For example, these robots are generally used for pick and place, painting and welding operations. These kind of tasks do not apply much external load or force on the robot system, the stiffness of robot system itself is sufficient to satisfy these operations' accuracy requirements. With the development of automation technology, the scope of applications using industrial robots is getting wider and wider. The potential applications of industrial robots in hybrid manufacturing, which usually involve both robot deposition process and robot machining process, have been gaining worldwide attention from researchers. But the external load from hybrid manufacturing process applied on robot system, including the weight of fused pellets extruder for deposition process and the cutting force from metal machining process, is much larger than common tasks for robot. Thus, to perform these operations, the robots must show good kinematic and elastostatic performance.

Some research works discuss the following: (i) tool path optimization considering both kinematic and dynamic robot performance [1–2]; (ii) the determination of optimal cutting parameters to avoid tool chattering [3,4]; (iii) robot stiffness analysis [5]; and (iv) the determination of robot performance indices [6–10]. Robot stiffness is also a relevant performance index for robot machining [11]. Accordingly, this paper discusses the stiffness modeling of serial robots and identifies their stiffness parameters. Some stiffness models can be found in the literature for serial and parallel manipulators [12-13]; however, the identification of stiffness parameters has yet to be determined. Two methods were

presented by Abele et al. [14] to obtain the Cartesian stiffness matrix (CaSM) of a five-revolute robot. The first method consists of clamping all of the joints except one to measure its stiffness. The second method measures the displacements of the robot end-effector due to certain applied loads and evaluates the robot Cartesian stiffness matrix throughout its Cartesian workspace with some interpolations.

In addition to the study of dynamic stiffness (which is useful for vibration and stability problems), the study of robot rigidity can be performed through the analysis of static stiffness maps. Static stiffness maps can be used to assess the level of positioning error for a given production task, i.e., for a given type of loading condition [15-17]. They can also be used to compare different architectures or configurations [18-19]. A few studies in the literature provide the stiffness maps of industrial robots. Using the virtual joint method, Gosselin [20] provided stiffness maps with the aim of setting a tool for the computer-aided design of a planar 3-DOF parallel manipulator and a spatial 6-DOF parallel manipulator. Majou et al. [21] identified the stiffest areas in the workspace of the Orthoglide, which is a three-axis translational parallel kinematic machine, by analyzing its stiffness maps for a specific machining task. Ruggiu [22] mapped the stiffness of a translational parallel mechanism using a general formulation based on the development of the principle of virtual work. Pinto et al. [23] used MSA, finite element method (FEM), and experimental measurements for the stiffness mapping of a Daedalus I, and concluded that volume FEM was more precise but leads to long calculation times.

The research objects of the above studies focus on robot stiffness parameter identification or stiffness distribution in robot working volume. This paper provides a new concept of viewing robot stiffness mapping problem, this method takes the turning points

of working path into consideration, by analyzing robot kinematic and the property of robot cartesian stiffness matrix, establish an evaluation formualtion to describe the difference of trajectory stiffness at different position and orientation. The paper will first introduce the mathematics foundation of robot jacobian matrix and how solve the jacobian matrix for a 6 DOF industrial robot, then based on two reasonable assumptions establish the stiffness model of serial manipulator and trajectory stiffness evaluation formualtion, finally apply the proposed method on a specific typical zigzag working path, find out the best position and orientation to perform this in the robot working volume and discuss how the size of working path affect the stiffness mapping analysis.

2. KINEMATIC JACOBIAN OF ROBOT

The Jacobian matrix is the matrix of all first-order partial derivatives of a vector-valued function. Suppose there are following multivariate functions:

$$\begin{aligned} y_1 &= f_1(x_1, x_2, x_3, x_4, x_5, x_6) \\ y_2 &= f_2(x_1, x_2, x_3, x_4, x_5, x_6) \\ y_3 &= f_3(x_1, x_2, x_3, x_4, x_5, x_6) \\ y_4 &= f_4(x_1, x_2, x_3, x_4, x_5, x_6) \\ y_5 &= f_5(x_1, x_2, x_3, x_4, x_5, x_6) \\ y_6 &= f_6(x_1, x_2, x_3, x_4, x_5, x_6) \end{aligned} \tag{1}$$

It can be written in vector form as:

$$Y = F(X) \tag{2}$$

Solve the multiple variables' first derivative of functions in equation (1):

$$\begin{aligned} dy_1 &= \frac{\partial f_1}{\partial x_1} dx_1 + \frac{\partial f_1}{\partial x_2} dx_2 \quad + \frac{\partial f_1}{\partial x_6} dx_6 \\ dy_2 &= \frac{\partial f_2}{\partial x_1} dx_1 + \frac{\partial f_2}{\partial x_2} dx_2 \quad + \frac{\partial f_2}{\partial x_6} dx_6 \\ dy_3 &= \frac{\partial f_3}{\partial x_1} dx_1 + \frac{\partial f_3}{\partial x_2} dx_2 \quad + \frac{\partial f_3}{\partial x_6} dx_6 \\ dy_4 &= \frac{\partial f_4}{\partial x_1} dx_1 + \frac{\partial f_4}{\partial x_2} dx_2 \quad + \frac{\partial f_4}{\partial x_6} dx_6 \\ dy_5 &= \frac{\partial f_5}{\partial x_1} dx_1 + \frac{\partial f_5}{\partial x_2} dx_2 \quad + \frac{\partial f_5}{\partial x_6} dx_6 \\ dy_6 &= \frac{\partial f_6}{\partial x_1} dx_1 + \frac{\partial f_6}{\partial x_2} dx_2 \quad + \frac{\partial f_6}{\partial x_6} dx_6 \end{aligned} \tag{3}$$

It can be written in vector form as:

$$dY = \frac{\partial F}{\partial X} dX \tag{4}$$

Make $J = \frac{\partial F}{\partial X}$, thus J is the jacobian matrix to illustrate the mapping relationship between dY and dX:

$$Y = J(X)X \tag{5}$$

Assume the movement function of robot is:

$$\boldsymbol{x} = x(\boldsymbol{q}) \tag{6}$$

$\boldsymbol{x}$ is the vector representing the position and orientation of robot's end effector, $\boldsymbol{q}$ is the vector representing the angle value of each joint. From equation (5), the jacobian matrix of robot $J(q)$ is:

$$x = J(q)q \tag{7}$$

Or it can be written in matrix form as:

$$\begin{matrix} dx \\ dy \\ dz \\ \delta x \\ \delta y \\ \delta z \end{matrix} = \begin{bmatrix} Robot \\ Jacobian \end{bmatrix} \begin{matrix} d\theta_1 \\ d\theta_2 \\ d\theta_3 \\ d\theta_4 \\ d\theta_5 \\ d\theta_6 \end{matrix} \tag{8}$$

3. SOLUTION OF THE JACOBIAN MATRIX OF ROBOT

The Nachi Robot (SC300F-02) is used as an illustrate example throughout this paper. It has a 4.1 m^2 (cross-section area) operating area and a 300° rotation range for the base motor (Figure 3.1), which could provide a much bigger working envelope than any current hybrid manufacturing system. The 6-axis movement mechanism makes the deposition/machining process more flexible in building a model with complex features.

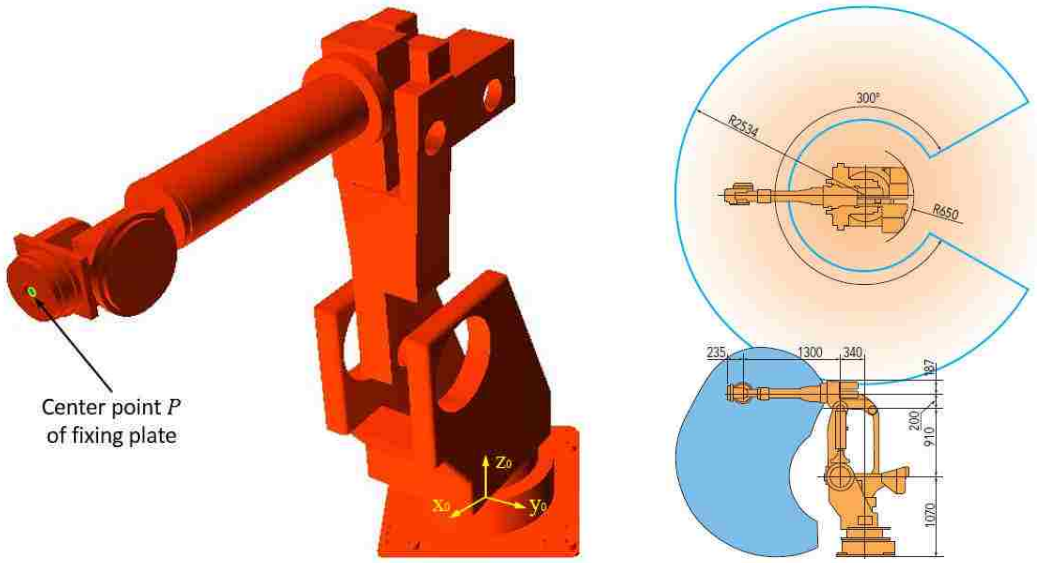

Figure 3.1 Working envelop and links schematic of Nachi Robot (SC300F-02)

The sixth link carrying the operation point P is connected to the base frame through a serial chain composed of six-revolute joints. The kinematic chain of Nachi Robot (SC300F-02) is shown in Figure 3.2.

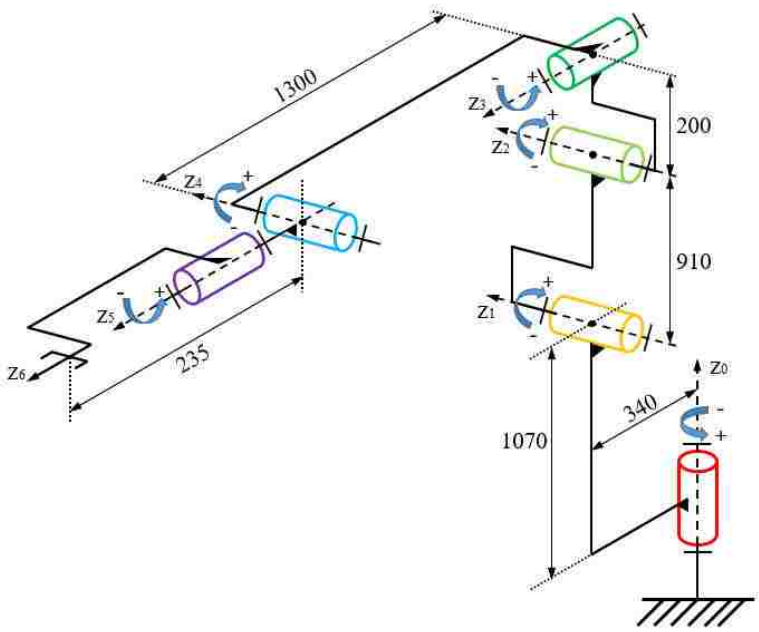

Figure 3.2 Kinematic chain schematic of Nachi Robot (SC300F-02)

But one thing needs to be noticed is that at current posture, the joints value displayed on the robot's touchpad is $[0^\circ \quad 90^\circ \quad 0^\circ \quad 0^\circ \quad 0^\circ \quad 0^\circ]$. In order to build a D-H model could represent the real robot perfectly, all of the joint value should be set to 0°, thus the robot's posture will be look like as the Figure 3.3:

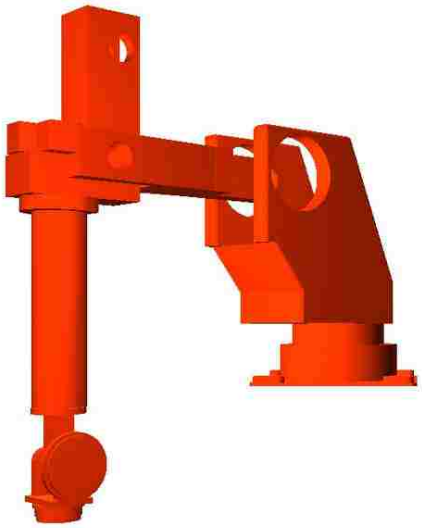

Figure 3.3 Robot's posture when joints value as $[0^\circ \quad 0^\circ \quad 0^\circ \quad 0^\circ \quad 0^\circ \quad 0^\circ]$

Start at joint 1, z_0 represents the first joint, which is the base revolute joint, x_0 is chosen to be the same direction as the reference frame x-axis of the robot controller, this is done for convenience to verify the correctness of the D-H model. x_0 is a fixed field axis, it represents the base of the robot. Next, z_1 is assigned at joint 2. x_1 will be normal to z_0 and z_1, because these two axes are intersecting. x_2 will be in the direction of the common normal between z_1 and z_2. x_3 is in the direction of the common normal between z_2 and z_3. In order to ensure the solvability of the invers kinematic of robot, z_4, z_5 and z_6 are assigned at the same origin point. Thus, the reference frames representation of Nachi robot as shown in Figure 3.4. Normally, the end effector is not included in the equations of motions, but it can be represented by an additional line in the D-H parameters table. In the case, the tip point of end effector physically represents the center point of the fixing plate of the joint 6, it is also as the same as the coordinate value that indicated on the robot's touch pad.

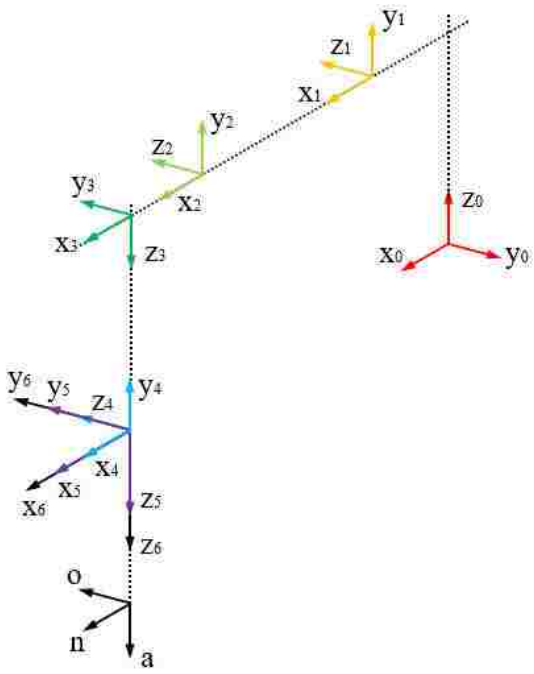

Figure 3.4 Reference frames representation of Nachi robot

According to these assigned coordinate frames, the parameters of D-H model can be filled out in Table 3.1. Notice that the rotations are measured with the right-hand rule. The curled fingers of your right hand, rotating in the direction of rotation, determine the direction of the axis of rotation along the thumb.

Table 3.1 D-H model parameters of Nachi Robot (SC300F-02)

i	θ_i	d_i	a_i	α_i
1	θ_1	1070	340	90
2	θ_2	0	910	0
3	θ_3	0	200	90
4	θ_4	1300	0	-90
5	θ_5	0	0	90
6	θ_6	0	0	0
tool	0	235	0	0

T_n represents the transformation matrix of end effector frame relative to the base frame of a n degree of freedom series robot. The position and orientation of an arbitrary point ${}^{n}p = [p_x \quad p_y \quad p_z]$ on the end effector can be described in the robot base coordinate frame as following:

$$ {}^{0}p = T_n {}^{n}p = A_1 A_2 A_3 \quad A_n {}^{n}p \tag{9} $$

For a robot which structure has been determined, according to D-H model table, link length a_i, link offset d_i, and link rotation angle α_i are all known parameters, θ_i are the variables changing with the movement of the robot. Thus, the equations of forward kinematic can be written as:

$$ T_n = A_1(\theta_1)A_2(\theta_2)A_3(\theta_3) \quad A_n(\theta_n) \tag{10} $$

For the Nachi robot, there are 6 joints, the transformation between each two successive joints can be written by simply substituting the parameters from the Table 1:

$$A_1 = \begin{bmatrix} C_1 & 0 & S_1 & a_1C_1 \\ S_1 & 0 & C_1 & a_1S_1 \\ 0 & 1 & 0 & d_1 \\ 0 & 0 & 0 & 1 \end{bmatrix} \tag{11}$$

$$A_2 = \begin{bmatrix} C_2 & S_2 & 0 & a_2C_2 \\ S_2 & C_2 & 0 & a_2S_2 \\ 0 & 0 & 1 & 0 \\ 0 & 0 & 0 & 1 \end{bmatrix} \tag{12}$$

$$A_3 = \begin{bmatrix} C_3 & 0 & S_3 & a_3C_3 \\ S_3 & 0 & C_3 & a_3S_3 \\ 0 & 1 & 0 & 0 \\ 0 & 0 & 0 & 1 \end{bmatrix} \tag{13}$$

$$A_4 = \begin{bmatrix} C_4 & 0 & S_4 & 0 \\ S_4 & 0 & C_4 & 0 \\ 0 & 1 & 0 & d_4 \\ 0 & 0 & 0 & 1 \end{bmatrix} \tag{14}$$

$$A_5 = \begin{bmatrix} C_5 & 0 & S_5 & 0 \\ S_5 & 0 & C_5 & 0 \\ 0 & 1 & 0 & 0 \\ 0 & 0 & 0 & 1 \end{bmatrix} \tag{15}$$

$$A_6 = \begin{bmatrix} C_6 & S_6 & 0 & 0 \\ S_6 & C_6 & 0 & 0 \\ 0 & 0 & 1 & 0 \\ 0 & 0 & 0 & 1 \end{bmatrix} \tag{16}$$

In the equations, S_i represents $sin(\theta_i)$, C_i represents $cos(\theta_i)$.

$\boldsymbol{T}_6$ is a 4×4 homogeneous matrix, the forward kinematic solution of Nachi Robot it can be written as following:

$$T_6 = \begin{bmatrix} n_x & o_x & a_x & p_x \\ n_y & o_y & a_y & p_y \\ n_z & o_z & a_z & p_z \\ 0 & 0 & 0 & 1 \end{bmatrix} = A_1 A_2 A_3 A_4 A_5 A_6 \quad (17)$$

Or it can be written in a lite form:

$$T_6 = \begin{bmatrix} \bar{n} & \bar{o} & \bar{a} & \bar{p} \\ 0 & 0 & 0 & 1 \end{bmatrix} = A_1 A_2 A_3 A_4 A_5 A_6 \quad (18)$$

Each element in the Jacobian is the derivative of a corresponding kinematic equation with respect to one of the variables. Referring to Equation (8), the first element in x is dx. This means the first kinematic equation must represent movements along the x-axis, which, of course, would be p_x. In other words, p_x expresses the motion of the hand frame along the x-axis, and thus, its derivative will be dx. The same will be true for dy and dz. Considering the $\bar{n}$, $\bar{o}$, $\bar{a}$, $\bar{p}$ matrix, the corresponding elements of p_x, p_y, p_z can be picked and be differentiated to get the dx, dy, and dz. However, since there is no unique equation that describe the rotations about the axes, thus there is no single equation available for differential rotations about the three axes, namely, δx, δy and δz. As a result, these have to be calculated differently.

Actually, it is a lot simpler to calculate the Jacobian relative to T_6, the last frame, than it is to calculate it relative to the first frame. The velocity equation relative to the last frame can be written as:

$$^{T_6}\dot{x} = {}^{T_6}J(q)\dot{q} \quad (19)$$

$^{T_6}\dot{x}$ is the vector representing the position and orientation of robot's end effector in last frame, q is the vector representing the angle value of each joint. This means that for the same joint differential motions, pre-multiplied with the Jacobian matrix relative to the last frame, the operation point differential motions relative to the last frame can be

obtained. One can calculate the Jacobian with respect to the last frame using following formation steps:

(1) The differential motion relationship of equation can be written as:

$$\begin{matrix} {}^{T_6}dx \\ {}^{T_6}dy \\ {}^{T_6}dz \\ {}^{T_6}\delta x \\ {}^{T_6}\delta y \\ {}^{T_6}\delta z \end{matrix} = \begin{matrix} {}^{T_6}J_{11} & {}^{T_6}J_{12} & {}^{T_6}J_{16} \\ {}^{T_6}J_{21} & {}^{T_6}J_{22} & {}^{T_6}J_{26} \\ {}^{T_6}J_{31} & {}^{T_6}J_{32} & {}^{T_6}J_{36} \\ {}^{T_6}J_{41} & {}^{T_6}J_{42} & {}^{T_6}J_{46} \\ {}^{T_6}J_{51} & {}^{T_6}J_{52} & {}^{T_6}J_{56} \\ {}^{T_6}J_{61} & {}^{T_6}J_{62} & {}^{T_6}J_{66} \end{matrix} \begin{matrix} d\theta_1 \\ d\theta_2 \\ d\theta_3 \\ d\theta_4 \\ d\theta_5 \\ d\theta_6 \end{matrix} \tag{20}$$

(2) Assuming that any combination of A_1, A_2, A_n can be expressed with a corresponding $\bar{n}$, $\bar{o}$, $\bar{a}$, $\bar{p}$ matrix, the corresponding elements of the matrix will be used to calculate the Jacobian.

(3) If joint i under consideration is a revolute joint, then:

$$\begin{matrix} {}^{T_6}J_{1i} \\ {}^{T_6}J_{2i} \\ {}^{T_6}J_{3i} \\ {}^{T_6}J_{4i} \\ {}^{T_6}J_{5i} \\ {}^{T_6}J_{6i} \end{matrix} = \begin{matrix} (\ n_x p_y + n_y p_x) \\ (\ o_x p_y + o_y p_x) \\ (\ a_x p_y + a_y p_x) \\ n_z \\ o_z \\ a_z \end{matrix} \tag{21}$$

(4) The column i use ${}^{i-1}T_6$:

For column 1, use ${}^{0}T_6 = A_1 A_2 A_3 A_4 A_5 A_6$

For column 2, use ${}^{1}T_6 = A_2 A_3 A_4 A_5 A_6$

For column 3, use ${}^{2}T_6 = A_3 A_4 A_5 A_6$

For column 4, use ${}^{3}T_6 = A_4 A_5 A_6$

For column 5, use ${}^{4}T_6 = A_5 A_6$

For column 6, use ${}^{5}T_6 = A_6$

4. FORCE JACOBIAN MATRIX OF ROBOT

When an external load applied on the robot end effector, if the robot system is in equilibrium state, the driving force generated by each joint should be balance with the external load. The external load can be written as $F = [f, n]^T$, so called the generalized end effector force vector. Revolute joint provides driving torque, prismatic joint provide drive force. For the Nachi Robot, the driving torques provided by the six revolute joints are τ_1, τ_2, τ_6, these can be written as:

$$\tau = [\tau_1 \quad \tau_2 \quad \tau_3 \quad \tau_4 \quad \tau_5 \quad \tau_6]^T \tag{22}$$

So called the generalized joint force vector.

According to the principle of virtual work, make the virtual displacement of each joint is dq, the virtual displacement of end effector is dX, thus the sum of virtual work by each joint force is:

$$W_q = \tau^T dq = \tau_1 dq_1 + \tau_2 dq_2 \quad + \tau_6 dq_6 \tag{23}$$

$$W_F = F^T dX \tag{24}$$

According to the sum of virtual work should be zero, thus:

$$\tau^T dq = F^T dX \tag{25}$$

From Equation (5), there is:

$$dX = J(q)dq \tag{26}$$

From Equation (26) and (26), there is:

$$\tau^T dq = F^T J(q)dq$$

$$\Rightarrow \quad \tau = J^T(q)F \tag{27}$$

$J^T(q)$ is force Jacobian matrix of robot, when the robot system is in equilibrium state, it represents the mapping relationship between external load and joint force. It is also the transposed matrix of Jacobian matrix.

5. CARTESIAN STIFFNESS MATRIX FORMULATION OF ROBOT SYSTEM

The robot system stiffness refers to the ability of resist to deformation, especially the displacement of end effector, when robot subjected to external robot. Make external load as $F = [f_x \quad f_y \quad f_z \quad n_x \quad n_y \quad n_z]^T$, the tiny displacement of end effector subjected to external load is $dX = [dx \quad dy \quad dz \quad \delta x \quad \delta y \quad \delta z]^T$. When displacement is small enough, there are linear relationship between these two: $F = KdX$. It can be written in matrix form:

$$\begin{matrix} f_x \\ f_y \\ f_z \\ n_x \\ n_y \\ n_z \end{matrix} = \begin{matrix} k_{11} & k_{12} & & k_{16} \\ k_{21} & k_{22} & & k_{26} \\ k_{31} & k_{32} & & k_{36} \\ k_{41} & k_{42} & & k_{46} \\ k_{51} & k_{52} & & k_{56} \\ k_{61} & k_{62} & & k_{66} \end{matrix} \begin{matrix} d\theta_1 \\ d\theta_2 \\ d\theta_3 \\ d\theta_4 \\ d\theta_5 \\ d\theta_6 \end{matrix} \tag{28}$$

F is the external load applied on end effector relative to the base coordinate frame of robot, it contains the force and torque in three degrees of freedom. dX is the displacement of the end effector relative the base coordinate of robot, it contains the translation and rotation in three degrees of freedom. Both of these are 6-dimensinal vectors. K is 6×6 matrix, it is the cartesian stiffness matrix of robot system.

The cartesian stiffness matrix of robot system depends on robot's configuration, link stiffness, control loop stiffness and the actuators' mechanical stiffness. For the slim and long structure, like the repair manipulator applied in space station, the deformation of link is the main factor that affect the robot stiffness. The components of transmission system, like the gears, belt and shaft, will be deformed under driving force. Especially, when the transmission line is long, these deformations could be accumulated and coupling with each other.

Because the deformation and stiffness properties are distributed in the robot system, and the statistical data shows that 70% or higher of deformation is come from the insufficient stiffness of driving and transmission system for the industrial robot. Thus, assume the deformation concentrate on the joints is reasonable. In this paper, the links of robot are assumed to be rigid, the damping is neglected and the stiffness of the joints is represented with the linear torsional springs, the coefficient of elasticity is k_{qi}, so called the joint stiffness, as shown in Figure 5.1. The reciprocal of k_{qi} is c_{qi}, so called the flexibility. For a 6 DOF robot, K_q is the diagonal joint stiffness matrix defined as follows:

$$K_q = \begin{matrix} k_{q1} & 0 & 0 & 0 & 0 & 0 \\ 0 & k_{q2} & 0 & 0 & 0 & 0 \\ 0 & 0 & k_{q3} & 0 & 0 & 0 \\ 0 & 0 & 0 & k_{q4} & 0 & 0 \\ 0 & 0 & 0 & 0 & k_{q5} & 0 \\ 0 & 0 & 0 & 0 & 0 & k_{q6} \end{matrix} \tag{29}$$

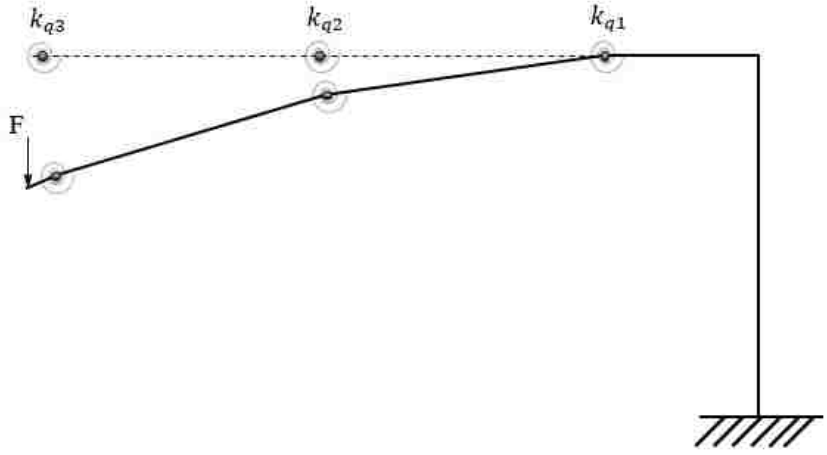

Figure 5.1 A 3-DOF robot model with linear torsional springs as joints

For a n DOF robot, assume the stiffness of each joint is k_{qi} $(i = 1, 2, \quad , n)$, the displacement of end effector is dX which subject to the external load F, the angle changing of each joint is d_{qi} $(i = 1, 2, \quad , n)$, there is:

$$\tau_i = k_{qi} d_{qi} \ (i = 1, 2, \quad , n) \tag{30}$$

τ_i is torque on each joint, it is due to the elastic deformation of the robot system.

This can be written in matrix form as:

$$\tau = K_q d_q \tag{31}$$

In the above equation, $d_q = [d_{q1} \quad d_{q1} \qquad d_{qn}]^T$, $K_q = diga(k_{q1}, k_{q2}, \quad , k_{qn})$.

Make the robot system stiffness equivalent to each joint, the mapping relationship between joints stiffness and end effector stiffness can be established, the derivation process as following:

From the jacobian matrix of robot, there is:

$$dX = J(q)dq \tag{32}$$

From the force jacobian matrix of robot, there is:

$$\tau = J^T(q)F \tag{33}$$

From equation (31) and equation (33), there is:

$$K_q d_q = J^T(q)F$$

$$\Rightarrow \qquad d_q = {K_q}^{-1} J^T(q)F \tag{34}$$

From equation (32) and equation (34), there is:

$$dX = J(q){K_q}^{-1} J^T(q)F \tag{35}$$

Make $C(q) = J(q){K_q}^{-1} J^T(q)$, thus:

$$dX = C(q)F \tag{36}$$

$C(q)$ is flexibility matrix of end effector.

Equation (35) pre-multiplied by $J^{-1}(q)$, K_q and $J^{-T}(q)$ Successively

$$\Rightarrow \quad J^{-1}(q)dX = J^{-1}(q)J(q){K_q}^{-1}J^T(q)F$$

$$\Rightarrow \quad J^{-1}(q)dX = {K_q}^{-1}J^T(q)F$$

$$\Rightarrow \quad K_q\, J^{-1}(q)dX = K_q{K_q}^{-1}J^T(q)F$$

$$\Rightarrow \quad K_q\, J^{-1}(q)dX = J^T(q)F$$

$$\Rightarrow \quad J^{-T}(q)K_qJ^{-1}(q)dX = J^{-T}(q)J^T(q)F$$

$$\Rightarrow \quad J^{-T}(q)K_qJ^{-1}(q)dX = J^{-T}(q)J^T(q)F$$

$$\Rightarrow \quad J^{-T}(q)K_qJ^{-1}(q)dX = F$$

Make

$$K(q) = J^{-T}(q)\, K_qJ^{-1}(q) \tag{37}$$

Thus:
$$F = K(q)dX \tag{38}$$

$K(q) = J^{-T}(q)\, K_qJ^{-1}(q)$ is the end effector stiffness matrix, derivation is completed.

The stiffness matrix $K(q)$ or flexibility matrix $C(q)$ represents the linear relationship between the external load applied on end effector and the displacement of end effector, and these matrixes change with the changing of robot's position and orientation. As can be seen from the elements in stiffness matrix, the force of one direction not only cause the deformation on this direction, but also cause the deformation in other directions. For example, the diagonal element k_{22} in stiffness matrix represents the f_{y} caused by d_{y} on y direction, the non-diagonal element k_{62} in stiffness matrix represents the n_{z} caused by d_{y} on z direction.

6. ROBOT TRAJECTORY STIFFNESS EVALUATION FORMULATION

The zigzag path is a typical trajectory for robotic hybrid manufacturing as shown in Figure 6.1. One layer of this kind path could work for machining or milling process, multiple layers of that could be used as a deposition working path. When robot carry the deposition extruder or machining tools moving along the straight line segments, the operation speed usually is set at a constant value, the robot system is in equilibrium state. But when the robot moves to the turning points in the trajectory, the end effector often accompanied with intensely changing of acceleration in different directions. The initial cutting force or inertia of heavy deposition equipment in directions of acceleration changing will cause unbalanced force on the robot system, so the robot demands higher stiffness property at these turning points positions.

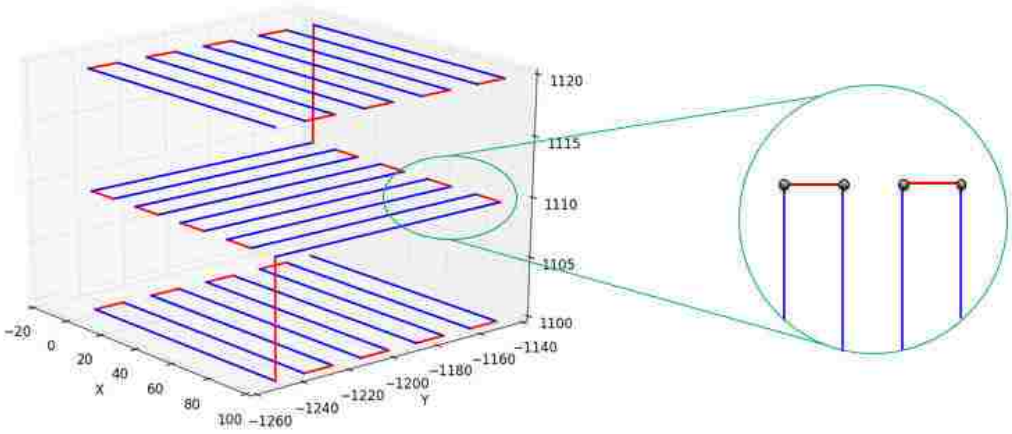

Figure 6.1 Zigzag path for hybrid manufacturing and turning points in the trajectory

As mentioned in the previous section, the robot joint stiffness matrix K_q is a diagonal matrix, so $K_q = {K_q}^T$, simultaneous this with equation (37), there is:

$$K(q) = K(q)^T \tag{39}$$

This is the symmetry property of $K(q)$, which is $k_{ij} = k_{ji}$, it illustrates that if the force in j direction can cause a unit deformation in i direction, then the same force in i direction can cause a unit deformation in j direction. The non-diagonal elements in $K(q)$ represents the coupling relationship between the force and displacement in different direction. When the non-diagonal element equal 0, which means there is no coupling relationship between these two directions. For example, when there is no coupling relationship between the force and displacement in x and y direction, then there is $k_{12} = k_{21} = 0$.

In addition, $K(q)$ is a positive-definite matrix, simultaneous with it symmetry property, the diagonal elements and the principal minor determinant of each order are more than 0, this can be written as:

$$k_{\mathrm{ii}} > 0, \det\left(\begin{bmatrix} k_{11} & k_{1\mathrm{i}} \\ k_{\mathrm{i}1} & k_{\mathrm{ii}} \end{bmatrix}\right) > 0, i = 1, 2, \quad , 6 \tag{40}$$

According to the analysis of $K(q)$'s properties, and notice that the stiffness matrix is changing when robot at different position and orientation, an evaluation formulation can be created to illustrate the difference of trajectory's stiffness performance at different position and orientation within robot working envelop:

$$E = \sum_{i=1}^{6} k_{ii} + \sum_{i=1, j=1, i\neq j}^{6} |k_{ij}| \tag{41}$$

7. SIMULATION: STIFFNESS MAPPING OF A ROBOTIC HYBRID MANUFACTURING WORKING PATH

The initial motivation of applying robot in hybrid manufacturing is overcome the building size limitation of conventional CNC machines. Figure 7.1 shows a schematic of the fused pellets deposition (FPM) extruder installed on the Nachi robot, this equipment can realize deposit large scale part in a relatively short period.

But the weight of the FPM extruder is over 500lb, this is an external load cannot be ignored during operation. Thus it is necessary use trajectory stiffness evaluation method to help planning the working path.

Figure 7.1 Assembly model of FPM system

For conducting a specific working path, there are multiple choices of position and orientation in the robot working envelop. Based on the robot kinematic and stiffness evaluation formulation, a trajectory stiffness evaluation simulation system can be programmed with Python, the flow chart of this simulation analysis system as shown in Figure 7.2.

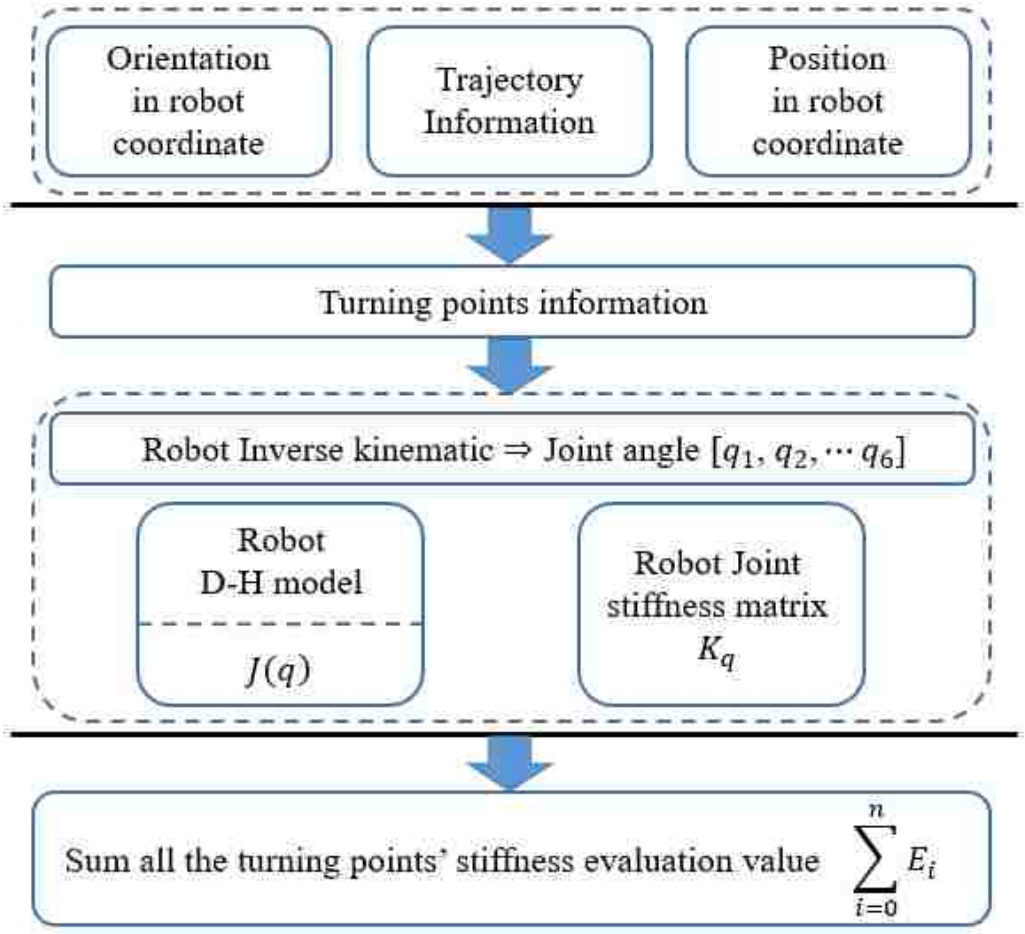

Figure 7.2 Flow chart of trajectory stiffness evaluation simulation system

In order to study how zigzag trajectory's position and orientation affect its stiffness in the working envelop of robot, firstly separate working volume into small testing cube area ($200\text{mm} \times 200\text{mm} \times 200\text{mm}$) within the x range is from -500 to 500, y range is from -1200 to -1800, z range is from 800 to 1400, in robot system coordinate.

The dimension of deposition zigzag path is $100\text{mm} \times 100\text{mm} \times 30\text{mm}$, layer thickness is 10 mm, track width is 20 mm and overlap is 0.3.

Thus there are 45 testing cube areas within robot working envelop, as shown in Figure 7.3.

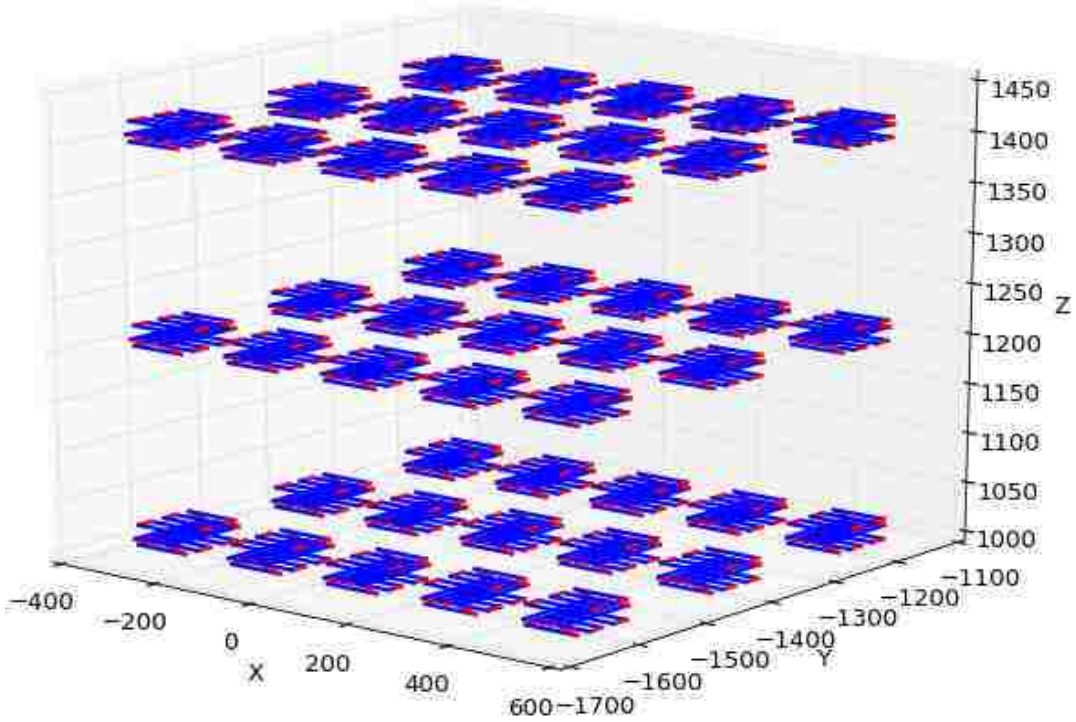

Figure 7.3 Trajectory testing cube within robot working envelop

Secondly, set the orientation angle for these trajectories, start from x axis positive direction, rotate about z axis counterclockwise, take the angle value as 0°, 60°, 120°, 180°, 240°, 300°, respectively.

Then apply the trajectory stiffness analysis process to these zigzag trajectories which at different positions and with different orientations, the results are shown in Table 7.1.

Table 7.1 100mm × 100mm × 30mm trajectory stiffness evaluation value

Trajectory	Rotation angle (°)											
position	0		60		120		180		240		300	
index	Value	Rank	Value	Rank	Value	Rank	Value	Rank	Value	Rank	Value	Rank
1	57912008.5	16	57917201.5	16	58023086.2	16	58098883.1	16	57982785.1	16	57899655.5	16
2	62189826.6	25	62177482.3	25	62238753.2	25	62319313.1	25	62268150.5	25	62198579.2	25
3	63186832.3	27	63162031.7	27	63192306.8	27	63266532.9	27	63256148.0	27	63205920.5	27
4	53285991.7	4	53299057.5	4	53384377.6	4	53404272.6	4	53305523.2	4	53271486.8	4
5	57421016.3	15	57417061.0	15	57472652.6	15	57516140.2	15	57461913.1	15	57421446.2	15
6	59000277.0	19	58983756.3	19	59015254.4	19	59065204.6	19	59044628.4	19	59010565.4	19
7	51508067.0	1	51522248.2	1	51579577.2	1	51567781.9	1	51500388.5	1	51497801.0	1
8	54659692.6	9	54659664.5	9	54702410.9	9	54719810.0	9	54675017.5	9	54657182.4	9
9	56152074.0	12	56140577.0	12	56167441.0	12	56197837.4	12	56176134.9	12	56156830.7	12
10	51419211.9	0	51430333.4	0	51460867.5	0	51436841.7	0	51400559.1	0	51413793.8	0
11	53368017.0	5	53368650.2	5	53396299.6	5	53398184.2	5	53367248.3	5	53364656.5	5
12	54440081.0	8	54430997.9	8	54450115.7	8	54466352.4	8	54448439.6	8	54441096.0	8
13	52164260.4	2	52170766.7	2	52180043.9	2	52155719.1	2	52142697.5	2	52161140.1	2
14	53076982.5	3	53076309.6	3	53089746.1	3	53083921.4	3	53065778.1	3	53072425.1	3
15	53645742.1	6	53637095.4	6	53647414.2	6	53654094.2	6	53641445.7	6	53643383.3	6
16	73443909.7	36	73420000.6	36	73535555.1	36	73692566.6	36	73596953.9	36	73460405.2	36
17	75636443.9	38	75604032.5	38	75668940.1	38	75801094.8	38	75778766.6	38	75677509.0	38
18	74860829.0	37	74820718.6	37	74855339.6	37	74966442.1	37	74978485.2	37	74906726.1	37
19	64402023.5	30	64396711.1	30	64503089.4	30	64581091.8	30	64482815.3	30	64408016.5	30
20	67652769.3	32	67635441.2	32	67700507.0	32	67786708.7	32	67746833.8	32	67676755.0	32
21	68235388.9	33	68208558.4	33	68247052.8	33	68328566.8	33	68321784.0	33	68266431.5	33
22	59097087.6	20	59103493.5	20	59183625.6	20	59213191.8	20	59140921.2	20	59104406.8	20
23	62120889.2	24	62113648.6	24	62169417.0	24	62221092.2	24	62181115.1	24	62136012.4	24
24	63232961.1	28	63215517.6	28	63251622.0	28	63308565.0	28	63293570.5	28	63253606.0	28
25	56080975.2	10	56091933.9	10	56144625.0	10	56153200.0	10	56108066.5	10	56088833.8	10
26	58451823.2	17	58450434.4	17	58493031.0	17	58522436.0	17	58489623.2	17	58461390.3	17
27	59627644.9	21	59616398.3	21	59646464.4	21	59684707.5	21	59667856.7	21	59640602.8	21
28	54333450.4	7	54344378.4	7	54376489.0	7	54378560.4	7	54350578.5	7	54338064.0	7
29	56118242.9	11	56119624.4	11	56149451.5	11	56165633.1	11	56140196.4	11	56122657.9	11
30	57175331.2	14	57167859.3	14	57190380.5	14	57215016.1	14	57199026.8	14	57181766.9	14
31	88574068.5	44	88529787.1	44	88619540.6	44	88828436.1	44	88813640.6	44	88646634.4	44
32	87420580.4	43	87375345.4	43	87435825.8	43	87596780.7	43	87616362.0	43	87499901.4	43
33	84942871.8	42	84893153.4	42	84932478.4	42	85066465.9	42	85099371.8	42	85014684.8	42
34	75849792.0	39	75826520.5	39	75925689.9	39	76065664.0	39	76009206.7	39	75890040.7	39
35	77035187.2	41	77008058.1	41	77072891.5	41	77193342.4	41	77182329.7	41	77088091.5	41
36	76425986.6	40	76392257.0	40	76435917.5	40	76541272.0	40	76550420.2	40	76478337.4	40
37	66838747.2	31	66833073.6	31	66922348.9	31	67005968.4	31	66945252.7	31	66866016.8	31
38	69042978.1	34	69029348.6	34	69091190.3	34	69176008.0	34	69150092.0	34	69078205.8	34
39	69575120.6	35	69553403.0	35	69596732.2	35	69676568.7	35	69670665.6	35	69612149.6	35
40	60648881.9	23	60654519.9	23	60725155.0	23	60774268.8	23	60722885.2	23	60667777.9	23
41	63113367.5	26	63109194.0	26	63163058.5	26	63220357.6	26	63189754.8	26	63136220.4	26
42	64250581.8	29	64237617.3	29	64277140.7	29	64335566.5	29	64321325.6	29	64275581.9	29
43	56424502.0	13	56435653.5	13	56489190.8	13	56518331.5	13	56475400.1	13	56435091.1	13
44	58856879.1	18	58858784.4	18	58902798.7	18	58940188.8	18	58909419.9	18	58869947.2	18
45	60270174.0	22	60263350.3	22	60296984.2	22	60338155.3	22	60319812.4	22	60285295.1	22

As can be seen from Table 7.1, for the same angle group, the position affects the trajectory stiffness obviously. But for the same position with different angle, the evaluation

result is close, take the maximum value position 31 as example, the difference between max and min is only 0.37 %. Moreover, the rank of evaluation result in different angle group is the same. This leads to the stiffness trajectory mapping result is the identical for these 6 groups, as shown in Figure 7.4. The color of cube is assigned as the normalized evaluation values. The higher of the evaluation result is, the better stiffness can be obtained at this position. So the best position to perform this task is at the center point of [500, -1200, 1000].

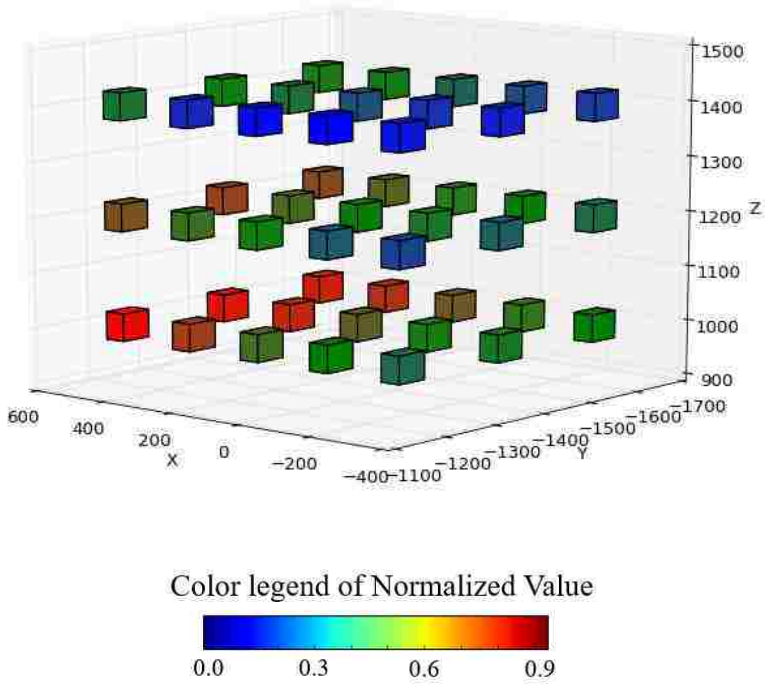

Figure 7.4 Trajectory stiffness mapping results for small scale working path

The reason of this result is the size of the deposition part. The stiffness property of robot is distributed unevenly within its working envelop, the larger of the task's operation range, the more different stiffness area the robot will cross. For the small scale working path, in macro view, most turning points are concentrated within a small area, even with the changing of working path's orientation, the gesture of robot manipulator did not change a lot. Thereby, it is more meaningful to discuss how the orientation affect a large scale

working path's stiffness performance, this is also the initial goal of applying robot in hybrid manufacturing.

Take a large size deposition task as example, the dimension of deposition zigzag path is $800\text{mm} \times 800\text{mm} \times 500\text{mm}$, layer thickness is 10 mm, track width is 20 mm and overlap is 0.3, thus there is only one center point option for this trajectory: [0, -1600, 800]. Then set the orientation angle for these trajectories, start from x axis positive direction, rotate about z axis counterclockwise, take the angle value as 0°, 60°, 120°, 180°, 240°, 300°, respectively. The stiffness evaluation result for this task is shown in Figure 7.5. The difference between maximum value and minimum value is 14 %, much more obvious than the small size working path. The higher of the evaluation result is, the better stiffness can be obtained at this orientation. So the best orientation to perform this task is 60°.

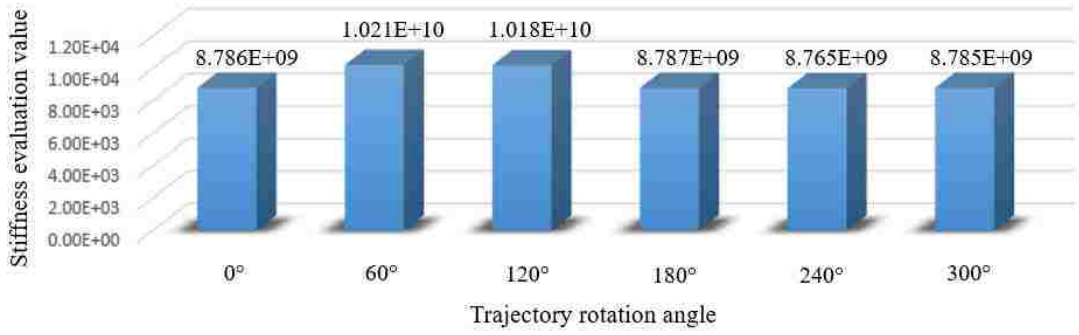

Figure 7.5 Trajectory stiffness mapping results for large scale working path

8. CONCLUSION

The subject of this paper was to develop a new methodology for finding the best position and orientation to perform heavy duty tasks based on the current robot system stiffness capability. Firstly, the definition of jacobian matrix was introduced, and the Nachi Robot (SC300F-02) was used as an illustrate example throughout this paper. The detail process of solving robot jacobian matrix was presented, and the force jacobian matrix also has been derived according to the concept of virtual work. Based the on the assumptions of the link of industrial robot is rigid and all the deformation are concentrated at joints, the stiffness model of serial manipulator was developed. Then the robot stiffness matrix was derived from the robot jacobian matrix and robot joint stiffness matrix. By analyzing the robot kinematic and the properties of robot stiffness matrix, a new evaluation formulation has been established for mapping the trajectory's stiffness within the robot's working volumetric. A trajectory stiffness simulation analysis system was developed for discussing the stiffness difference of a robotic deposition working path at different positions and orientations. The simulation results revealed that for the small size working path, in macro view, most turning points are concentrated within a small area, position is the main factor that affect the stiffness performance of this specific task. But for the large scale working path, the orientation of trajectory would affect the distribution of turning pointing a lot, thus lead to a great difference of stiffness performance. In conclusion, this method can benefit the applications of using robot in hybrid manufacturing process, especially for the larger-scale deposition process when robot carrying a heavy extruder. When considering the robot machining process, for instance, with variable heavy cutting force applied to the robot system, the stiffness analysis should integrate more influence factors.

ACKNOWLEDGEMENTS

This research was supported by Laser Aided Manufacturing Processes (LAMP) Laboratory at Missouri University of Science and Technology (Missouri S&T). Their support is greatly appreciated. The author would like to thank Morris Zhang from the National Cheng Kung university in Taiwan for his valuable contribution to the project. The author would also like to thank all the people attached directly or indirectly to the project.

REFERENCES

[1] Zha, Xuan F. "Optimal pose trajectory planning for robot manipulators." Mechanism and Machine Theory 37.10 (2002): 1063-1086.

[2] Kim, Taejung, and Sanjay E. Sarma. "Toolpath generation along directions of maximum kinematic performance; a first cut at machine-optimal paths." Computer-Aided Design 34.6 (2002): 453-468.

[3] Matsuoka, Shin-ichi, et al. "High-speed end milling of an articulated robot and its characteristics." Journal of materials processing technology 95.1 (1999): 83-89.

[4] Pan, Zengxi, et al. "Chatter analysis of robotic machining process." Journal of materials processing technology 173.3 (2006): 301-309.

[5] Nagata, Fusaomi, et al. "CAD/CAM-based position/force controller for a mold polishing robot." Mechatronics 17.4 (2007): 207-216.

[6] Zhang, Hui, et al. "Machining with flexible manipulator: toward improving robotic machining performance." Advanced Intelligent Mechatronics. Proceedings, 2005 IEEE/ASME International Conference on. IEEE, 2005.

[7] Nawratil, Georg. "New performance indices for 6R robots." Mechanism and machine theory 42.11 (2007): 1499-1511.

[8] Kucuk, Serdar, and Zafer Bingul. "Comparative study of performance indices for fundamental robot manipulators." Robotics and Autonomous Systems 54.7 (2006): 567-573.

[9] Mansouri, I., and M. Ouali. "A new homogeneous manipulability measure of robot manipulators, based on power concept." Mechatronics 19.6 (2009): 927-944.

[10] Kim, Byoung-Ho, et al. "Non-dimensionalized performance indices based optimal grasping for multi-fingered hands." Mechatronics 14.3 (2004): 255-280.

[11] Chen, Yonghua, and Fenghua Dong. "Robot machining: recent development and future research issues." The International Journal of Advanced Manufacturing Technology 66.9-12 (2013): 1489-1497.

[12] Pashkevich, Anatol, Damien Chablat, and Philippe Wenger. "Stiffness analysis of overconstrained parallel manipulators." Mechanism and Machine Theory 44.5 (2009): 966-982.

[13] Östring, Måns, Svante Gunnarsson, and Mikael Norrlöf. "Closed-loop identification of an industrial robot containing flexibilities." Control Engineering Practice 11.3 (2003): 291-300.

[14] Abele, E., M. Weigold, and S. Rothenbücher. "Modeling and identification of an industrial robot for machining applications." CIRP Annals-Manufacturing Technology 56.1 (2007): 387-390.

[15] Chanal, Hélene, Emmanuel Duc, and Pascal Ray. "A study of the impact of machine tool structure on machining processes." International Journal of Machine Tools and Manufacture 46.2 (2006): 98-106.

[16] Robin, Vincent, Laurent Sabourin, and Grigore Gogu. "Optimization of a robotized cell with redundant architecture." Robotics and Computer-Integrated Manufacturing 27.1 (2011): 13-21.

[17] Clinton, Charles M., Guangming Zhang, and Albert J. Wavering. "Stiffness modeling of a Stewart platform based milling machine." (1997).

[18] Rizk, Rani, et al. "A comparative stiffness analysis of a reconfigurable parallel machine with three or four degrees of mobility." Journal of machine engineering 6.2 (2006): 45-55.

[19] Xi, F., et al. "A comparative study on tripod units for machine tools." International Journal of Machine Tools and Manufacture 43.7 (2003): 721-730.

[20] Gosselin, Clement. "Stiffness mapping for parallel manipulators." Robotics and Automation, IEEE Transactions on 6.3 (1990): 377-382.

[21] Majou, Félix, et al. "Parametric stiffness analysis of the Orthoglide." Mechanism and Machine Theory 42.3 (2007): 296-311.

[22] Ruggiu, Maurizio. "Cartesian stiffness matrix mapping of a translational parallel mechanism with elastic joints." International Journal of Advanced Robotic Systems 9 (2012).

[23] Pinto, Charles, et al. "A methodology for static stiffness mapping in lower mobility parallel manipulators with decoupled motions." Robotica 28.05 (2010): 719-735.

III. REALIZATION OF ROBOT INK DEPOSITION ON A CURVED SURFACE

Zhiyuan Wang, Renwei Liu, Todd Sparks, and Frank Liou

Department of Mechanical and Aerospace Engineering

Missouri University of Science and Technology, Rolla, Missouri 65409, U.S.A.

ABSTRACT

A robot ink deposition system is proposed in this paper. An Additive Manufacturing (AM) concept-based method is proposed to generate an ink deposition path, and an adaptive compensation algorithm is developed for the robot to deposit ink on a curved surface based on B-spline surface theory. This method provides more flexibility for the robot arm to print characters or graph on a curved surface and affords the robot system a larger working envelope for ink deposition. A letter-printing experiment was conducted in a laboratory using this method. The results show that writing letters on the ink deposition path generated based on the AM concept is much easier than doing so on paths generated using existing methods. Additionally, the adaptive compensation algorithm for printing letters on a large curved surface proved effective.

Keywords: ink deposition; robot print; adaptive compensation; curved surface; B-spline surface

1. INTRODUCTION

Robots can work continuously and tirelessly, so their implementation typically is desirable in places where continuous operation is required, such as assembly lines. Getting a robot to behave like a human continues to be a research area of much interest. Various studies have been conducted to investigate the mechanism and control of robots that can perform the task of writing letters. A 4 DOF robot drawing platform that can write Chinese characters with a brush was developed and then later improved with the addition of a vision system [1-3]. A segmentation-based algorithm stores the character information; it focuses on segmenting the Latin character set, and the segment information then can be used by the robots to write [4]. The extraction of the trajectory of the writing brush in character writing was proposed based on image and curve processing techniques and knowledge of writing [5]. Thus far, however, this line of work typically has required complicated programs to control the robot, as well as specially designed devices, such as dedicated movement mechanisms and precise drawing planes. Moreover, the writing style and character size are limited.

The basis of writing is an ink deposition process. In this paper, a contour-points-based method based on the Additive Manufacturing (AM) concept is proposed to generate an ink deposition path and to adopt surface measurement technology to enable the robot arm to print letters on a curved white board. This method involves decomposing the shape of the characters into a set of contour points, information that the robot then can use to reconstruct the characters with linear tracks. The deposition movement of the robot along the curved surface can be adjusted by a position compensation program. This method

provides an easy way for a robot to write different styles of characters in large scale on a freeform surface.

The paper is structured as follows. The generation of the proposed ink deposition method and the measurement of the curved surface and the compensation algorithm are presented in Section 2. Section 3 describes the experiment and the results of the robot adaptive ink deposition system. Finally, some conclusions are discussed in Section 4.

2. METHODOLOGY

In the first part of this section, the method for generating the ink deposition path is introduced. Then, in the second section, the method for measuring the curved surface and the compensation algorithm are discussed.

2.1. GENERATION OF INK DEPOSITION PATH FOR THE ROBOT

Characters in different languages consist of various basic segments. The Latin language is a simple example in which characters are formed primarily with two elements, straight lines and curves. A complicated example is the Chinese language, which uses 28 different strokes as opposed to two. Extracting the sequence of writing is an arduous task requiring the design and programming of algorithms. From the perspective of geometry, a set of collinear points constitute a line, and a set of successive lines constitute a plane. The plane can be any graph, including the characters, as calligraphy could be considered a kind of plane art as well. In this way, information about the contour points of a character can be obtained, these points can be connected with tracks of a reasonable width, and the writing task can be completed using just a linear movement of the robot.

In order to obtain the graph information of the characters, the concept of AM was adopted because the writing process is just like depositing one layer of ink material. Available 3D CAD software, such as Solidworks and NX, can build 3D models of characters easily. Another advantage of this method is that the font library of 3D CAD software can be used to allow the robot to write different kinds of characters.

The algorithm for extracting the contour information of 3D models works as follows:

Step 1: Use a horizontal plane to slice the model into layers.

Step 2: Set a series vertical plane to intersect with one of the sliced layers to get the contour points.

Step 3: Generate the ink deposition path according to the contour points.

Figure 2.1 provides a detailed illustration of the method for generating the ink deposition path. Figure 2.1 (a) shows a 3D extrusion model of the Chinese character “激光” using the font library in Solidworks. Figure 2.1 (b) depicts a one-layer slice contour of the 3D character model. Figure 2.1 (c) illustrates that the segments inside the slice contour connect the contour points.

Finally, the ink deposition path can be obtained based on the AM concept. All of these steps can be accomplished using MAPS, software developed by our lab that can be used for multi-axis deposition path planning.

(a) 3D model of Chinese character “激光”

Figure 2.1 Method for generating the ink deposition path

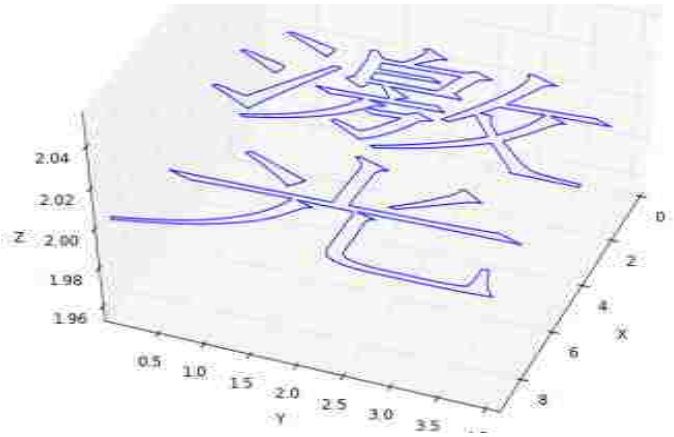

(b) one layer slice contour

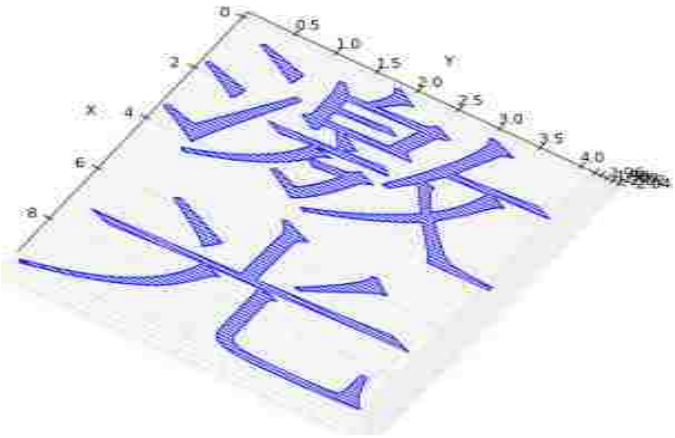

(c) segments connecting the contour points

Figure 2.1 Method for generating the ink deposition path (cont.)

2.2. MEASUREMENT OF CURVED SURFACE AND COMPENSATION ALGORITHM

When using a robot to deposit ink in a large working envelope, the absence of segments becomes a problem because the flatness of a large plane cannot be guaranteed. To realize adaptive ink deposition, a matrix of points on the board's surface first must be detected. Then, the board's surface based on B-spline surface theory can be reconstructed, and the compensation algorithm can be applied to determine the adaptive ink deposition path.

2.2.1 Curved Surface Reconstruction. The fundamental principle of reconstructing the surface [6] from the matrix of detected points is as follows: Suppose the detected points are $p_{i,j}(i = 0,1, \quad r;\ j = 0,1, \quad s)$; the expected surface can be expressed by equation (1), which has $(m+1) \times (n+1)$ control points $d_{i,j}(i = 0,1, \quad m, j = 0,1, \quad n, m = r + k \quad 1, n = s + l \quad 1)$, parameters$u$, v with times k and l, respectively, and knots vectors $U = [u_0, u_1, \quad , u_{m+k+1}]$ and $V = [v_0, v_1, \quad , v_{n+l+1}]$.

$$p(u,v) = \sum_{i=0}^{m} \sum_{j=0}^{n} d_{i,j} N_{i,k}(u) N_{j,l}(v) \tag{1}$$

Where $u_k \le u \le u_{m+1},\ v_l \le v \le v_{n+1}$.

This equation can also be revised to yield equation (2):

$$p(u,v) = \sum_{i=0}^{m} (\sum_{j=0}^{n} d_{i,j} N_{j,l}(v)) N_{i,k}(u) \tag{2}$$

Which then can yield equation (3), which is similar to the B-spline curve function:

$$p(u,v) = \sum_{i=0}^{m} c_i(v) N_{i,k}(u) \tag{3}$$

In equation (3), $c_i(v) = \sum_{j=0}^{n} d_{i,j} N_{i,j}(v)$, $i = 0,1, \quad m$, which are now control curves instead of control points. Therefore, by fixing parameter v, $m+1$ points will be given in $c_i(v)$ $(i = 0,1, \quad m)$. Those points are used as control points to define the equal parameter curve of the surface for which u is a parameter. When parameter v sweeps its whole range, infinite equal parameter curves can describe the whole surface. Clearly, $n+1$ curves are given interpolation points in the infinite equal parameter curves, which correspond to a column of points in the value points matrix. These $n+1$ equal parameter curves are called section curves [7]. The control points $\overline{d_{i,J}}(i = 0,1, \quad m;\ j = 0,1, \quad s)$ of the section curve can be calculated using equation (4).

$$s_j(u_{k+i}) = \sum_{r=0}^{m} \overline{d_{r,J}} N_{r,k}(u_{k+i}) = P_{i,j} \tag{4}$$

Where $i = 0,1, \quad m;\ j = 0,1, \quad s$.

The problem can be changed to the reconstructed calculation of $m+1$ interpolation curves:

$$\sum_{s=0}^{n} d_{i,s} N_{s,l}\left(v_{l+j}\right) = \overline{d_{i,j}}, j = 0,1, \quad r;\ i = 0,1, \quad m \tag{5}$$

By combining these equations, $(m+1) \times (n+1)$, the control point $d_{i,j}(i = 0,1, \quad m;\ j = 0,1, \quad n)$ of the surface can be calculated. Then, using the B-spline surface equation generates the surface. In the experiment described in this paper, we used a bi-cubic B-spline interpolation surface to reconstruct the robot writing surface. The reconstructed surface can be described by parametric equation (1).

2.2.2 Compensation Algorithm. The reconstructed surface also can be described by parametric equation (6).

$$p(u,v) = \begin{Bmatrix} x(u,v) \\ y(u,v) \\ z(u,v) \end{Bmatrix} \tag{6}$$

Project each point $[x_0, y_0, z_0]$ from the ink deposition path to the curved surface to obtain the corresponding point $[x_0, y_0, z_0']$, and then obtain the compensation value $cv = z_0' \quad z_0$ for each ink deposition point. The principle behind this step is as follows:

Firstly, determine u, v that satisfy equation (7).

$$\begin{cases} x(u,v) = x_0 \\ y(u,v) = y_0 \end{cases} \tag{7}$$

In order to solve (u,v), first guess the value $(u = u_g, v = u_g)$. Then, use the Newton-Raphson method to obtain the values of (u,v) numerically. According to the Taylor Series,

$$x_0 = x\left(u_g, v_g\right) + \left(u \quad u_g\right)\frac{\partial x(u_g,v_g)}{\partial u} + \left(v \quad v_g\right)\frac{\partial x(u_g,v_g)}{\partial v} + \quad ig \ \ er \quad order\ terms$$

$$y_0 = y\left(u_g, v_g\right) + \left(u \quad u_g\right)\frac{\partial y(u_g,v_g)}{\partial u} + \left(v \quad v_g\right)\frac{\partial y(u_g,v_g)}{\partial v} + \quad ig \ \ er \quad order\ terms$$

By ignoring the higher-order terms, we obtain:

$$\begin{bmatrix} \frac{\partial x}{\partial u} & \frac{\partial x}{\partial v} \\ \frac{\partial y}{\partial u} & \frac{\partial y}{\partial v} \end{bmatrix}_{(u_g, v_g)} \begin{bmatrix} u \\ v \end{bmatrix} = \begin{bmatrix} x_0 & x(u_g, v_g) \\ y_0 & y(u_g, v_g) \end{bmatrix}$$

Here, $u = u_g + \ u$, $v = v_g + \ v$.

If $[x_0 \quad x(u,v)]^2 + [y_0 \quad y(u,v)]^2 < \varepsilon$, then $z_0' = z(u,v)$.

Otherwise, let the obtained u and v be u_g and v_g, and then continue the above computation iteratively.

After obtaining the value of u, v, use parametric equation (6) to obtain $z_0' = z(u,v)$, and the compensation value $cv = z_0' \quad z_0$ for the adaptive robot ink deposition path.

3. EXPERIMENT AND RESULTS

In this paper, a robot to write characters is used as an implementation example of ink deposition. Figure 3.1 explains the entire working process of the robot ink deposition system.

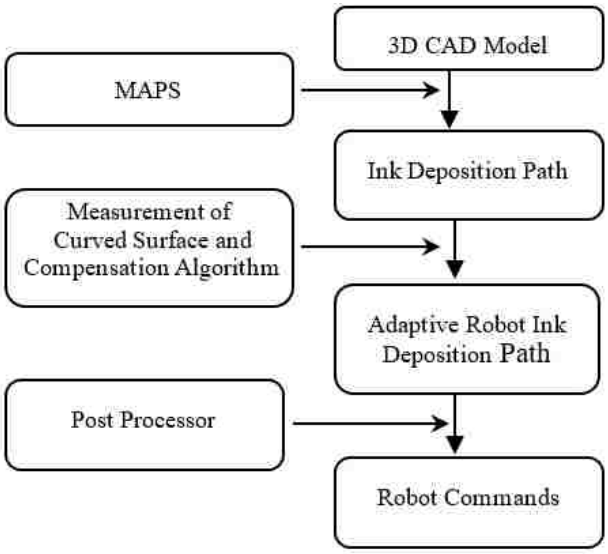

Figure 3.1 Working process of robot ink deposition system

Specifically, the ink deposition path of a character is generated by following steps.

Step 1: Generate a character model as a step file with 3D modeling software.

Step 2: Slice this model into layers, and generate the file contour points; the track width and overlap between each track can be controlled in this step. Figure 3.2 shows the robot writing path generation procedure.

Step 3: Measure and reconstruct the curved surface. Then, apply the compensation algorithm to obtain the adaptive robot ink deposition path.

Step 4: Conduct post-processing to translate information about the points into the robot commands file.

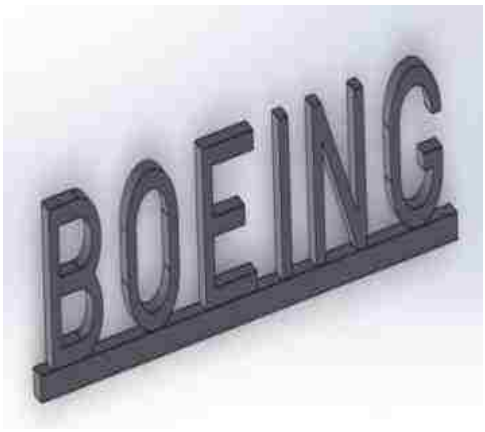

(a) 3D model of characters

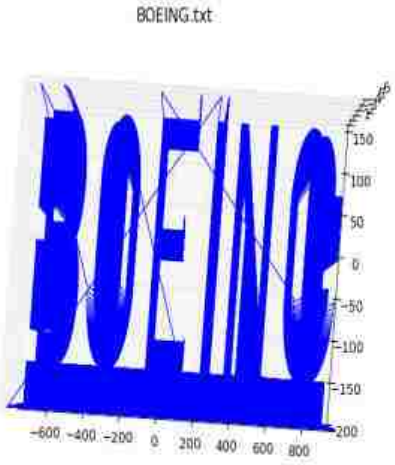

(b) contour points of characters

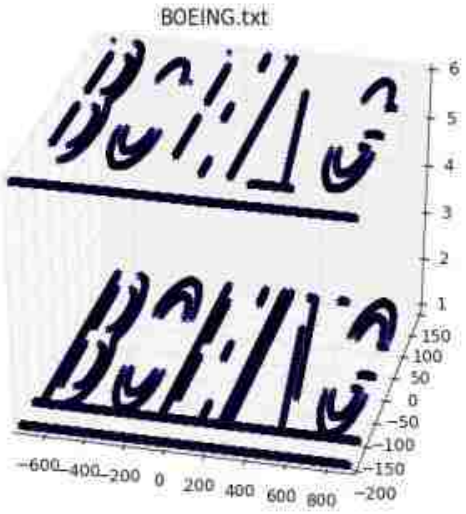

(c) simulation of robot writing path

Figure 3.2 Writing path generation procedure

A marking pen was installed on the wrist of a 7-axis industry robot arm, as shown in Figure 3.3 (a), to accomplish the writing task. The arm had 6 joints and a moveable foundation, therefore exhibiting great flexibility and a large working range (1.6m*3.4m). In this experiment, the robot was to write characters on a large white board that did not have a flat surface, especially at the four edges.

In order to write on this board, the curve information should be obtained firstly. No coordinate measuring machine can measure such a large object. As Figure 3.3 (b) shows, a touch probe installed on the robot was used to collect the points coordinate matrix of the board's surface.

(a) (b)

Figure 3.3 Robot arm and touch probe

In this experiment, 6*6 points were detected in the coordinate matrix of the board's surface, as shown in Table 3.1. Each element of the table represents the x, y, and z values of a point from the board's surface, in millimeters. Figure 3.4 (a) shows the curved white board, and Figure 3.4 (b) shows its reconstructed surface.

The compensation algorithm which introduced in Section 3 to calculate the offset for each contour point on the curved surface and to generate the final writing commands.

Table 3.1 Points coordinate matrix of the board's surface

Group 1	**Group 2**	**Group 3**
[800 -1300 742.9]	[480 -1300 741.8]	[160 -1300 741.0]
[800 -1500 752.0]	[480 -1500 752.1]	[160 -1500 751.4]
[800 -1650 754.9]	[480 -1650 756.3]	[160 -1650 755.9]
[800 -1700 755.1]	[480 -1700 757.0]	[160 -1700 756.9]
[800 -1900 752.5]	[480 -1900 757.3]	[160 -1900 758.7]
[800 -2100 745.8]	[480 -2100 753.3]	[160 -2100 757.3]
Group 4	**Group 5**	**Group 6**
[-160 -1300 739.8]	[-480 -1300 738.6]	[-800 -1300 737.5]
[-160 -1500 750.1]	[-480 -1500 748.2]	[-800 -1500 745.7]
[-160 -1650 754.5]	[-480 -1650 752.0]	[-800 -1650 747.5]
[-160 -1700 755.6]	[-480 -1700 752.8]	[-800 -1700 747.8]
[-160 -1900 757.6]	[-480 -1900 753.6]	[-800 -1900 745.8]
[-160 -2100 756.3]	[-480 -2100 750.1]	[-800 -2100 740.5]

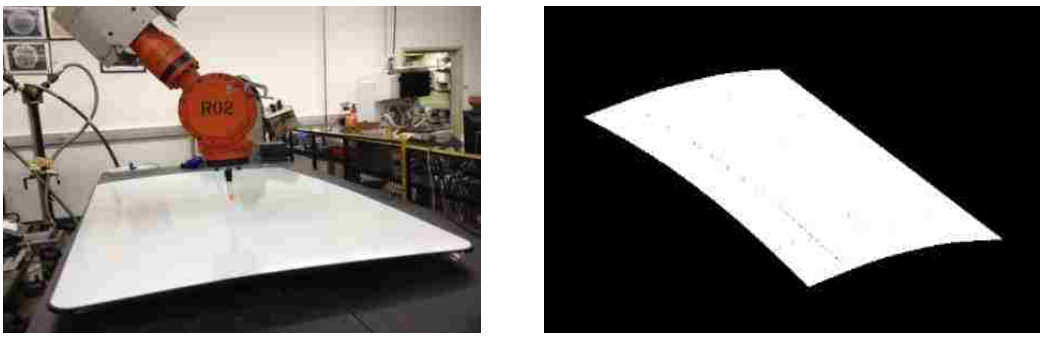

(a) (b)

Figure 3.4 Curved white board and its reconstructed surface

The writing result illustrated in Figure 3.5 shows that the entire robot ink deposition system was effective. Generating the ink deposition path using AM concepts was much easier than doing so using existing methods for writing letters. Furthermore, the system was able to deposit ink for any kind of character or graph represented in the 3D model. In this study, the height difference of the ink deposition path created using the proposed system was approximately 10mm, and the robot writing result showed no segment absence;

therefore, the compensation algorithm was effective and can support ink deposition on free-form surfaces.

Figure 3.5 Robot writing result

4. CONCLUSIONS

An adaptive robot ink deposition system aimed at writing larger-scale letters on a curved surface was developed in LAMP lab. Based on the contour points, gathering information about the 3D model and using it to reconstruct the characters is an easier method than other control algorithms for robot writing, and this process also served as a test method for robot ink deposition. Using the proposed curved surface measurement method, the robot was not limited to writing only on a flat surface. Due to the measurement limitation of laser meter, the current scanning method can only work for the slightly convex curved surface. For other complex types surface, the customized scanning algorithm should be developed. In addition, the compensation control algorithm also was shown to apply to the robot repair area, which focuses mainly on curved deposition.

ACKNOWLEDGEMENTS

This research was supported by National Science Foundation Grants IIP-0822739 and IIP-1046492, and the Intelligent Systems Center at the Missouri University of Science and Technology. Their support is greatly appreciated.

REFERENCES

[1] Lo, Ka Wah, et al. "Brush footprint acquisition and preliminary analysis for Chinese calligraphy using a robot drawing platform." Intelligent Robots and Systems, 2006 IEEE/RSJ International Conference on. IEEE, 2006.

[2] Kwok, Ka Wai, et al. "Genetic algorithm-based brush stroke generation for replication of Chinese calligraphic character." Evolutionary Computation, 2006. CEC 2006. IEEE Congress on. IEEE, 2006.

[3] Kwok, Ka Wai, Yeung Yam, and Ka Wah Lo. "Vision system and projective rectification for a robot drawing platform." Control and Automation, 2005. ICCA'05. International Conference on. Vol. 2. IEEE, 2005.

[4] Yussof, Salman, Adzly Anuar, and Karina Fernandez. "Algorithm for robot writing using character segmentation." Information Technology and Applications, 2005. ICITA 2005. Third International Conference on. Vol. 2. IEEE, 2005.

[5] Yao, Fenghui, Guifeng Shao, and Jianqiang Yi. "Extracting the trajectory of writing brush in Chinese character calligraphy." Engineering Applications of Artificial Intelligence 17.6 (2004): 631-644.

[6] Farin, Gerald E., Josef Hoschek, and Myung-Soo Kim. Handbook of computer aided geometric design. Elsevier, 2002.

[7] Woodward, Charles D. "Skinning techniques for interactive B-spline surface interpolation." Computer-Aided Design 20.8 (1988): 441-451.

IV. STEREO VISION BASED HYBRID MANUFACTURING PROCESS FOR PRECISION METAL PARTS

Zhiyuan Wang, Renwei Liu, Todd Sparks, Heng Liu and Frank Liou

Department of Mechanical and Aerospace Engineering

Missouri University of Science and Technology, Rolla, Missouri 65409, U.S.A.

ABSTRACT

This paper presents the research and development of an automatic hybrid manufacturing process which based on stereo vision and laser scanning technology to produce fully dense metal parts with CNC level precision. High performance metals, such as titanium alloys, nickel super-alloys, tool steel, stainless steels, etc., can benefit from this process. Coupling the additive and the subtractive processes into a single workstation, the hybrid process, can produce metal parts with accuracy. The surface quality of the final product is similar to the industrial milling capability. It will certainly impact the future rapid manufacturing industry. To achieve such a system, issues, including the modeling of the metal deposition process, the automated path planning and accurate surface scanning of the hybrid manufacturing process, are summarized.

Keywords: Hybrid manufacturing, Deposition process molding, Stereo Vision, Laser Surface Scanning

1. INTRODUCTION

The Directed Energy Deposition (DED) process referred here is a metal additive manufacturing process in which metal is added to the part or product, layer by layer, to rapidly manufacture or form the part or product to a predetermined shape. It is a technique that can produce fully dense functional metal parts or tools directly from a CAD system and eliminate the need for intermediate steps. An example of DED process discussed in this paper is shown in Figure 1.1.

Figure 1.1 A blown powder metal deposition process is depositing a steel part

A DED process is especially beneficial for high performance metals, such as fully dense titanium alloys, Inconel, and tool steel, which are difficult for traditional CNC machines or rapid prototyping (RP) machines to fabricate. For example, titanium and its alloys have proven to be technically superior and cost-effective materials for a wide variety of aerospace, industrial, marine, medical, and commercial applications. Parts or products cast and/or machined from these high performance metals are very expensive, partly due to the processing difficulties and complexities during machining and casting. DED processes however have been found to be very cost effective because they can produce near-net shape parts from these high performance metals with little or no machining. However, as DED processes cannot build support materials, multi-axis capability is critical

in metal deposition technologies. The hybrid manufacturing process here combines laser deposition and machining processes to develop a rapid manufacturing process to build functional metal parts. This paper summarizes the research and development of such a hybrid process, including modeling and understanding of the direct laser deposition process for distortion, and automated process planning of the hybrid process.

2. DEPOSITION PROCESS MODELING

The basis of DED process is a sound microstructure which is dominated by the created melt pool during deposition. Melt pool formed during laser deposition is a critical factor and melt pool geometry is a crucial factor in determining deposition quality. To optimize process parameters, a deep understanding of the underlying mechanisms is beneficial. A mathematical model, as shown in Figure 2.1, was developed to simulate the coaxial laser cladding process with powder injection, which includes laser-substrate, laser-powder and powder-substrate interactions [1]. The model considers most of the associated phenomena, such as melting, solidification, evaporation, evolution of the free surface and powder injection. The fluid flow in the melt pool, which is mainly driven by Marangoni shear stress as well as particle impinging, together with the energy balances at the liquid-vapor and the solid-liquid interfaces are investigated. Powder heating and laser power attenuation due to the powder cloud are incorporated into the model in the calculation of the temperature distribution. The influences of the powder injection on the melt pool shape, penetration, and flow pattern are predicted by comparison between cases with powder injection and without powder injection. Dynamic behavior of the melt pool and the formation of the clad are simulated. The effects of the process parameters on the melt pool dimension and peak temperature are further investigated based on the validated model.

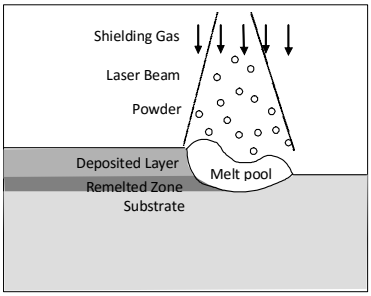

Figure 2.1 Schematic diagram of the calculation domain for laser deposition process

3. DISTORTION ANALYSIS

Highly localized heating and cooling during DMD process produces nonuniform thermal ex- pansion and contraction, resulting in complicated distribution of residual stresses in the heat affect zone and unexpected distortion in the whole structures. The residual stresses may promote fracture and fatigue and induce unpredictable buckling during the service of deposited parts and the distortion is often detrimental to the dimensional accuracies of structures. Therefore, it is vital to predict the behavior of materials after DMD process and optimize the design/manufacturing parameters to control the residual stresses and distortion.

During DED process, the substrate will continuously experience expansion and shrinkage and finally keep a deformed shape. Deformation in y direction, shown in Figure 3.1, is the main deformation under consideration and is observed by both experiments and simulations shown in Figure 3.2.

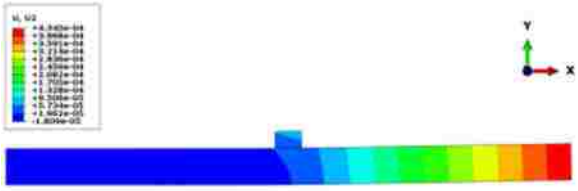

Figure 3.1 Deformation of substrate in y direction

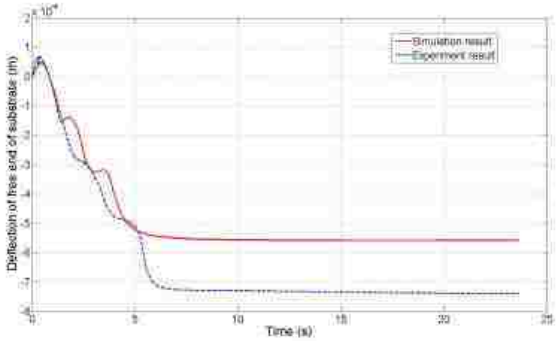

Figure 3.2 Simulation and experiment results of deflection of substrate

The distortion analysis tool allows the planning of an effective hybrid manufacturing process so that the distortion effect could be minimized through the machining process.

4. HYBRID MANUFACTURING SYSTEM

In order to expand the applications of DED processes, multi-axis capability is needed. A multi-axis rapid manufacturing system can be hardware-wise configured by adding extra degrees of mobility to a deposition system or by mounting a laser deposition device on a multi-axis robot. The configuration could also be a hybrid system in which a laser deposition system is mounted on a multi-axis CNC machine. With the addition of extra rotations, the support structures may not be necessary for the deposition process in order to build a complicated shape. Due to the nature of the deposition process, it is driven by a so-called "slicing" procedure, which uses a set of parallel planes to cut the object to obtain a series of slicing layers. So far, the slicing software on the market is only able to handle 2.5D slicing in which the building/slicing direction is kept unchanged and it lacks the capability of changing directions to fully explore the capability of multiple degrees of freedom.

This process uses laser deposition for material deposition and CNC milling for material removal. As shown in Figure 4.1, it includes two major systems: a laser deposition system and a CNC milling machine system.

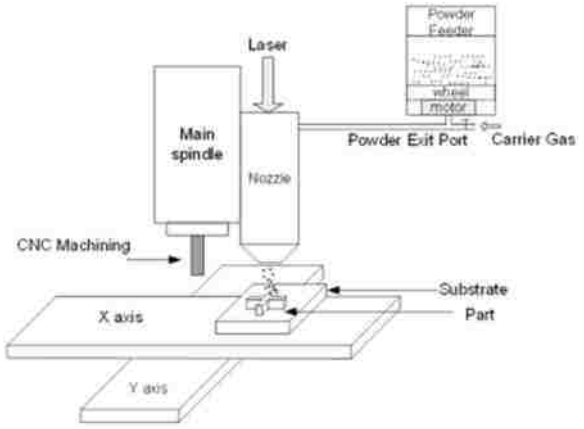

Figure 4.1 A hybrid manufacturing system: laser deposition for material deposition and CNC milling for material removal

The laser deposition system and CNC milling machine work in shifts in a five-axis motion mode. The laser deposition system consists of a laser and a powder feeder. In a conventional 2.5-D laser deposition process to create three-dimensional parts, overhang and top surfaces of hollow parts must be supported. Often support materials for functional metal parts are not feasible.

Moreover, it increases the build time of the part and necessitates a time-consuming post-processing. Additionally use of support increases the build time of the part and necessitates a time-consuming post-processing. With a five-axis deposition process integrated with five-axis machining, these obstacles can be removed.

Measurement with high resolution is the basis of precise manufacturing [2-3]. Measuring with camera could get numerous information in a short time but not accurate, the laser sensor is precision enough but relatively slow.

Stereo vision camera couple with laser displacement sensor archive a balance between speed and precision for automation path planning [4]. As shown in Figure 4.2, two level of measuring will be taken in this process: Rough and Precise. Two-eye camera adopted with stereo vision algorithm could provide the spatial information for this hybrid manufacturing system, including the position, size, shape of part, substrate, machine tool and the deposition nozzle. The work of precisely scanning in specific working area will finished by Laser displacement sensor, which the resolution of point clouds could reach to 10 microns.

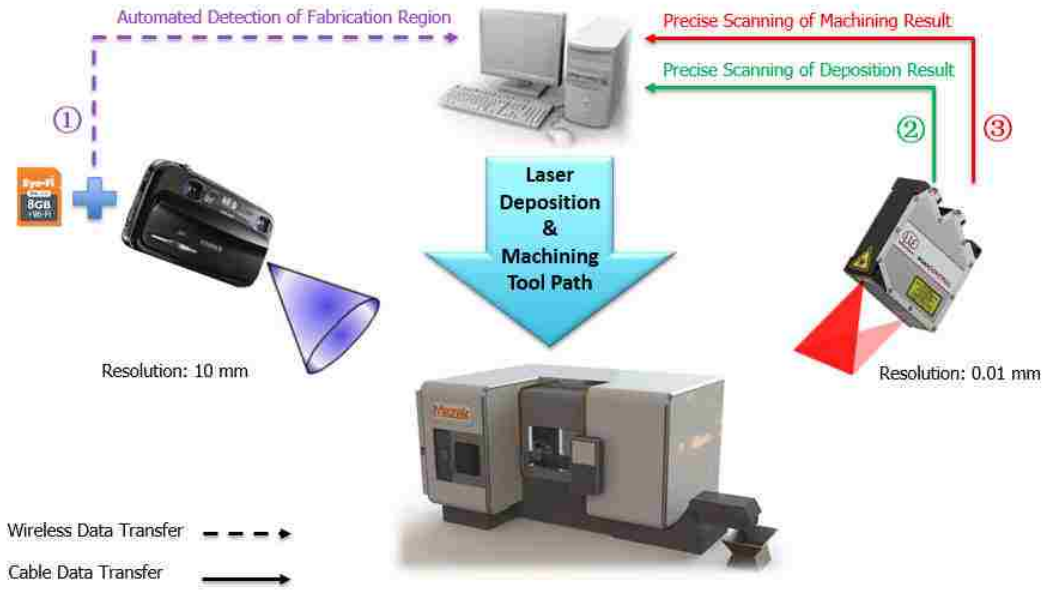

Figure 4.2 Stereo vision based path planning for hybrid manufacturing

5. STEREO VISION BASED HYBRID PROCESS PLANNING

The major issue to make an effective hybrid process is the automation of the system. Process planning, simulation, and tool path generation of a hybrid manufacturing process allow the designer to visualize and perform the part fabrication from the desktop. The Laser Aided Manufacturing Process Planning system uses B-Rep models as input and generates a description that specifies contents and sequences of operations. The objective of the process planning is to integrate the five-axis motion and deposition-machining hybrid processes. The results consist of the subpart information and the build/machining sequence. Basic planning steps involve determining the base face, extracting the skeleton, decomposing a part into subparts, determining build sequence and direction for subparts, checking the feasibility of the build sequence and direction for the machining process, and optimization of the deposition and machining [5-7].

(1) Skeleton Computation

An algorithm for computing the skeleton of the 3-D polyhedron is needed. The algorithm is based on a classification scheme for points on the skeleton computation in which the continuous representation of the medial axis is generated with associated radius functions. Because it is used as a geometric abstraction, the skeleton is trimmed from the facets that touch the boundary of the object along every boundary edge for which the interior wedge angle is less than π rad.

(2) Part Orientation

The determination of the base face from which the building process of the part starts is very important. The base face functions as the fixture in the machining process.

Therefore, when in the machining process, it must provide resistance against the cutting force. The maximal resistance force depends on the area of the base face.

(3) Part Decomposition and Building Direction

The objective of part decomposition is to divide the part into a set of subparts, which can be deposited and machined. The topology of the part can be obtained from the skeleton. Each branch of the skeleton corresponds to a subpart. One of the partitions that is performed is along a non-planar surface. Therefore, close to the partition area, 3-D layers are needed to build the connection between two subparts. The build direction of a subpart may not be constant. It changes when the part is built layer by layer so that for two adjacent layers, the later layer can be deposited based on the early layer without any support structures. To achieve the non-support build, the build directions need to be along the skeleton.

(4) Building Sequence

The results of decomposition are recorded in an adjacency graph where nodes represent subparts, and edges represent the adjacency relationship between connected nodes. After considering part building order, a directed graph that represents the precedence relationship among subparts can be constructed. From the precedence graph, one can identify in what order the subparts can be built. With the precedence graph, a set of alternative building plans can be generated. Each plan represents a possible building sequence on the decomposed geometry and can be chosen optimally depending upon machine availability or other criteria such as minimum building time.

(5) Machinability Check

The main purpose of the machinability check is to choose an optimal building sequence from the sequence set. Local and global collision checks are operated first to

choose acceptable sequences since the building direction is different in each sequence. If any kind of collision happens or an undercut plane appears, the corresponding sequence will be discarded. For the rest of the building sequences in the set, the building ability check and machining time computation is performed to find an optimal building sequence.

Stereo computer vision technology is adopted to obtain the spatial information of the part and hybrid manufacturing system. Firstly, several markers are put around the target working area on the part for image processing. After the part securely fixed on the CNC, stereo camera will take several stereo images. Then the image processing is done by stereo marker matching to get the value of three dimension coordinates in the camera coordinates system. The stereo camera calibration provides the camera intrinsic and extrinsic parameters. The spatial information in camera coordinate system could be transformed to the hybrid manufacturing environment with this information. This process is to build the relationship between CNC machine and camera coordinate system, as shown in Figure 5.1. And then the 3d coordinates of defect area on the Ti64 part in camera coordinate system is transformed to CNC machine. Equation (1) and (2) show the method to get the transformation matrix T_{cam}^{cnc} . Four spatial positions which are not in one plane on CNC machine are used to calculate T_{cam}^{cnc}. Read each coordinate of those four positions in CNC machine and then calculate the corresponding coordinate of those four positions in camera coordinates system by stereo computer vision method.

$$\begin{bmatrix} p_{1x}^{cnc} & p_{2x}^{cnc} & p_{3x}^{cnc} & p_{4x}^{cnc} \\ p_{1y}^{cnc} & p_{2y}^{cnc} & p_{3y}^{cnc} & p_{4y}^{cnc} \\ p_{1z}^{cnc} & p_{2z}^{cnc} & p_{3z}^{cnc} & p_{4z}^{cnc} \\ 1 & 1 & 1 & 1 \end{bmatrix} = T_{cam}^{cnc} \begin{bmatrix} p_{1x}^{cam} & p_{2x}^{cam} & p_{3x}^{cam} & p_{4x}^{cam} \\ p_{1y}^{cam} & p_{2y}^{cam} & p_{3y}^{cam} & p_{4y}^{cam} \\ p_{1z}^{cam} & p_{2z}^{cam} & p_{3z}^{cam} & p_{4z}^{cam} \\ 1 & 1 & 1 & 1 \end{bmatrix}$$

$$\Rightarrow \quad points^{cnc} = T_{cam}^{cnc} \times points^{cam} \tag{1}$$

$$\Rightarrow \quad T_{cam}^{cnc} = points^{cnc} \times inv(points^{cam}) \tag{2}$$

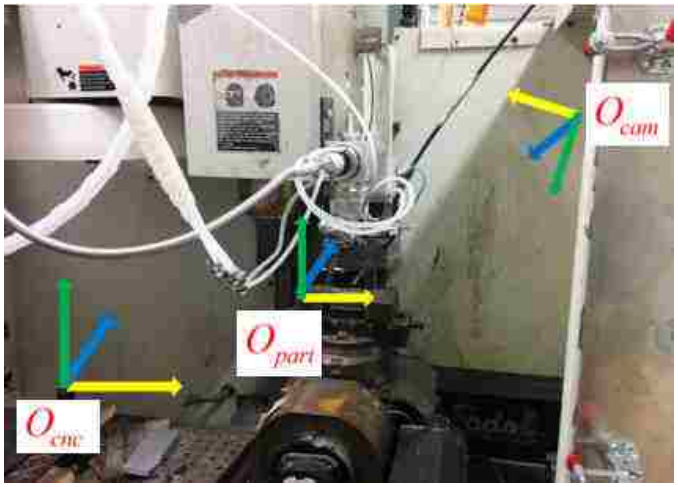

Figure 5.1 Coordinate Relationship between camera, CNC, and part

6. RESULTS

Laser displacement sensor is used to scan the geometry of deposition result and machining area. The resolution of measurement can be reach to 10 microns. These accurate dimension data are basis for path planning of near-net manufacturing. Point clouds of the deposition area is used to generate the machining tool path. Figure 6.1 shows the laser displacement sensor is scanning a deposition sample on Ti64 substrate. Figure 6.2 describes the machining tool path according to this point clouds information.

Figure 6.1 Accurate surface scanning with laser displacement sensor

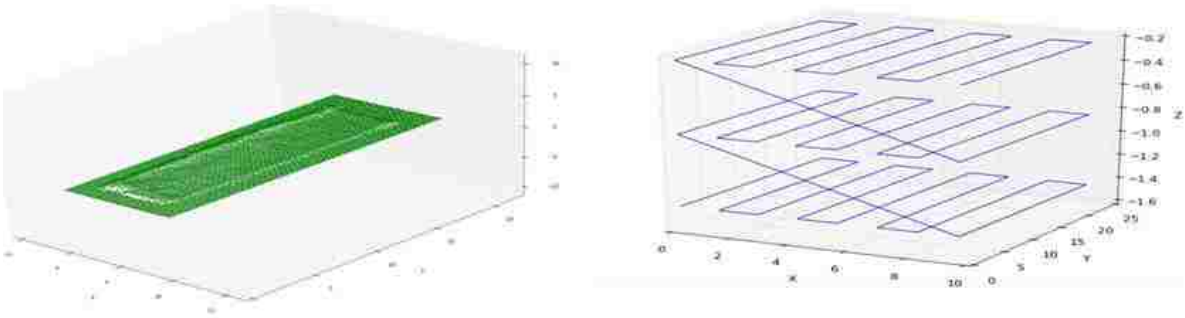

Figure 6.2 Point clouds of scanning results and the machining tool path

The bearing seat example as shown in Figure 6.3 (a) and its deposition result are shown here. Figure 6.3 (b) shows the planed tool path for both deposition and machining,

Figure 6.3 (c) shows the part in H13 tool steel being deposited, and Figure 6.3 (d) shows the part after machining.

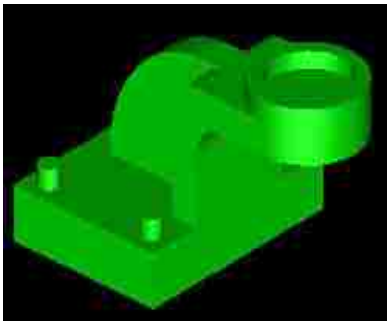

(a) CAD model

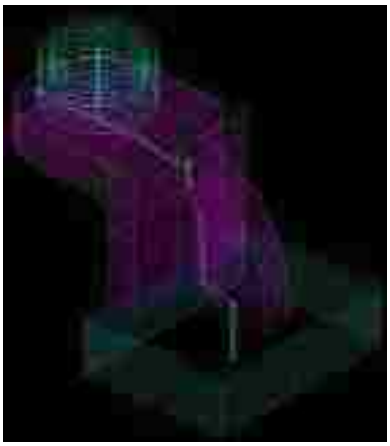

(b) Automated generated tool path for deposition and machining

(c) Laser deposition

Figure 6.3 Hybrid manufacturing of an H13 tool steel bearing seat part

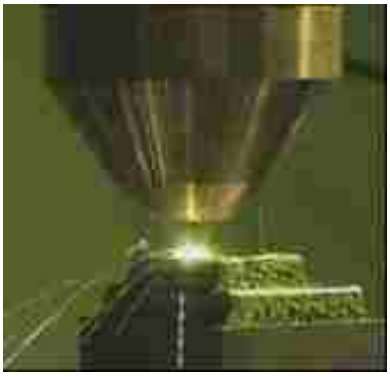

(d) After machining

Figure 6.3 Hybrid manufacturing of an H13 tool steel bearing seat part (cont.)

7. CONCLUSIONS

Making precision metal parts is a critical additive manufacturing technology as it can directly produce finished products or parts for high performance applications. The current limitations of additive processes include surface finish, repeatability, and material properties. The research and applications of a stereo vision based hybrid metal manufacturing system are summarized in this paper. The issues include understanding the DED process, the stereo vison aided automated process planning, and laser displacement sensor surface scanning. The modeling and simulation of material-laser interaction help design and set the process parameters for metal deposition. The stereo vison based path planning and laser sensor scanning make the process has less involve with manual operation, enhance the automation and accuracy of additive manufacturing process. The overall goal for process planning is not only to find a solution to build a part but also to look for an answer to produce it in the least amount of time; therefore, the least amount of switching between the machining process and deposition process, the better since each switch requires retreating and relocating the deposition nozzle as well as the machining tool, which may cost extra time. With integration of multi-axis deposition and machining processes on the same work station, a hybrid system is able to produce complicated geometry, especially the overhang structure with less or no support structures. Based on different geometry shapes, the five-axis system can save close to 100% of support materials. The surface quality of the final product is similar to the industrial milling capability. As there is a big demand in precision metal additive manufacturing applications, a more sophisticated process planner and general purpose for hybrid manufacturing systems is needed.

ACKNOWLEDGMENTS

This research was supported by the National Science Foundation Grant Numbers IIP-0637796, IIP-0822739, and IIP-1345240, and the grant from the U.S. Air Force Research Laboratory contract # FA8650-04-C-5704, and Missouri S&T Intelligent Systems Center. Their support is greatly appreciated.

REFERENCES

[1] Han, L.; Liou, F.W.; and Phatak, K.M., (2005) “Modeling of Laser Cladding with Powder Injection,” Metallurgical and Materials Transactions B, Volume 35B, pp. 1139-1150.

[2] J. Hur, K. Lee, h. Zhu, J. Kim, Hybrid rapid prototyping system using machining and deposition, Computer-Aided Design, 34 (2002) 741-754.

[3] Hur, Junghoon, Kunwoo Lee, and Jongwon Kim. "Hybrid rapid prototyping system using machining and deposition." Computer-Aided Design 34.10 (2002): 741-754.

[4] J. Gao, J. Folkes, O. Yilmaz, N. Gindy, Investigation of a 3D non-contact measurement based blade repair integration system, Aircraft Engineering and Aerospace Technology, 77 (2005) 34-41.

[5] Liou, Frank; Slattery, Kevin; Kinsella, Mary; Newkirk, Joseph; Chou, Hsin-Nan; Landers, Robert, “Applications of a Hybrid Manufacturing Process for Fabrication and Repair of Metallic Structures,” Rapid Prototyping Journal, 2007, ISSN: 1355-2546, 2007 Volume: 13 Issue: 4 Page: 236 - 244.

[6] Ruan, J.; Eiamsa-ard, K.; and Liou, F., (2005) “Automatic Process Planning and Toolpath Generation of a Multi-Axis Hybrid Manufacturing System,” SME Journal of Manufacturing Processes, Vol 7, No. 1, pp. 57-68.

[7] Liou, Frank; Slattery, Kevin; Kinsella, Mary; Newkirk, Joseph; Chou, Hsin-Nan; Landers, Robert, “Applications of a Hybrid Manufacturing Process for Fabrication and Repair of Metallic Structures,” Rapid Prototyping Journal, 2007, ISSN: 1355-2546, 2007 Volume: 13 Issue: 4 Page: 236 - 244.

V. LARGE-SCALE DEPOSITION SYSTEM BY AN INDUSTRIAL ROBOT (I) – DESIGN OF FUSED PELLET MODELING (FPM) SYSTEM AND EXTRUSION PROCESS ANALYSIS

Zhiyuan Wang, Renwei Liu, Todd Sparks, Heng Liu and Frank Liou

Department of Mechanical and Aerospace Engineering

Missouri University of Science and Technology, Rolla, Missouri 65409, U.S.A.

ABSTRACT

Fused pellet modeling (FPM) is an important method in additive manufacturing technology that uses granular material instead of filaments. In FPM, prototypes are constructed by the sequential deposition of material layers. As the size of the part increases, the long build times and part deformations become critical problems. Methods for optimizing the extrusion process to eliminate the void density during large scale FPM processes were studied. Based on analyzing polymer extrusion theory and non-Newtonian fluid properties, a mini extruder with a variable pitch and a progressive diameter screw has been proposed for large scale fused pellets deposition. Each of the design parameters, such as the lengths of different function sections of screw, die shape of extruder nozzle, and the material properties was analyzed. According to these analysis results, an extrusion process simulation for controlling the filament shape was carried out with multi-physics modeling software proving that the FPM could increase the building efficiency and deposition quality for large-size parts.

Keywords: Fused pellet extruder, Robot deposition, Polymer extrusion, Non-Newtonian fluid

1. INTRODUCTION

Layered manufacturing with extruded material is one of the most promising rapid prototyping techniques that demonstrates novel design ideas and reduces the product development cycle. This process fabricates prototypes by extruding the material in a semi-fluid status through a heated nozzle in a prescribed pattern onto a platform. Various types of material could be applied in this process, including polymer, cement, plaster, and wax.

The deposition material should be extruded continuously, stably, and under constant temperature during the layered manufacturing process. “Continuously” means there should be no interruption of extrusion when the nozzle scans the deposition path; “stably” involves the stable extrusion amount and accurate geometry of the semi-molten material; and “thermostatic” is to ensure the bonding quality is acceptable between deposition tracks.

The fused deposition modeling (FDM) developed by Stratasys Inc. has been a leading rapid prototyping technology that involves layer by layer deposition of extruded material through a nozzle using feedstock filaments from a spool [1]. The material feeding process of filament based extrusion is realized by two friction wheels that rotate reversely to push the filament into a heated nozzle as shown in Figure 1.1. Because of the simple structure and easy control, it has been widely used in most of the fused deposition systems. But the weak points of this method are also very obvious. The extrusion force is limited by the filaments’ surface compressive strength and the contact area between the friction wheels and filament. Insufficient friction will cause slip feeding, and too much compressive force applied on the filament might break it off. Both of these will affect the extrusion quality. To shift from rapid prototyping to agile fabrication by broadening the

material selection and to improve the properties of fused deposition modeling, N. Volpato et al [2] proposed a piston driven extrusion head that can extrude polypropylene granules into a filament. However, the problem of this method that related to filament uniformity should be addressed. Also adopted granulated material, Anna Bellini et al [3] presented a novel extrusion system that was mounted on a high precision positioning system and fed with plastic pellets. This research area also drawn significant interests from industry. Cincinnati Incorporated commercialized a Big Area Additive Manufacturing (BAAM) machine that could use granulated material to build a body of car within a gantry deposition system, but it still confined by an enclosed working envelope. Lockheed Martin teamed with Oak Ridge National Laboratory (ORNL) designed a system that accommodate a team of coordinated robots working in an open air environment to produce components and structures unbounded in size, they adopted a screw extrusion unit which enables the use of advanced polymer composites, multiple material within a single component [4]. Although this screw extrusion system could perform better than other filament based extrusion systems, the normal single screw is still not the most suitable structure for the fused material extrusion process.

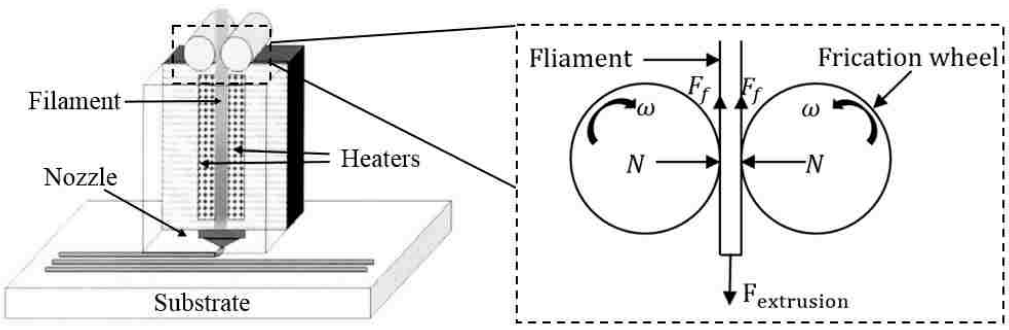

Figure 1.1 Schematic of filament based extrusion systems

As the size of the part increases, the problem of long build times and part deformation becomes more critical. Currently, most filament based 3D printers equipped with 0.3 mm-0.8 mm diameter nozzles, and the printing speed of those between 30 mm/s - 120 mm/s, even some printers can go up to 200 mm/s, it would still take a long time to build a big part. In addition, inner stresses resulting from the contraction of deposition fibers within one layer can affect the precision of the prototype's size and bring about prototype deformations, including warp and inner-layer delaminating or cracking. Similar quality issues exist in other rapid prototyping processes. Many researchers have investigated the inner stresses. Tian-Ming Wang et al. [5] constructed a mathematical model of the prototype warp deformation to analyze each of the influencing factors. Jayanthi et al. [6] discussed how the scanning pattern of the laser in stereolithography (SLA) influences the resulting deflection of the part. Céline Bellehumeur [7] studied the dynamics of bond formation between polymer filaments using thermal analysis and sintering experiments under different conditions. This same group performed a more in-depth study on the mechanisms that control the bond formation under different process conditions [8].

To avoid most of the defects that occur during the material extrusion steps in a filament-based system, a mini screw extrusion system has been proposed, developed, and specially designed to build large objects using the layered manufacturing technique. The new set-up is called fused pellet modeling (FPM) system. The FPM consists of a mini extruder mounted on an industry robot arm. It operates using bulk material in a granulated form. With the special designed progressive screw, this mini extruder could provide higher extrusion speed and better extrusion quality. In addition, theory analysis and simulation

work have done on optimizing the nozzle geometry, to eliminate the deposition defects happened in conventional fused deposition method. This configuration opens up opportunities to use a wider range of materials. Meanwhile the robot arm makes the fused pellet modeling process a more flexible and viable alternative rapid for the prototyping of large part.

2. SYSTEM SPECIFICATIONS

Screw extrusion has been widely adopted in the polymer manufacturing industry because of its extremely excellent attribute for processing. The plastic melts as it moves along the screw. Initially, a thin film of molten material is formed at the barrel walls. As the screw rotates, it scrapes this film off, and molten plastic moves down the front face of the screw flight. When the material reaches the core of the screw, it sweeps up again, setting up a rotary movement in front of the leading edge of the screw flight. Initially, the screw flight contains solid granules, but these granules tend to be swept into the molten pool by the rotary movement. As the screw rotates, the material passes further along the barrel, and more and more solid material is swept into the molten pool until, eventually, only melted material exists between the screw flights.

Applying the screw extrusion method into the fused deposition process is not simple. The key component in the system is the extrusion screw. But the length of screw for extrusion machine in plastic industry is normally from 80 inch to 200 inch. Those extrusion systems are too big to apply on robot deposition process, because the nozzle needs to keep a certain scanning speed during the deposition process, it requires the weight and volume of the extrusion unit to be within a certain range, so it is crucial to design and manufacture a small screw for the mini extrude. Some researchers have tried to use a common screw for extrusion. A common screw could work for several kinds of material, like ceramic and plaster, because these material are already in viscous state, the screw rotation only provide the force for material moving forward. But for the polymer pellets, the material will experience state change from solid plastic to viscous fluid. The mini screw with a variable pitch and a progressive diameter could form a volume changing inside of

the barrel, the material will be mixed uniformly by the pressure which generated when material moving forward.

In combination with the barrel, the screw converts solid material to the melted status and efficiently pumps the material to the die. To obtain a good extrusion performance, the screw for FPM system should be designed with three different function sections: feed, transition, and metering. The feed section is the first element of the screw where the polymers are introduced. The wide pitch P_1 and small diameter D_1 could provide the greatest feeding volume and frication force for pushing the polymer material forward, because the dry friction occurred between the solid state pellets and inner wall of the barrel at this section. The transition section (or compression section) is where most of the polymer melting takes place. This is the portion of the screw that "transitions" from the feed depth to the metering depth. This portion is also where the work is done on the resin to cause melting to occur. In this section, the root of the screw gradually becomes shallower, forcing the material towards the wall of the heated barrel where the melting takes place. Last but not least is the metering section, or pumping section, of the screw. This is where the polymer melting is completed and pumping occurs to overcome the head pressure.

The first design requirement of the extrusion screw is L/D ratio, as shown in Figure 2.1. It being defined as the "enclosed" portion of the screw, or the flighted length form the front side of the feed port to the end of the screw. Typical extruder L/Ds are 24:1 and 30 or 32:1, but there are special applications where extruder are built as 10:1 L/D and as long as 50:1 L/D. The proper L/D is determined by the process and application that is being satisfied. Considering minimize the extruder unit volume and realize high extrusion amount for this proposed design, L/D ratio has chosen as 10:1.

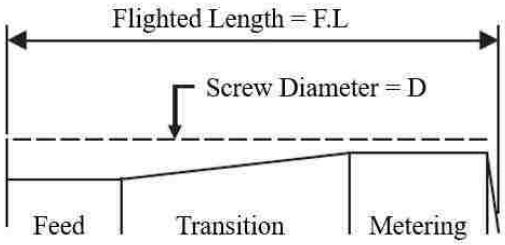

$$L/D = \frac{\text{Flighted Length (F.L)}}{\text{Screw Diameter (D)}}$$

Figure 2.1 Schematic of a progressive screw

Another important design requirement is the length and diameter of different sections. As the function described above, feed section is the deepest portion of the screw, special attention needs to be given to this section of the screw in order to reduce twisting the screw in half due to over torque of the screw. For this design, the raw material of screw is 8620 hot roll steel, according to empirical formula for screw design, the depth of feed section is $F_{dmax} = 0.2 \quad (Screw\ Diameter) = 0.4\ inc$. The depth of metering section is determined as 0.2 inch for provide volume changing for compression along the screw. The screw pitch also decreased from the end to the front of screw, feed section is 1.5 inch, transition section is 1.0 inch, metering section is 0.6 inch, respectively. Usually, the length of feed section set as L1 = (3~5)*D, the length of transition section determined based on the heating ability and rotation speed, L2 = (6~8)*D, so the ratio of section length for this design is L1 : L2 : L3 ≈ 2:3:1. The screw is machined on a 5-axis CNC, used its helix expand command, the G-code is shown in Table 2.1. The finial manufacturing result of progressive screw shown as Figure 2.2.

Table 2.1 G-code for manufacturing progressive screw

N1 02010 (Progressive Screw)	N25 X12.80 Y62.8318
N2 G90	N26 X13.00 Y62.8318
N3 S800	N27 X15.10 Y69.11498
N4 F3.	N28 X17.20 Y75.39816
N5 G17	N29 X15.10 Y69.11498
N6 G58	N30 X13.00 Y62.8318
N7 M6 T3	N31 X11.45 Y56.54862
N8 G58 Z0	N32 X5.60 Y31.4159 Z (0:-0.2:-0.1)
N9 G43 H3	N33 X4.60 Y25.13272
N10 G59	N34 X1.40 Y0
N11 G5 Z3	N35 X1.45 Y0
N12 G90	N36 X4.65 Y25.13272
N12.1 S3000 M3	N37 X5.85 Y31.4159
N13 X1.40 Y-1. Z0 F27.	N38 X11.45 Y56.54862 Z (0:-0.4:-0.1)
N14 Z (0:-0.2:-0.1)	N39 X13.25 Y62.8318
// cutting start height z=0;	N40 X17.45 Y75.39816
// cutting end height z=-0.2;	N41 X16.45 Y75.39816
// cutting depth z=-0.1	N42 X14.35 Y69.11498
N15 Y0	N43 X12.35 Y62.8318
N16 G17 Q2.8648	N44 X10.95 Y56.54862
N17 X4.60 Y25.13272	N45 X5.35 Y31.4159 Z (0:-0.2:-0.1)
N18 X5.60 Y31.4159	N46 X4.55 Y25.13272
N19 X11.20 Y56.54862 Z (0:-0.4:-0.1)	N47 X1.35 Y0
N20 X12.60 Y62.8318	N48 X1.45 Y0
N21 X14.60 Y69.11498	N49 Z0.5
N22 X16.70 Y75.39816	N50 X1.35 Y0 F200.
N23 X16.95 Y75.39816	N51 G17
N24 X14.85 Y69.11498	

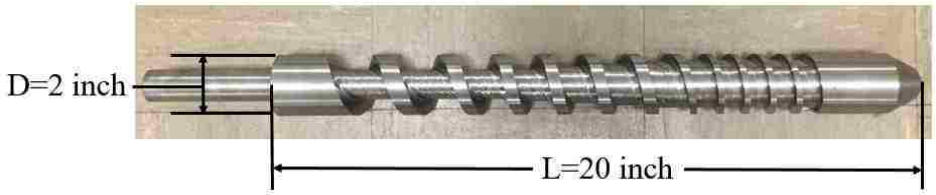

Figure 2.2 Progressive screw for mini extruder

This mini extruder is mounted on an industry robot as shown in Figure 2.3(a). It has a 4.1 m^2 (cross-section area) operating area and a 300 rotation range for the base motor (Figure 2.3(b)), which could provide a much bigger deposition working envelope than the current fused deposition system. The 6-axis movement mechanism makes the deposition process more flexible in building a model with complex features.

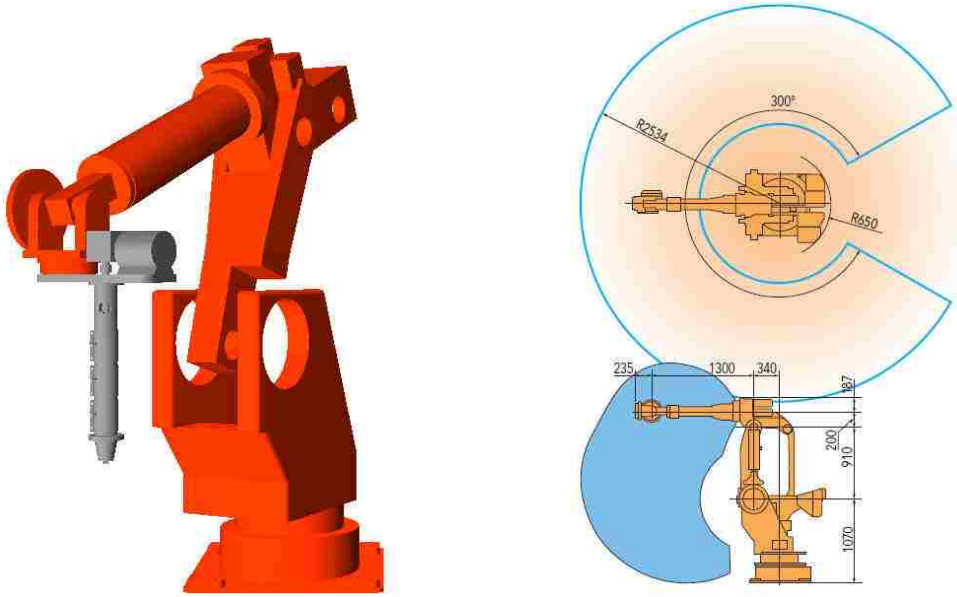

(a) Assembly model of FPM system (b) Robot's working envelope

Figure 2.3 Assembly model of FPM system on the industry robot and working envelope

3. ACCURACY CONTROL OF THE EXTRUSION PROCESS

The void density caused by the gap and overlap between deposition tracks is an inevitable defect of the filament based extrusion system. It will also result in part deformation and deposition failure. To analyze the effect of void density in the deposition process, L. Li [9] proposed a method to calculate it theoretically. For each laminate, axis d is normal to the plane of filament's cross section, define ρ_1 as the area void density, g as the gap size.

When g =0, there are no gaps among the filaments. The ideal cross section is shown in Figure 3.1. The cross section shape of the filament is an ellipse with a and b representing the idealized lengths of the semi-major axis.

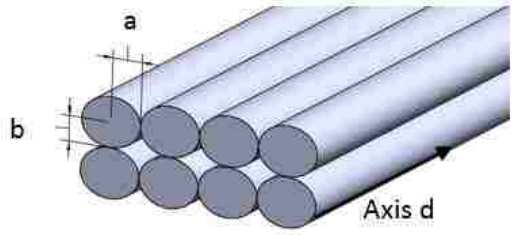

Figure 3.1 Ideal cross section of deposited filament

In the actual process, the top and bottom surfaces of the filament would flatten when deposited onto previous layers. This is from the vertical force of extrusion in a semi-molten state. Therefore, the modified calculation model is shown in Figure 3.2(a), considering the flattening effect of δ can be measured experimentally. Assuming that the total cross sectional area stays unchanged, the relation between areas Q and P should be:

$$Q = 2P \tag{1}$$

Assuming δ is a small amount, the flattened area has the same length as the long semi-axis of the filament ellipse. Thus, the void density can be calculated using the following equation:

$$\rho_1 = 1 - \frac{\pi ab}{2a(2b-\delta)} \tag{2}$$

The real cross section for this situation is also indicated in the microscopic photo in Figure 3.2(b).

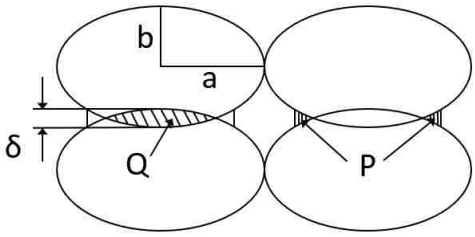

(a) Schematic diagram of deposited filament with flattening effect

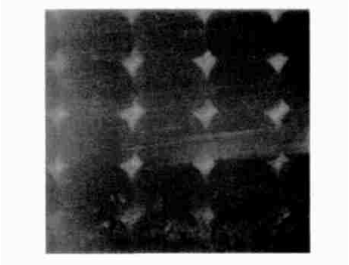

(b) Microscopic cross section of deposited filament

Figure 3.2 Deposited filament with flattening effect and photo of microscopic cross section

When $g = \pm\Delta$, there is a gap or overlap between deposition tracks, as shown in Figures 3.3(a) and Figures 3.4(a). The cross section photos of filaments were taken under microscopic, as shown in Figures 3.3(b) and Figures 3.4(b), respectively.

$$\rho_1 = 1 - \frac{\pi ab}{(2a \pm \Delta)(2b-\delta)} \tag{3}$$

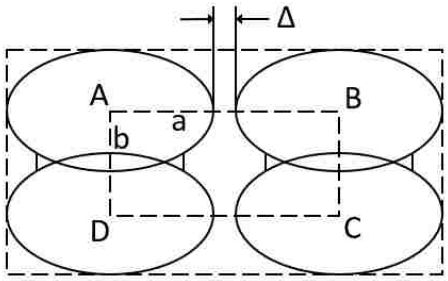

(a) Schematic diagram of deposited filament with positive gap

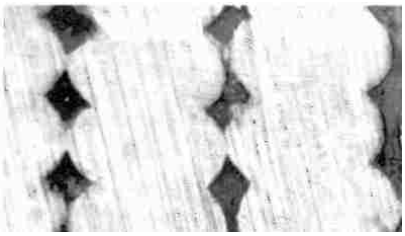

(b) Microscopic cross section of deposited filament

Figure 3.3 Deposited filament with positive gap and photo of microscopic cross section

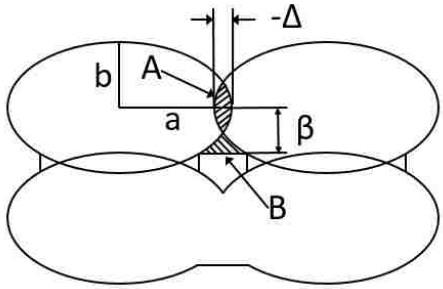

(a) Schematic diagram of deposited filament with negative gap

(b) Microscopic cross section of deposited filament

Figure 3.4 Deposited filament with negative gap and photo of microscopic cross section

The smaller area of void density means a better deposition quality. Increasing δ and using a minus gap setting could decrease the ρ_1, but because of the nozzle's structure

more deposition layers and denser deposition tracks are required, δ has a limitation as well. The result would be a longer building time.

Obviously, the void density problem in conventional filament based deposition process caused by the elliptical shape of extruded filament's cross section. To solve this problem, FPM system could realize extruding filament with rectangle shape cross section by analyzing the plastic extrusion process and extrusion material property.

The polymer material changes into three different physical states, sequentially, from when it is fed into the barrel to when it is extruded out through the nozzle: a glass state, a high elastic state, and a viscous flow state. Because the molten polymer has a high viscosity and significant elasticity, it should be considered as a kind of viscoelastic material that exhibits non-Newtonian fluid properties.

One important feature of a non-Newtonian fluid is the Barus effect [10], which is an expansion phenomenon of a non-Newtonian fluid that occurs when it emerges from a nozzle to an open space such that the diameter of the emerging stream can be several times the nozzle diameter, and the expansion ratio is varied from the edges to the corners. When the molten polymer is extruded out from the nozzle, it expends along the edge.

The longer the edge, the more significant the expansion is. This results in the filament shape of the extruded material been different from the shape of the nozzle (Figure 9). Therefore, if the expected filament shape is a rectangle, the shape of the nozzle should be similar to the third shape in Figure 3.5.

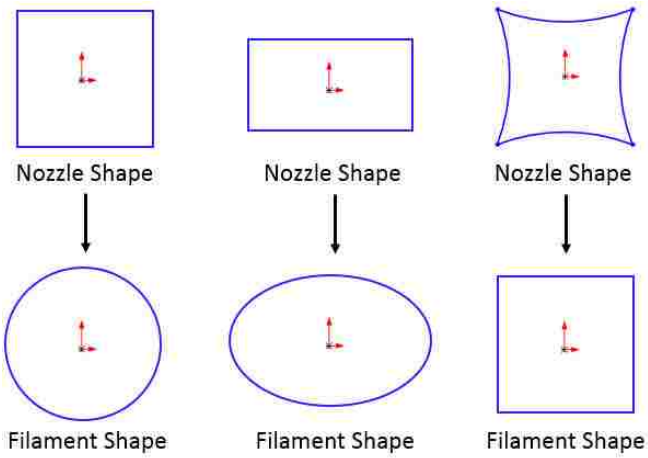

Figure 3.5 Barus effect with different nozzle shapes

By controlling the parameters of the extrusion process, including screw ration speed (this one will directly affect the back pressure in the barrel), temperature of heating bands, the pellets feed amount and the shape the nozzle, a rectangle-shaped of filament, as shown in Figure 3.6 could be obtained to decrease the void density and enhance the deposition quality.

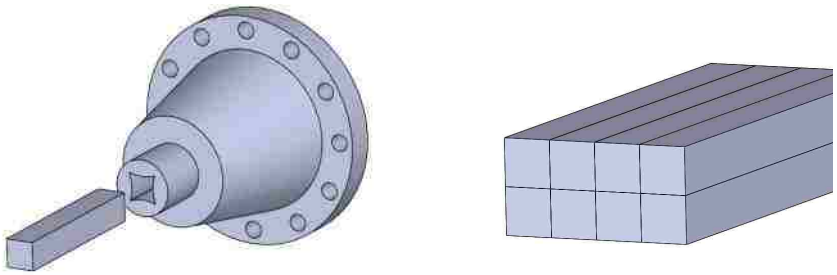

(a) (b)

Figure 3.6 Model of nozzle for extruding rectangle filament and the ideal deposition results

4. EXTRUSION PROCESS MODELING AND DISCUSSION OF SIMULATION RESULTS

For a non-Newtonian flow, μ denotes the viscosity (kg/(m·s)), u the velocity (m/s), ρ is the density of the fluid (kg/m^3), and p the pressure (Pa). The equations to solve are the momentum and continuity equations are, respectively, as follows:

$$\rho\frac{\partial u}{\partial t}-\nabla\cdot\mu(\nabla u+(\nabla u)^T)+\rho u\cdot\nabla u+\nabla p=0 \tag{4}$$

$$\nabla\cdot\mu=0 \tag{5}$$

In the Carreau model, the viscosity depends on the shear rate, $\dot{\gamma}$, which, for an axisymmetric model in cylindrical coordinates, is defined according to Equation 2:

$$\dot{\gamma}=\sqrt{\frac{1}{2}\left((2u_r)^2+2(u_r+v_r)^2+(2v_z)^2+4(\frac{u}{r})^2\right)} \tag{6}$$

The viscosity is given by

$$\mu=\mu_\infty+(\mu_0-\mu_\infty)[1+(\lambda\dot{\gamma})^2]^{\frac{(n-1)}{2}} \tag{7}$$

where μ_∞ is the infinite shear rate viscosity, μ_0 is the zero shear rate viscosity, λ is a parameter with units of time, and n is a dimensionless parameter.

The section view of the nozzle in this FPM system is shown in Figure 4.1(a). An inside volume model of the nozzle was built, as shown in Figure 4.1(b), to analyze the flow behavior of the molten polymer material in COMSOL multi physics.

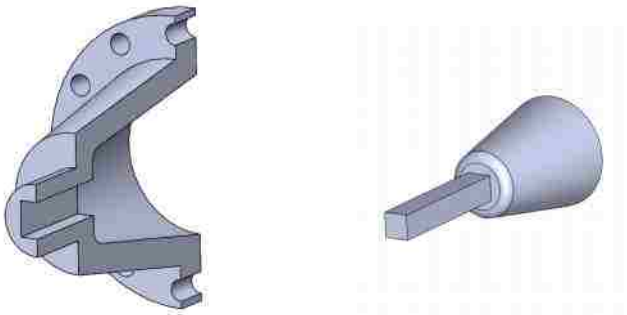

(a) (b)

Figure 4.1 Cross section view of nozzle and the inside volume model

Three different nozzle shapes were designed to analysis the Barus effect of the extruded molten polymer. The inside volume models of the nozzle were also modeled, respectively (Figure 4.2). Shape-1 represents the original rectangle shape die. The edge length is 0.5 inch. Shape-2 represents the modified shape die. The edge contracted inward, obviously. The radius of the arc is equal to the length of the rectangle, and the arcs are tangent to each other. Shape-3 represents the improved shape die. The edge contracted inward slightly. The radius of the arc is 0.7 inch, and the radius of the fillet at each corner is 0.01 inch.

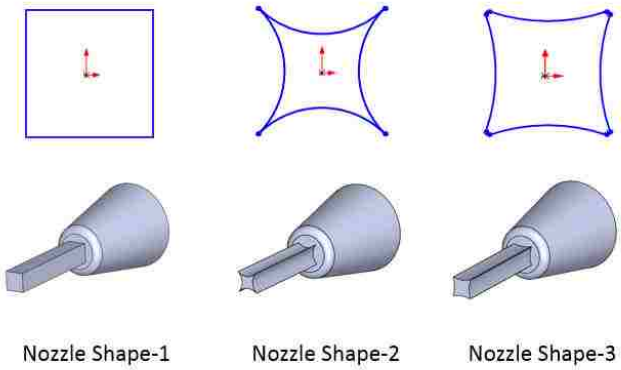

Figure 4.2 Cross section sketch and 3D model of three different nozzle shapes

The inside volume model represents the material that is extruded out from the barrel through the die of the nozzle. The flow behavior of the melted material follows the non-

Newtonian flow equations. Because of the symmetrical geometry feature, and for computation efficiency, the model could be simplified as a single quadrant, shown as in Figure 4.3. To compare how different nozzle shapes affect extruded filament shape, the boundary conditions and mesh parameters set as same for these simulations in COMSOL: wall boundary is no slip, pressure at inlet boundary is 23 MPa , pressure at outlet boundary is 0 MPa , mesh type is tetrahedral, maximum element size is 0.058.

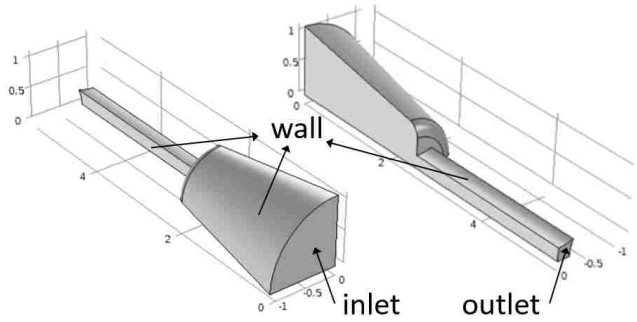

Figure 4.3 Quadrant inside volume models and definition of boundaries

The material subdomain settings for low density polyethylene (LDPE) at around 220 degrees centigrade [11] are shown in Table 4.1. The convergence could be achieved when the mesh is tuned sparser, it is also affected by the boundary conditions and material properties. With current boundary conditions and the property of LDPE material, the model is stable and convergent.

Table 4.1 Subdomain settings for LDPE material

Viscosity model type	**Carreau model**
Density of melt LDPE (rho)	743 kg/m^3
Zero shear rate viscosity	1437.4Pa.s
Model parameter (n)	0.39
Model parameter (λ)	0.015s

When a non-Newtonian flow comes out from the nozzle with a certain speed and back pressure, the inner pressure of the flow forces the material to expand in the open space. This is the macro phenomenon of the Barus effect, which results in the extruded material swelling and coming out with an oval shape or another unexpected shape. Usually the working pressure of plastic extrusion machine is 20 MPa. As the screw rotation speed increasing, extrusion pressure will rise up, obvious Barus effect will happen when the pressure reach to 22.5 MPa-26 MPa, specific value is varied according to different material property and other system parameters, like L/D ratio, pellets feed amount, et al. This phenomenon could be reflected in the pressure plot of nozzle outlet cross section of the simulation results. Figure 4.4 shows the meshed inside single quadrant volume models of three different shaped nozzles and the cross section pressure distribution plot at the outlet of each nozzle, respectively. Normalized pressure scale is used in the figures to illustrate the color difference of maximum and minimum pressure.

The polymer material filament will swell when it comes out from the nozzle of screw extruder, because the internal pressure of material will drive the filament expand to different shape. As shown in Figure 4.4(a), for the rectangle shape nozzle, the pressure distribution along the rectangle's edge is higher than the pressure at the corner section, the filament tends to expand to a round similar shape. Figure 4.4(b) shows the pressure distribution plot of the modified nozzle shape, which shrank too much from each edge. It resulted that the pressure was concentrated at the corner because of the stress cusp effect. These pressure distribution plots illustrate that the simulation corresponded to the non-Newtonian flow's characteristic, and these two designs cannot achieve the extruding rectangle shape filament because the molten polymer cannot expand averagely.

This problem can be solved by optimizing the geometry of the die, that could uniform the pressure at the edges and corners. Figure 4.4(c) shows the pressure distribution plot of the improved shape die. The pressure at the corners is less than the pressure at the edges, and the pressure distribution is nearly uniform and symmetrical, the filament surface tends to expand to a rectangle similar shape which drove by the internal pressure. The stress cusp effect could also be eliminated by adding a fillet feature. A comparison between these three nozzles shows that the filament extrusion quality could be controlled with die shape optimization. Moreover, the rectangular filament would improve deposition accuracy and efficiency for large-scale objects.

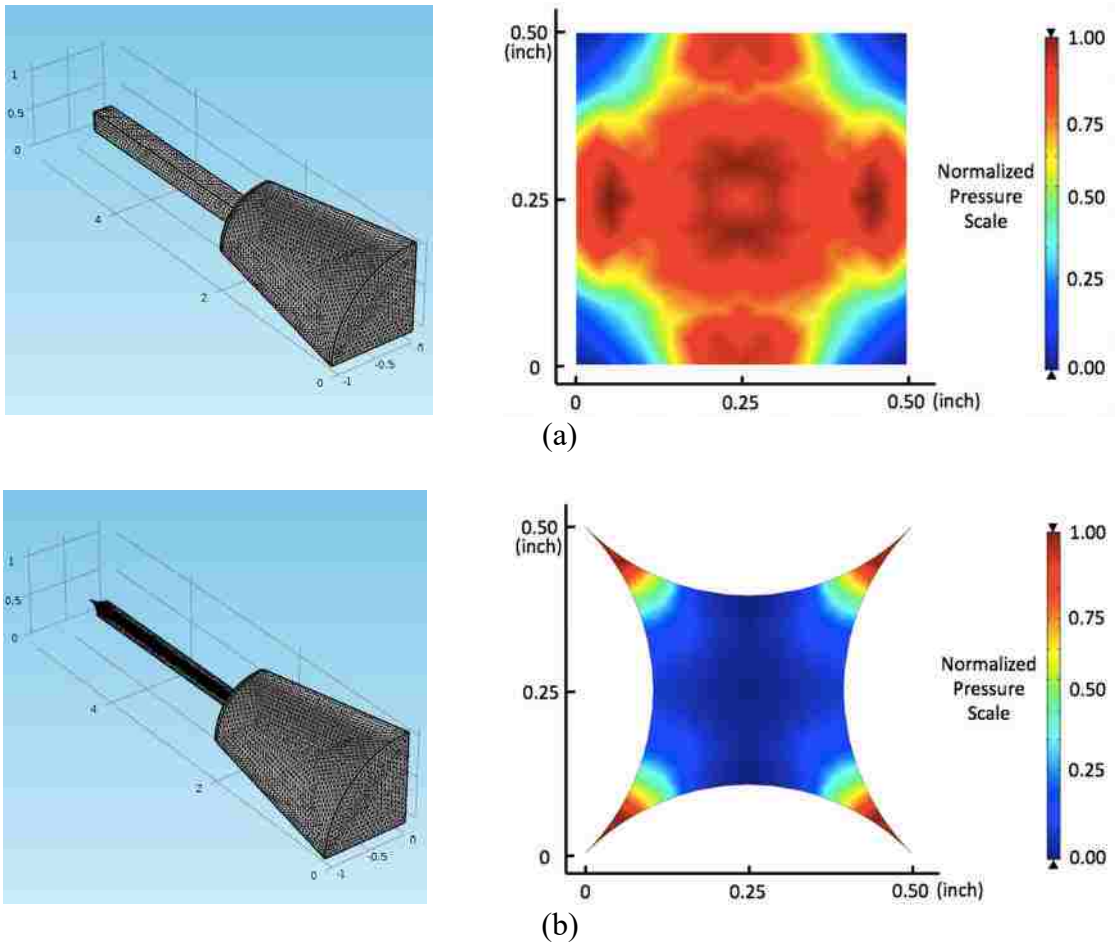

Figure 4.4 Meshed single quadrant inside volume models and
the cross section pressure distribution plot at the outlet of the nozzle

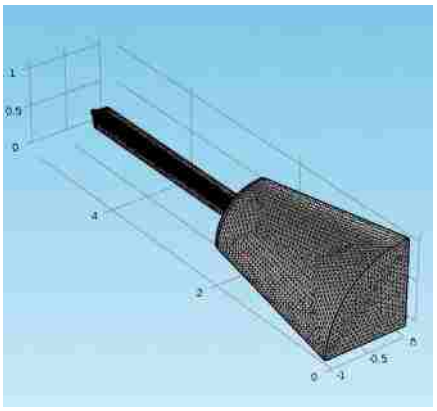

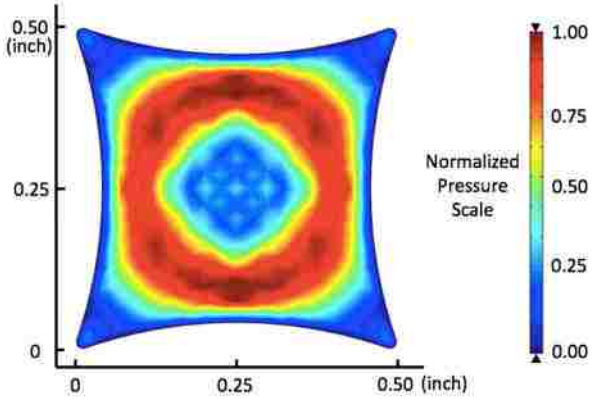

(c)

Figure 4.4 Meshed single quadrant inside volume models and
the cross section pressure distribution plot at the outlet of the nozzle (cont.)

5. CONCLUSION

Filament based fused extrusion deposition has been innovated and developed for a long period of time. It has the advantages of being a simple and economical system structure, but the low extrusion speed and enclosed workspace limit applying this technique to build a large-size prototype. To solve these problems, a fused pellet modeling (FPM) method is proposed. A screw with a variable pitch and progressive diameter would be designed to provide sufficient extrusion material at a high speed and with a certain back pressure. Analyzing the cause of void density in fused deposition based on the Carreau model would allow the die shape to be optimized for LDPE material in COMSOL. The next step of this project will include an investigation of the coupling affection of multi-physic fields (including hydromechanics, thermodynamics, and phase change) on the deposition process of fused pellet modeling (FPM) to build high-quality large-size prototypes with efficiency.

ACKNOWLEDGEMENTS

This research was supported by Laser Aided Manufacturing Processes (LAMP) Laboratory at Missouri University of Science and Technology (Missouri S&T). Their support is greatly appreciated. The author would like to thank Maxwell Mulholland and Huixu Deng from the Department of Mechanical & Aerospace Engineering at Missouri S&T for their valuable contribution to the project. The author would also like to thank all the people attached directly or indirectly to the project.

REFERENCES

[1] Masood S H. Intelligent rapid prototyping with fused deposition modelling. Rapid Prototyping Journal, 1996, 2(1): 24-33.

[2] Volpato, N., et al. "Experimental analysis of an extrusion system for additive manufacturing based on polymer pellets." The International Journal of Advanced Manufacturing Technology (2015): 1-13.

[3] Bellini A, Shor L, Guceri S I. New developments in fused deposition modeling of ceramics. Rapid Prototyping Journal, 2005, 11(4): 214-220.

[4] Newell, Clint, et al. Out of Bounds Additive Manufacturing. ADVANCED MATERIALS & PROCESSES, (2013): 15-17.

[5] Wang T M, Xi J T, Jin Y. A model research for prototype warp deformation in the FDM process. The International Journal of Advanced Manufacturing Technology, 2007, 33(11-12): 1087-1096.

[6] Jayanthi S, Keefe M, Gargiulo E P. Studies in stereolithography: influence of process parameters on curl distortion in photopolymer models. Solid Freeform Fabrication Symposium 1994. University of Texas, Austin, 1994: 250-258.

[7] Bellehumeur C, Li L, Sun Q, et al. Modeling of bond formation between polymer filaments in the fused deposition modeling process. Journal of Manufacturing Processes, 2004, 6(2): 170-178.

[8] Sun Q, Rizvi G M, Bellehumeur C T, et al. Effect of processing conditions on the bonding quality of FDM polymer filaments. Rapid Prototyping Journal, 2008, 14(2): 72-80.

[9] Li L, Sun Q, Bellehumeur C, et al. Composite modeling and analysis for fabrication of FDM prototypes with locally controlled properties. journal of Manufacturing Processes, 2002, 4(2): 129-141.

[10] Hori Y, Okubo S. On the normal stress effect and the Barus effect of polymer melts. Journal of Rheology (1978-present), 1980, 24(1): 39-53.

[11] Bogale K. Simulation and Design of Extrusion Dies. Arcada University of Applied sciences, Finland, 2011.

SECTION

2. CONCLUSION

Since the robot arm functions as the motion mechanism in the robotic hybrid manufacturing process, thus the research issues on optimizing robot accuracy and stiffness property are very important. A new methodology was developed for finding the best position and orientation to perform a specific tasks based on the current robot system accuracy capability. The knowledge of rigid body representation and homogeneous transformation matrices was introduced. Then the D-H model of Nachi Robot (SC300F-02) was established and the detail solution of robot forward/inverse kinematic was given. Since joint angle error affects the end effector position accuracy greatly, a robot positon error model was created to analyze the sensitivity of each joint with angle error. It reveals that even the same joint angle error could have different weight of affection when it appears on different joint. Thus, a new evaluation formulation was established for mapping the trajectory accuracy within the robot's working volumetric. With a group of known joint error, influence of different position and orientation on the movement accuracy of end effector was discussed.

For solving the problem of enhancing robot trajectory stiffness under heavy external load, firstly the detail process of solving robot jacobian matrix was presented, and the force jacobian matrix also has been derived according to the concept of virtual work. Based the on the assumptions of the link of industrial robot is rigid and all the deformation are concentrated at joints, the stiffness model of serial manipulator was developed. Then the robot stiffness matrix was derived from the robot jacobian matrix and robot joint stiffness matrix. By analyzing the robot kinematic and the properties of robot stiffness

matrix, a new evaluation formulation has been established for mapping the trajectory's stiffness within the robot's working volumetric. A trajectory stiffness simulation analysis system was developed for discussing the stiffness difference of a robotic deposition working path at different positions and orientations. The simulation results revealed that for the small size working path, in macro view, most turning points are concentrated within a small area, position is the main factor that affect the stiffness performance of this specific task. But for the large scale working path, the orientation of trajectory would affect the distribution of turning pointing a lot, thus lead to a great difference of stiffness performance.

For improving the engineering application of robotic hybrid manufacturing, an adaptive robot ink deposition system aimed at writing larger-scale letters on a curved surface was developed. Based on the contour points, gathering information about the 3D model and using it to reconstruct the characters is an easier method than other control algorithms for robot writing, and this process also served as a test method for robot ink deposition. Using the proposed curved surface measurement method, the robot was not limited to writing only on a flat surface, which has been the standard, especially for writing large-scale characters. In addition, the compensation control algorithm also was shown to apply to the robot repair area, which focuses mainly on curved deposition.

Moreover, the research and applications of a stereo vision based hybrid metal manufacturing system are summarized. The issues include understanding the DED process, the stereo vison aided automated process planning, and laser displacement sensor surface scanning. The stereo vison based path planning and laser sensor scanning make the process has less involvement with manual operation, enhance the automation and accuracy of

additive manufacturing process. The overall goal for process planning is not only to find a solution to build a part but also to look for an answer to produce it in the least amount of time; therefore, the least amount of switching between the machining process and deposition process, the better since each switch requires retreating and relocating the deposition nozzle as well as the machining tool, which may cost extra time. With integration of multi-axis deposition and machining processes on the same work station, a hybrid system is able to produce complicated geometry, especially the overhang structure with less or no support structures.

In order to extend the robotic hybrid manufacturing process to the broader application area, a fused pellet modeling (FPM) system is proposed. A screw with a variable pitch and progressive diameter would be designed to provide sufficient extrusion material at a high speed and with a certain back pressure. Analyzing the cause of void density in fused deposition based on the Carreau model would allow the die shape to be optimized for LDPE material in COMSOL. The simulation result shows that the filament extrusion quality could be controlled with die shape optimization. Moreover, the rectangular filament would improve deposition accuracy and efficiency for large-scale objects.

The overall outcomes of this dissertation addressed several key issues which challenging the development of robotic hybrid manufacturing. It provided a systematic approach for analyzing the factors that could affect robot accuracy in actual hybrid manufacturing processes, and establish the schema for optimizing working trajectory to maximize the accuracy and stiffness capacity of robot. In addition, the stereovision

measurement and adaptive path planning technology is important for improving the efficiency of robot hybrid manufacturing process.

Moreover, the fused pellet modeling (FPM) system avoids most of the defects that occur during the material extrusion steps in a filament-based system, make the large-scale robotic deposition object much more feasible and easier to implement.

BIBLIOGRAPHY

[1] J. Hur, K. Lee, h. Zhu, J. Kim, Hybrid rapid prototyping system using machining and deposition, Computer-Aided Design, 34 (2002) 741-754.

[2] Summers, Mark. "Robot capability test and development of industrial robot positioning system for the aerospace industry." SAE transactions 114.1 (2005): 1108-1118.

[3] Fassi, Irene, et al. "Calibration of serial manipulators: theory and applications." Industrial Robotics: Programming, Simulation and Applications (2007): 147-170.

[4] Park, In-Won, and Jong-Hwan Kim. "Estimating entire geometric parameter errors of manipulator arm using laser module and stationary camera." IECON 2011-37th Annual Conference on IEEE Industrial Electronics Society. IEEE, 2011.

[5] Wang, Dali, Ying Bai, and Jiying Zhao. "Robot manipulator calibration using neural network and a camera-based measurement system." Transactions of the Institute of Measurement and Control (2010).

[6] Nagata, Fusaomi, et al. "CAD/CAM-based position/force controller for a mold polishing robot." Mechatronics 17.4 (2007): 207-216.

[7] Zhang, Hui, et al. "Machining with flexible manipulator: toward improving robotic machining performance." Advanced Intelligent Mechatronics. Proceedings, 2005 IEEE/ASME International Conference on. IEEE, 2005.

[8] Lo, Ka Wah, et al. "Brush footprint acquisition and preliminary analysis for Chinese calligraphy using a robot drawing platform." Intelligent Robots and Systems, 2006 IEEE/RSJ International Conference on. IEEE, 2006.

[9] Kwok, Ka Wai, et al. "Genetic algorithm-based brush stroke generation for replication of Chinese calligraphic character." Evolutionary Computation, 2006. CEC 2006. IEEE Congress on. IEEE, 2006.

[10] Yao, Fenghui, Guifeng Shao, and Jianqiang Yi. "Extracting the trajectory of writing brush in Chinese character calligraphy." Engineering Applications of Artificial Intelligence 17.6 (2004): 631-644.

[11] J. Gao, J. Folkes, O. Yilmaz, N. Gindy, Investigation of a 3D non-contact measurement based blade repair integration system, Aircraft Engineering and Aerospace Technology, 77 (2005) 34-41.

[12] Liou, Frank; Slattery, Kevin; Kinsella, Mary; Newkirk, Joseph; Chou, Hsin-Nan; Landers, Robert, “Applications of a Hybrid Manufacturing Process for Fabrication and Repair of Metallic Structures,” Rapid Prototyping Journal, 2007, ISSN: 1355-2546, 2007 Volume: 13 Issue: 4 Page: 236 - 244.

[13] Masood S H. Intelligent rapid prototyping with fused deposition modelling. Rapid Prototyping Journal, 1996, 2(1): 24-33.

[14] Volpato, N., et al. "Experimental analysis of an extrusion system for additive manufacturing based on polymer pellets." The International Journal of Advanced Manufacturing Technology (2015): 1-13.

[15] Bellini A, Shor L, Guceri S I. New developments in fused deposition modeling of ceramics. Rapid Prototyping Journal, 2005, 11(4): 214-220.

[16] Newell, Clint, et al. Out of Bounds Additive Manufacturing. ADVANCED MATERIALS & PROCESSES, (2013): 15-17.

VITA

Zhiyuan Wang was born in Handan, Hebei, China. He received his Bachelor of Science degree in Mechanical Engineering in June 2008 from Lanzhou University of Technology, Lanzhou, China. In December 2010, he received his Master of Science degree in Mechanical Engineering from Lanzhou University of Technology, Lanzhou, China. In December 2016, he received his Doctor of Philosophy in Mechanical Engineering from Missouri University of Science and Technology, Rolla, Missouri, USA. He won the first place award for the poster presentation entitled "Multi-Axis Planning System for Robotic Deposition" at the 8th Intelligent System Center (ISC) Graduate Research Symposium on November, 2012 at Missouri University of Science and Technology. During his Ph.D. study, he authored and co-authored 6 journal papers and 4 conference papers.